University of South Bohemia in České Budějovice

Faculty of Science

Molecular modeling of biomolecules – surface interactions

Ph.D. Thesis

Ing. Ondřej Kroutil

Supervisor: doc. RNDr. Milan Předota, Ph.D.

Faculty of Science, Institute of Physics and Biophysics,
University of South Bohemia in České Budějovice

České Budějovice 2016

This thesis should be cited as:

Kroutil, O., 2016: Molecular modeling of biomolecules – surface interactions. Ph.D. Thesis Series, No. 6. University of South Bohemia, Faculty of Science, České Budějovice, Czech Republic, 128 pp.

Annotation

Interactions between (bio)molecules, ions and solid surfaces play crucial role in many biological processes as well as in many scientific applications and understanding of this phenomenon on *molecular level* is a challenging task for today science. Computer simulations can provide detailed view on atomic level if carefully prepared and evaluated models are used.

In this thesis, interactions of several types of (bio)molecules with inorganic surfaces are studied by classical and ab initio molecular dynamics. Chemisorbed biomolecules, namely DNA and oligopeptide, covalently attached to graphene and mercury surface, respectively, were studied to make link with DNA chip design and experimental label-free electrochemical measurements, respectively. Quartz (101) surface model applicable to wide range of pH conditions was developed and evaluated against experimental X-ray data. Physisorption of the nucleobases on quartz (101) surface and oxalate dianion on rutile (110) was examined and discussed.

Declaration [in Czech]

Prohlašuji, že svoji disertační práci jsem vypracoval samostatně pouze s použitím pramenů a literatury uvedených v seznamu citované literatury.

Prohlašuji, že v souladu s § 47b zákona č. 111/1998 Sb. v platném znění souhlasím se zveřejněním své disertační práce, a to v úpravě vzniklé vypuštěním vyznačených částí archivovaných Přírodovědeckou fakultou elektronickou cestou ve veřejně přístupné části databáze STAG provozované Jihočeskou univerzitou v Českých Budějovicích na jejích internetových stránkách, a to se zachováním mého autorského práva k odevzdanému textu této kvalifikační práce. Souhlasím dále s tím, aby toutéž elektronickou cestou byly v souladu s uvedeným ustanovením zákona č. 111/1998 Sb. zveřejněny posudky školitele a oponentů práce i záznam o průběhu a výsledku obhajoby kvalifikační práce. Rovněž souhlasím s porovnáním textu mé kvalifikační práce s databází kvalifikačních prací Theses.cz provozovanou Národním registrem vysokoškolských kvalifikačních prací a systémem na odhalování plagiátů.

České Budějovice, 26. 6. 2016

…….

Ondřej Kroutil

This thesis originated from research projects solved at Faculty of Science, University of South Bohemia.

Přírodovědecká
fakulta
Faculty
of Science

Financial support

GAČR 203/08/0094
MŠMT - Kontakt, ME 09062
GAČR: 13-08651S
GAČR: P208/12/0622

Acknowledgements

Mé milované manželce Ivě za všechno! Miluji tě!

Mamce, taťkovi a celé rodině (včetně Smíšků!) za všechnu podporu a lásku, kterou mi kdy dali.

Milanu Předotovi za to, že byl tím nejlepším školitelem, jakého jsem mohl mít. Za to, co mě naučil, ale i za to, že se nechal něco naučit ode mne i on, což mně vždy dávalo pocit rovnocenného partnerství a smysluplné práce.

Zdeňku Chvalovi za jeho bezelstnou pomoc při psaní článků a všechnu tu trpělivost, které někdy muselo být víc než dost.

Martinu Kabeláčovi, Babaku Minofarovi a Davidu Řehovi za skvělou vědeckou i mimovědeckou spolupráci.

Olze Dvořáčkové, Lukáši Martínkovi a Davidu Kimmerovi za zpříjemnění chvil na ZSF i mimo ni.

Všem Hammonderům a speciálně Futrálům za neopakovatelné hudební zážitky v ČB.

A všem ostatním za to, že jsou a je mi s nimi dobře…

List of papers and author's contribution

The presented thesis is based on the papers OK1-OK4. Although publications OK5 and OK6 fall under the biophysical modeling as previous ones, the topic is different and thus they are not included in this thesis. Numbering OK1-OK4 will be used throughout this thesis.

OK1) Kroutil O., Chval Z., Skelton A. A., Předota M. (2015): Computer Simulations of Quartz (101)–Water Interface over a Range of pH Values. The Journal of Physical Chemistry C 119 (17), 9274-9286; IF(2014) = 4.772

OK *implemented new force field to Gromacs software package, performed all molecular dynamics simulations of water and ions interacting with the quartz surface and carried out all analyses. He participated in the paper writing.*

OK2) Kabeláč M., **Kroutil O.**, Předota M., Lankaš F., Šíp M. (2012): Influence of a charged graphene surface on the orientation and conformation of covalently attached oligonucleotides: a molecular dynamics study. Physical Chemistry Chemical Physics 14 (12), 4217-4229; IF(2014) = 4.493

OK *prepared the model of graphene and attached oligonucleotide, performed several molecular dynamics simulations and participated in the paper writing.*

OK3) Dorčák V., Kabeláč M., **Kroutil O.**, Bednářová K. and Vacek J. (2016): Electrocatalytic Monitoring of Peptidic Proton-Wires. (Manuscript accepted in Analyst); IF(2014) = 4.107

OK *participated in the paper writing.*

OK4) Kroutil O., Minofar B., Kabeláč M. (2015): Structure and Dynamics of Solvated Hydrogenoxalate and Oxalate Anions: a Theoretical Study, (Manuscript)

OK *prepared all models, performed all ab initio molecular dynamics simulations and did several analyses. He participated in the paper writing.*

OK5) Kroutil O., Romancová I., Šíp M., Chval Z. (2014): Cy3 and Cy5 Dyes Terminally Attached to 5′C End of DNA: Structure, Dynamics, and Energetics. The Journal of Physical Chemistry B 118 (47), 13564-13572; IF(2014) = 3.302

OK *prepared all models, performed several molecular dynamics simulations and did several analyses. He participated in the paper writing.*

OK6) Kroutil O., Předota M., Chval Z. (2016): Pt…Hw Non-Classical Interaction in Water Dissolved Pt(II)-Complexes: Coaction of Electronic Effects with Solvent-Assisted Stabilization., Inorg Chem, 55 (7), 3252–3264; IF(2014) = 4.762

OK *prepared all models for ab inito molecular dynamics, performed dynamics simulations and did several analyses. He participated in the paper writing.*

Contents

List of abbreviations:

AIMD	Ab Initio Molecular Dynamics
BOMD	Born-Oppenheimer Molecular Dynamics
CMD	Classical Molecular Dynamics
CPMD	Car-Parinello Molecular Dynamics
GPW	Gaussian Plane-Wave method
MD	Molecular Dynamics
RDF	Radial Distribution Function
RESP	Restrained ElectroStatic Potential
AA	Amino Acid
Cx	Oxalate carbon
DIW	DeIonized Water
ds-DNA	double-stranded Deoxyribonucleic Acid
HIE	neutral histidine
HIP	protonated histidine
Hw	Water hydrogen
Ow	Water oxygen
Ox	Oxalate oxygen
ox-1	Hydrogenoxalate anion
ox-2	Oxalate dianion
ss-DNA	single-stranded Deoxyribonucleic Acid
AFM	Atomic Force Microscopy
BL	Brandt and Lyubartsev parameters
CPS	Current chronoPotentiometric Stripping
CPU	Central Processing Unit
CTR	Crystal Truncation Rod
EDL	Electric Double-Layer
GPU	Graphical Processor Unit
CHER	Catalytic Hydrogen Evolution Reaction
MA	Matsui and Akaogi parameters
MUSIC-CD	MUltiSIte Complexation – Charge Distribution
PZC	Point of Zero Charge
RAXR	Resonant Anomalous X-ray Reflectivity
SHG	Second Harmonic Generation
SPR	Surface Plasmon Resonance
XR	X-ray Reflectivity
XSW	Standing Wave

I was just guessing
At numbers and figures
Pulling the puzzles apart

Questions of science
Science and progress
Do not speak as loud as my heart

The Scientist, Coldplay

1. Introduction

1.1 Motivation

Interactions between (bio)molecules, ions and solid surfaces play crucial role in many biological processes as well as in many scientific applications. Understanding of this phenomenon on *molecular level* is a challenging task for today science. From the beginning of the 20th century when Langmuir presented his model for the monolayer adsorption of species onto simple surfaces [Langmuir, 1918], the surface and interface science has gone long journey and has grown up into fully-fledged discipline with its own specific experimental methods and theoretical models. Experimental techniques like atomic force microscopy (AFM), surface plasmon resonance (SPR), resonant anomalous X-ray reflectivity (RAXR) and second harmonic generation (SHG) together with in-silico techniques like classical molecular dynamics (CMD), ab initio molecular dynamics (AIMD), and accompanied by various models of electric double-layer (EDL) and surface complexation models (e.g. MUSIC-CD, i.e. MUltiSIte Complexation – Charge Distribution) can give complex and detailed picture of what happens at the surface and interface during adsorption of (almost) any kind atom, ion or molecule.

(Bio)molecules/solid surface interactions that are heart of this thesis belong to a wide family of processes generally called *adsorption*. Adsorption is defined as "the accumulation of a substance at an interface" [Butt, 2003] and it is purely surface phenomenon with no penetration of the *adsorbate* into the bulk region of the *adsorbent* (contrary to *absorption*). *Interface* is a narrow contact region between two phases where

physical and chemical properties of adsorbate differ from their bulk values. Properties and processes in this region are crucial for understanding of adsorption.

If we consider three states of matter, i.e. solid, liquid and gas state, we get several combinations of the interfaces: the solid–liquid, the solid–gas, and the liquid–gas interface (commonly called *surfaces*), or interfaces between two immiscible liquids (liquid–liquid interfaces) or different solid materials (solid–solid interfaces). Out of these combinations, only the *solid–liquid* interface is a subject of our interest, because all simulations described in this thesis are tightly connected to experiments investigating this interface.

Adsorption can be categorized using various criteria, but the strength of the interaction between adsorbate and adsorbent is the key factor. Weak adsorption where only van der Waals forces act between surface and adsorbate is called *physisorption* while strong adsorption accompanied by creation and/or disruption of chemical bonds is called *chemisorption*. Physisorption is usually characterized by the sorption energy of the order of 20–40 $kJ.mol^{-1}$, relatively free adsorbate able to diffuse and rotate on the surface, and quick establishing of an adsorption equilibrium. Contrary, chemisorption has usually typical sorption energies of 100–400 $kJ.mol^{-1}$, the adsorbate is relatively immobile and usually does not diffuse on the surface and often leads to surface reconstruction. We have dealt with both types of the adsorption in our work, physisorption is described in Chapter 3 and chemisorption in Chapter 4.

As adsorption of (bio)molecules takes place very often in water environment with dissolved ions, one has to be also beware of adsorption of these substances. Water molecules at a solid substrate often experience a hindered rotation relative to those in the bulk, forming dense layers of the solvent up to few nanometers above the surface. Then, if liberated from the surface via displacement by an adsorbed molecule, a net entropy gain results. At the same time ions can occupy charged spots on the surface and/or and adsorbent, hereby influencing equilibrium of the adsorption. Thus, high-quality models of the surfaces and adsorbing molecules that properly quantify interactions with water and ions are crucial for the success of simulations. Development and evaluation of these models is discussed in detail in Chapter 2 and Chapter 3.

Due to complexity of the topic and corresponding large number of simulations, systems and analyzed data, not all results included in thesis have been published yet. But to give overall picture of our work and to maintain hierarchy of the topic, we combine both published and unpublished data in the following text.

1.2 Organic molecules, nucleic acids and peptides

1.2.1 Oxalic acid

Oxalic acid is the most simple dicarboxylic acid, being composed of two COOH groups directly connected together (see Figure 1-1, $C_2H_2O_4$). It occurs in nature as a calcium oxalate mineral (whewellite, weddellite), it has been spotted in traces in atmosphere as a product of the combustion of fossil fuels or exhaust of cars, representing 37-69 % of the total dicarboxylic acids in atmosphere [Kawamura and Ikushima, 1993]. It also shows a wide biological activity in plants and animals. For example, it was revealed [Sharma, 1993] that oxalic acid and diacylglycerol metabolites in blood are quantitatively depleted under sleep-restricted conditions and restored after recovery of sleep. Under physiological conditions, oxalate ion can interact with calcium ion and thus it plays an important role in the formation of calcium-containing uroliths in human body. It has high solubility (143 $g.dm^{-3}$; due to polarity and formation of intra and intermolecular hydrogen bonds) and very low first deprotonation constant of pK_{a1} = 1.24. Thus, in near-neutral pH it occurs mainly as oxalate dianion ($C_2O_4^{2-}$) with very small amounts as hydrogenoxalate anion ($C_2HO_4^-$, pK_{a2} = 4.23) (Figure 1-1). Albeit oxalic acid and both its anions are relatively simple chemical compounds, their structure, solvation and parameterization is still a matter of debate.

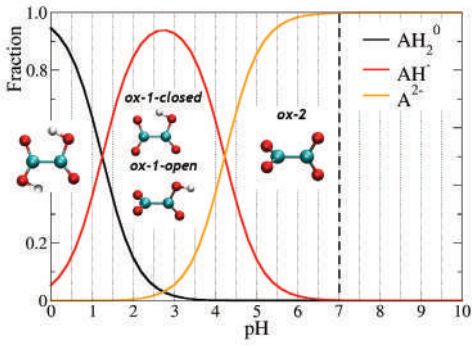

Figure 1-1. Fraction of total oxalate in any protonation form as a function of pH. Neutral pH highlighted by dashed curve. Inset: corresponding structures and naming.

1.2.2 Nucleobases

Nucleic acid bases, i.e. nitrogenous purine and pyrimidine bases, and their related structures with attached 5-membered sugar ring and phosphate group(s) - nucleosides and nucleotides (see Figure 1-3 in Charter 1.2.3), are essential molecules for all living beings. They serve as building blocks of nucleic acids and as co-factors of enzymatic reactions (coenzyme A, FAD, FMN), and alone they participate in metabolism as chemical energy

storage media, or in cellular signaling [Francis and Corbin, 1999]. Nucleosides are also used as dietary supplements and modified forms of purines and pyrimidines are promising new drugs [Jordheim, 2013].

The primary nucleobases are cytosine (DNA and RNA), guanine (DNA and RNA), adenine (DNA and RNA), thymine (DNA) and uracil (RNA), abbreviated as C, G, A, T, and U, respectively (Figure 1-2, uracil not shown). Adenine and guanine belong to the purine and thymine, cytosine and uracil to the pyrimidine family of bases. Apart primary nucleobases also modified versions exist with hypoxanthine, 7-methylguanine, or 5-hydroxymethyl cytosine being the most known examples.

Immobilization of nucleobases (and all derived molecules mentioned above) onto inorganic surfaces is a determining factor for many scientific techniques such as biosensing (DNA microarray) [OK2], chromatographic and electrophoretic separation of these species [Marrubini, 2010], oligonucleotide synthesis (phosphoramidite process) [Sanghvi, 2000], for development of biocompatible materials [Li, 2011] and for prebiotic polymerization of RNAs and DNAs [Brindley, 1968; Mignon, 2009].

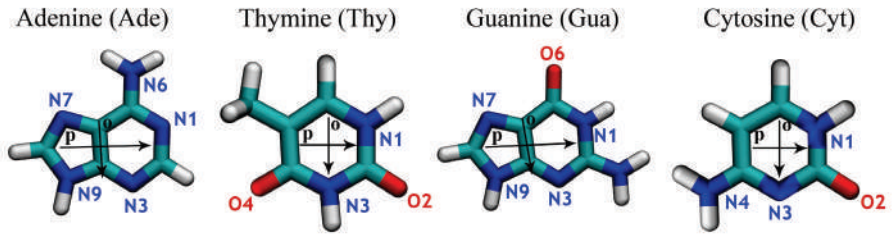

Figure 1-2. Four nucleobases used in our study. Main atoms and vectors used to complete bivariate plots shown.

There is an ongoing interest in nucleobases adsorption onto various surfaces. The most recent experimental studies have focused mainly on the adsorption onto pure metal [Feyer, 2011; Plekan, 2010] (and especially gold [Pagliai, 2012; Plekan, 2012; Yang, 2009; Kundu, 2009]) and carbon-based [Panigrahi, 2012; Varghese, 2009; Sowerby, 2001] surfaces due to applicability of these results in biosensing. The main emphasis in these studies has been on the orientation of the adsorbed molecules (perpendicular vs. parallel) and a type of the adsorption (physi- vs. chemisorption). Similar situation occurs in the field of theoretical chemistry with several quantum mechanical [Bogdan and Morari, 2012; Umadevi and Sastry, 2011; Rajarajeswari, 2011; Piana and Bilic, 2006] and molecular dynamic studies [Maleki, 2011; Rapino, 2005; Piana and Bilic, 2006].

Some experimental studies have focused on the behavior of the nucleic acids components near metal-oxides [Cleaves, 2010; Plekan, 2007] and clay materials [Baú, 2012; Carneiro 2011] with the main motivation to explain a prebiotic chemical processes, since it is believed that immobilization of nucleic acid components is a necessary step for the polymerization of these species.

Few molecular dynamics studies have tried to identify a binding arrangement and to quantify the strength of interactions of nucleobases with the rutile surface [Monti, 2011] and with a Si (111) surface with attached alkyl-amine molecules [Monti, 2011].

To the best of our knowledge, there are no systematic all-atom molecular dynamics simulations studying these nucleobases binding on various surfaces at various conditions.

1.2.3 Nucleic acids

Nucleic acid molecules (NAs) are essential biomolecules that all living organisms have in common. They execute variety of functions in living cells ranging from transmission of genetic information between generations and transcription of the genetic information into proteins, through catalytic functions to gene regulation. Basic structural unit of nucleic acids is the nucleotide (Figure 1-3a, yellow), each of which contains a pentose sugar (deoxyribose in DNA and ribose in RNA), a phosphate group, and a nucleobase (Figure 1-3b). Sugar and phosphate group creates so-called sugar-phosphate backbone (Figure 1-3a, purple) that carries large negative charge due to deprotonated phosphate (PO_4^{-1}) groups. Nucleobases were described in detail in previous chapter (Chapter 1.2.2). NAs can be either single-stranded or double-stranded with complementary bases that can *hybridize* via

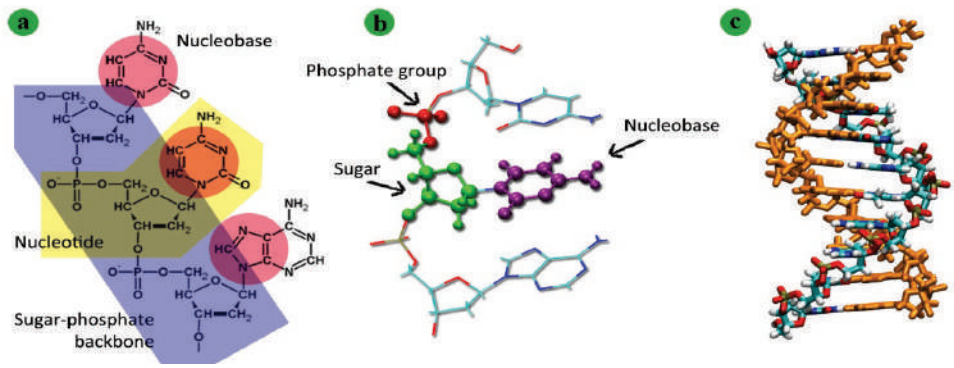

Figure 1-3. (a) Schematic representation of the DNA constituents, (b) Ball-and-stick representation of the nucleotide; (c) Licorice representation of a double stranded DNA with its typical helical geometry. Single strand highlighted by orange color.

making of the weak hydrogen bonds between nucleotides and forming typical double-stranded helix. DNA molecules are in most cases double-stranded, whereas RNA molecules are usually single-stranded [Hodge, 2009].

DNA is more stable than RNA and is located in a cell nucleus where it stores genetic information, being coiled into higher structural units called *chromosomes*. All chromosomes together make up so-called *genome* that is, in the case of humans, composed of approximately 3 billion of base pairs arranged into 46 chromosomes. *Gene* is a certain part of long DNA molecule that encodes a functional RNA or protein product. Rapid and cheap detection of a sequence of the nucleotides in a gene (so-called *sequencing*), is a main interest of today science because with knowledge of the exact order of nucleotides one can identify changes in genes, associations with diseases and phenotypes, study how different organisms are related and how they evolved, determine if there is risk of genetic diseases, etc.

For this purpose, microarrays or DNA chips are appropriate devices. Arrays of tens to tens of thousands of microscopic spots containing single-stranded deoxyribonucleotides are attached to a solid surface (such as a membrane, a polymer, or glass) of the microarray, and these are used to analyze simultaneously a sample solution containing fragments of nucleic acids. Oligonucleotides (capture probes) in individual spots are identical, but their sequences are different for each spot to match the various complementary DNA sequences (targets) present in a given sample. The sequences of surface-immobilized capture probes needs to be designed to meet several criteria: they should not allow the formation of internal structures such as hairpins and they should be sensitive to sequence variations and bind only to complementary strands. Usually, software tools available for probe design during the process of microarray development are based on standard hybridization conditions, i.e. nucleic acids in solution, not being attached to a surface.

However, the surface plays an important role and can influence process of hybridization to a large extent. First, the capture probes are immobilized to a certain extent by surface binding and therefore their molecular dynamics is different from that describing a system of two free strands in a solution. Second, the presence of the surface and the interactions of the capture probe with the surface represent an important sterical hindrance making single-strand – double-strand transitions more difficult. Third, in addition to the van der Waals interactions, the surface, whether it is charged or not, generates nontrivial electrostatics and interfacial structure owing to the interactions between the solution and the surface, influencing the density profiles of the water and ions in the vicinity of the surface and attached probes.

1.2.4 Peptides

Peptides are short chains composed of amino acid monomers (Figure 1-4a) linked by peptide bonds. There is 23 proteinogenic, i.e. protein-building amino acids. Peptide bonds are formed by condensation reaction when the carboxyl group of one amino acid reacts with the amine group of another (Figure 1-4b) while water is released. As peptides are a continuous and unbranched chain (Figure 1-4c), they fall under the broad chemical classes of biological oligomers and polymers, alongside nucleic acids, oligosaccharides and polysaccharides. Peptides contain approximately 50 or fewer amino acids, but the border is not strict.

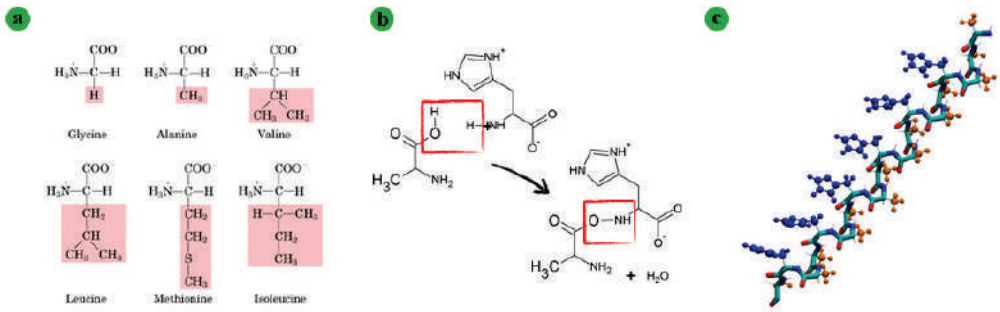

Figure 1-4. (a) Example of the several amino acids with highlighted side functional groups, (b) Creation of the peptide bond; (c) Peptide chain, backbone in licorice representation, side functional groups highlighted by orange and blue color and ball-and-sticks representation.

Similarly as in a label-free or label based analysis of nucleic acid (and also of polysaccharides and glycans), so far only carbon and mercury based electrodes have been found useful for the sensitive analysis required by contemporary peptide/protein research [Paleček, 2012; Paleček, 2015]. Use of carbon electrodes is limited to oxidation reactions of tyrosine (Tyr) or tryptophan (Trp) residues, while utilization of mercury or amalgam electrodes was earlier restricted only to the reduction processes involving SH- groups of Cys and/or SS-bonds of cystine (CSSC) residues. Nowadays, considerable progress in development of a method called constant current chronopotentiometric stripping (CPS), that utilizes mercury electrode, has widened number of amino acids that can be detected by this type of an electrode (see below), and has allowed characterization of the nanomolar quantities of various peptides and proteins.

This *label-free* and also *structure-sensitive* method is based on catalytic hydrogen evolution reaction (CHER) with a typical analytical output known as *peak H* (Figure 1-5)

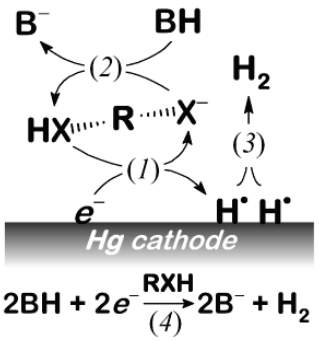

Figure 1-5. CHER mechanism

[Heyrovsky, 2005]. In hydrogen evolution catalyzed by a peptide or a protein molecule, CPS peak H is reflecting consumption of electrons in the irreversible reduction of exchangeable protons from the functional groups (–XH, located at side chains of some AA residues) close to the negatively charged electrode surface (reaction *1*, Figure 1-5). The effect is much more pronounced in buffered media in which the catalyst (peptide or protein) molecule (R–XH/R–X^-) in adsorbed state mediates a transport of protons from the acid constituent of a buffer (BH, reaction *2*) onto negatively charged electrode surface where subsequently surface bound hydrogen atoms ($H^•$) combine into more stable molecules of gaseous hydrogen (H_2, reaction *3*). Deprotonated functional groups ($–X^-$) are then immediately reprotonated by an excess of slightly acidic BH (reaction *2*) and enter reaction *1* closing thus a catalytic cycle. The net result is that while the catalyst is restored, the acid constituent of the solution is reduced under formation of molecular hydrogen (reaction *4*).

Artificial and bioactive peptides were studied mostly as a protein like models to identify catalytically active sites or to better understand fundamental basis of the electrocatalytic process taking place in the case of complex protein molecules [Sestáková, 2000; Enache 2013; Zuman, 2005]. In search for catalytically active amino acid residues, so far involvement of Cys thiol (pKa ~ 8), lysine (Lys) ε-ammonium (pKa ~ 11), arginine (Arg) guanidinium (pKa ~ 12), and His imidazolium (pKa ~ 6) groups had been unambiguously confirmed [Zuman, 2005, Palecek, 2014]. However, also ammonium group (pKa ~ 9) at peptidic chain N-end and hydroxyl group at Ser, Tyr, or Thr residues (pKa ~ 10) are capable of proton exchange reaction in solution but their involvement in CHER was neither confirmed nor denied.

From previous brief description of the CPS method it is evident, that interactions and conformations of peptide(s) on a mercury electrode are crucial for success of this method. Contrary to previous successful event, it was also shown on a set of angiotensin (AT) peptides [Dorčák, 2013] that presence of aspartic acid (Asp) residue bearing negatively charged carboxylate group in the vicinity of Arg residue can *cancel* catalytic activity of the peptide. Other preliminary results from Dorčák group with several Cys containing peptides indicate that also carboxylate group at side chain of glutamic acid (Glu) residue or at C-end of the peptide backbone can prevent involvement of the SH-groups in CHER. It is believed that very probably the electrostatic repulsion between the negative charges at

the electrode surface and carboxylate group prevailed over the electrostatic attraction of the positively charged Arg guanidinium group or hydrophobic interaction of Cys SH group and thus, detracted their involvement in CHER.

1.3 Computer simulations

1.3.1 Classical molecular dynamics

The classical molecular dynamics simulations propagate a series of instantaneous atomic configuration over time by integration of Newton's equations of motion. In CMD the atoms are represented by interacting sites (points) corresponding to their nuclei, while the electrons are considered only effectively via partial charges located at the atomic or auxiliary sites and assumed to follow the Born-Oppenheimer approximation. With this significant simplification and adopting pair-wise potentials for all inter-atomic interactions except angular bonded terms, systems composed of ~10^5 atoms can be simulated for times up to hundreds of nanoseconds on modern clusters of CPU and GPU units.

Basics of the classical molecular dynamics can be found elsewhere [Leach, 2001; Schlick, 2002]. For the purpose of this thesis just brief description of the non-bonded interactions is mentioned because we had to take special care of them.

Non-bonded interactions play an important role in MD simulations, because precisely these interactions stand behind adsorption phenomena, higher-level structure of molecules, hydration and hydrogen-bonding. Therefore the best possible parameters describing non-bonded interactions are crucial for success of the simulation.

We explicitly incorporate two types of non-bonded interactions in MD simulations: electrostatic interactions that are described by Coulomb's law (Equation 1-1):

$$\boldsymbol{U_{Elst.}(r_{ij})} = \frac{\boldsymbol{q_i q_j}}{\boldsymbol{4\pi\varepsilon_0 r_{ij}}} \tag{1-1}$$

and van der Waals forces that are almost exclusively described by Lennard-Jones potential (Equation 1-2) in standard biomolecular force fields:

$$\boldsymbol{U_{LJ}(r_{ij})} = \boldsymbol{4\varepsilon_{ij}}\left[\left(\frac{\boldsymbol{\sigma_{ij}}}{\boldsymbol{r_{ij}}}\right)^{\boldsymbol{12}} - \left(\frac{\boldsymbol{\sigma_{ij}}}{\boldsymbol{r_{ij}}}\right)^{\boldsymbol{6}}\right] \tag{1-2}$$

where σ_{ij} denotes the distance where the intermolecular potential between two atoms is zero, and and ε_{ij} the well depth characterizing how strong the attraction between two

atoms is. Using Lorentz-Berthelot combination rule (Equation 1-3) one can derive the cross parameters for different species:

$$\sigma_{ij} = \frac{\sigma_{ii}+\sigma_{jj}}{2};\ \varepsilon_{ij} = \sqrt{\varepsilon_{ii}\varepsilon_{jj}} \tag{1-3}$$

Another possibility is to take into account van der Waals forces in simulation using Buckingham potential (also known as exp-6 potential) (Equation 1-4):

$$U_{BH}(r_{ij}) = A_{ij}\exp\left(-\frac{r_{ij}}{b_{ij}}\right) - C_{ij}r_{ij}^{6} \tag{1-4}$$

where A_{ij}, b_{ij} describe components of the repulsive interaction and C_{ij} describes the attractive interaction. Both potentials for van der Waals interactions appeared in our work together in Chapter 2.4 and we had to dealt with their incompatibility.

1.3.2 Ab initio molecular dynamics

Unlike classical molecular dynamics, in ab initio molecular dynamics forces are computed on-the-fly by accurate electronic structure calculations and therefore AIMD does not rely on a set of empirical parameters as CMD. It also implies that bond making and breaking events are naturally included when ab initio calculations are involved.

Two approaches are in use [Vidossich, 2016]: Born-Oppenheimer MD (BOMD) where the time-independent electronic structure problem is solved for the actual nuclear configuration at each step during the dynamics, and Car-Parrinello MD (CPMD) where the electronic orbitals are evolved together with the ions, thus not requiring optimization of the wave function at each MD step.

Computer power requirements of ab initio calculations are enormous. State-of-art AIMD calculations dealt with systems composed of hundreds of atoms and simulation times up to hundreds of picoseconds, i.e. several orders of magnitude less than CMD.

In our work [OK4], we have used BOMD to study conformation and solvation shell of the oxalic acid anions.

1.3.3 Structural characteristics

Radial distribution function

The key structural property, radial distribution function $g(r)$, gives the probability of finding a particle in the distance r from another particle. Simply speaking, radial

distribution function (RDF) informs us how atoms in a system are radially packed around each other. This is particularly useful if one wants to describe the structure of disordered molecular systems, especially pure liquids and solutions. The disordered movement of molecules and atoms in a system with hardly recognizable order is converted by computing RDF to behavior of the average structure. It can reveal short range order due to presence of hydrogen bonds, London forces, etc., including contributions from nearest neighbors as well as more distant molecules.

RDF $g_{AB}(r)$ between particles of type A and B, resp. A and A is computed as (Equation 1-5):

$$g_{AB}(r) = \frac{N_{AB}(r, \Delta r)}{N_A N_B \frac{4\pi r^2 \Delta r}{V}}; \; g_{AA}(r) = \frac{N_{AA}(r, \Delta r)}{\frac{N_A(N_A - 1)}{2} \frac{4\pi r^2 \Delta r}{V}} \tag{1-5}$$

where N_{AA}, resp. N_{AB} is the number of corresponding pairs within a spherical shell of thickness Δr and centered around distance r from one of the species and N_A, N_B are numbers of particles (atoms) of given kind.

Except of being very informative structural property, great benefit of RDF arises from the fact, that it can be indirectly determined via its relation with the structure factor $S(q)$ from neutron scattering or X-ray scattering data. This allows experimental measurements and computer simulations to be mutually compared and interpreted.

Axial density profiles

Axial density profiles represent density profiles of species averaged laterally in the x and y directions to obtain only z dependent density, where z axis is perpendicular to the surface, typically with origin at the interface and facing the liquid phase. They are useful for the analysis of the distribution of groups or atoms across the interface including recognition of dissolved vs adsorbed species. They are easily accessible from the simulations and more indirectly from experimental studies too. Comparison between theoretical and experimental data was done by us many times [OK1, Chapter 2.1, Předota *et al.*, 2004] and allowed us to justify our models and thereafter broaden experimental findings with more detailed molecular view.

From the experimental techniques, X-ray reflectivity (XR), crystal truncation rod (CTR) and standing wave (XSW) measurements provide invaluable information on the structure of interfacial liquid (most commonly water), surface relaxation, and geometry of adsorbed ions [Zhang, 2004]. Typical XR signal, $R(Q)$, of quartz (101) in contact with deionized water and RbCl solution as a function of vertical momentum transfer is depicted

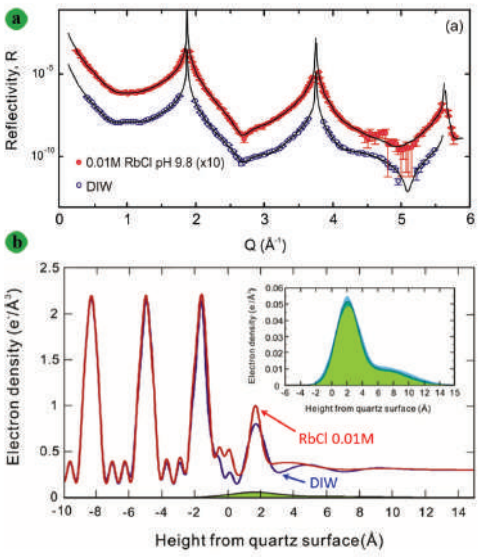

Figure 1-6. (a) Specular XR signal, $R(Q)$, of quartz (101) in contact with DIW (empty blue circles), and RbCl solution 0.01 M at pH 9.8 (fullred circles), as a function of vertical momentum transfer, Q;.(b) Derived electron density profiles for quartz(101) in contact with DIW (blue line) and 0.01 M RbCl solution at pH 9.8 (red line).

at Figure 1-6a [Bellucci, 2015], accompanied with derived axial electron density profiles (Figure 1-6b).

2. Surfaces

Four different surfaces have appeared one by one in our studies, namely graphene, mercury, quartz (101) and rutile (110) surfaces (Figure 2-1). This chapter describes in depth developing, evaluation and comparison of these surface models.

2.1 Graphene

Graphene surface was used as a substrate in our study focusing on a behavior of nucleic acids chemisorbed on the graphene surface [OK2].

Graphene is two-dimensional material only one monolayer thick (Figure 2-1). It can be considered as one layer from multi-layered graphite mineral. It consists of carbon atoms densely packed in regular hexagonal pattern with surface atom density of 38.2 atoms.nm^{-2}.

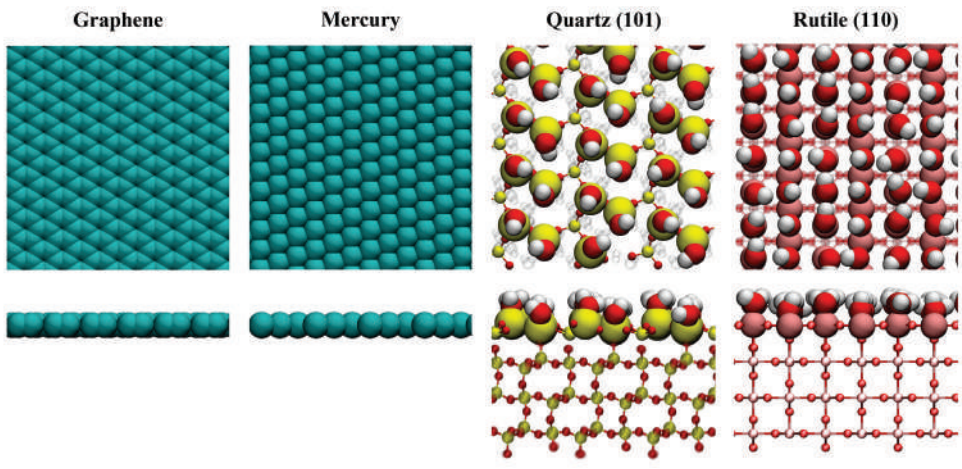

Figure 2-1. Top and side views of four different surfaces used in our studies.

This surface atom density is more than four times the density of mercury atoms used to model mercury surface. Graphene surface possesses very extraordinary properties like very high specific surface area (2630 $m^2.g^{-1}$), remarkable electron mobility at room temperature (15000 $cm^2.V^{-1}.s^{-1}$), unique optical properties with an unexpectedly high opacity, etc.

This particular surface was selected as the substrate in our simulations, because it was a relatively simple but realistic surface with its geometry independent of pH, salt concentration, etc. Furthermore, some theoretical studies on DNA interactions with carbon nanotubes (surfaces based on graphene geometry) were available at that time and binding of DNA to carbon nanotubes was identified as a way to open the door to carbon–nanotube–based applications in biotechnology.

For the carbon atoms of graphene, we have used 'CA' atomic type from Amber99SB force field with parameters σ_{CC} = 0.340 nm and ε_{CC} = 0.360 $kJ.mol^{-1}$. Similar parameters were used in other papers simulating carbon–nanotube–DNA interactions [Hummer, 2001; Zhao, 2007; Johnson, 2009].

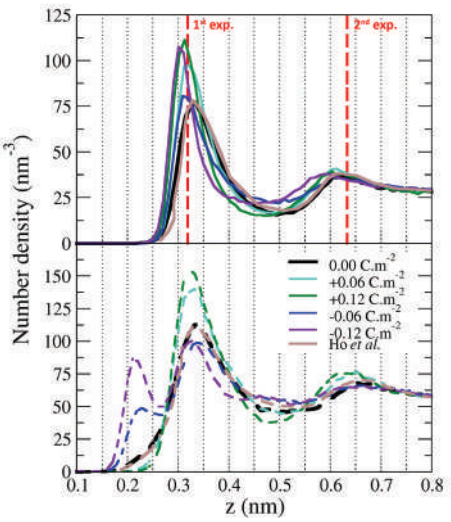

Figure 2-2. Axial density profiles of water oxygen Ow (upper graph) and hydrogen Hw (lower graph) for all surface charge densities. Positions of experimentally observed density peaks for water are shown by red dashed lines [Ho, 2013].

Axial density profiles of the water oxygens and hydrogens depicted in Figure 2-2 were not included in the original manuscript, but for comparison it is worthwhile to discuss them here. On water oxygen profile, two distinct peaks up to cca 1 nm above the surface are visible. In uncharged system, the first peak is positioned at 0.333 nm and the second one at 0.625 nm. In their experimental and theoretical study, Zhou *et al.* [Zhou, 2012] have derived from X-ray measurements positions of the first and second peak of the water to be 0.319 and 0.633 nm above the graphene surface. Thus, our results are just 0.015 and 0.008 nm off the experimental ones. With increasing positive surface charge, position of the first peak uniformly moves toward the surface and its height increase considerably. This is caused by increased

electrostatic attraction between positive surface charge and negative partial charge on the oxygen. Influence of the negative surface charges on oxygen density profile is different. While for surface charge density -0.06 $C.m^{-2}$ the change is rather small with respect to neutral system, for surface charge density -0.12 $C.m^{-2}$ height of the first peak reaches similar values as for +0.12 $C.m^{-2}$.

Water hydrogen profile shows two peaks at 0.334 and 0.664 nm above the uncharged surface. The first peak is positioned at the same distance as water oxygen. Since our axial density profiles have practically the same shape as those in the study by Ho *et al.* [Ho, 2013] (Figure 2-2), we suppose that even in our simulations some of the water molecules within the first hydration layer (~9 %) point one of their OH bonds towards the surface, others having planar geometry with both hydrogens parallel to the surface. Positive surface charge density changes position of the first peak in accordance with the change of the position of the oxygen first peak. Contrary, negative charge density causes more pronounced changes. Negative surface charge attracts positively charged hydrogens and these having no assigned Lennard-Jones parameters start to orient toward the surface with no restriction on how close they can get to the surface. This behavior is represented by peaks emerging at ~0.22 nm above the surface.

2.2 Mercury

Mercury served as an electrode in combined experimental and ab initio study by Dorčák *et al.* (see Chapter 1.2.4) [OK3], whose results were further developed in classic molecular dynamics (CMD) study (Chapter 4.2).

Since mercury is the only common metal which is liquid at ordinary temperatures,

Table 2-1. Lennard-Jones parameters from available mercury models. Final parameters used in our simulations are highlighted by green color.

Ref.	σ_{Hg} (nm)	ε_{Hg} ($kJ.mol^{-1}$)	Parametrization on
Hg0[1]	-	-	Water next to the liquid/solid mercury **benchmark**
Hg1[2]	0.2610	11.10	Liquid bulk mercury
Hg2[3]	0.2969	6.23	Free diffusion of Hg^{2+} in water
Hg3[4]	0.3128	4.04	Hg^0 dimer

[1]Hg0 ref. [Dimitrov and Raev, 2000; Bopp and Heinzinger 1998], [2]Hg1 ref. [Bomont and Bretonnet, 2006], [3]Hg2 ref. [Kuss, 2009] and [4]Hg3 ref. [Munro, 2001].

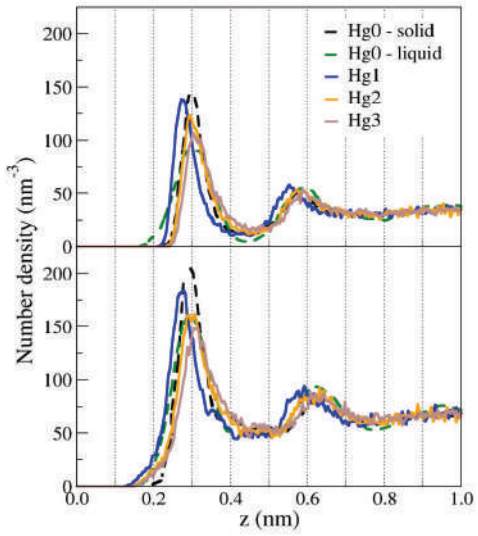

Figure 2-3. Axial number density profiles of water oxygen (top) and hydrogen (bottom) above the mercury surface. Hg0 - solid and liquid represent the benchmark data.

computer simulations of this element based on empirical methods are not easy. Lack of studies is not surprising and only few of them describe mercury using functions which are compatible with biological force fields [Bomont and Bretonnet, 2006; Kuss, 2009; Munro, 2001]. The Lennard-Jones parameters obtained from these works are summarized in Table 2-1. Unfortunately, none of these parameters was parameterized in a study of interactions with biomolecules. Thus, a reproduction of the axial water density profile on mercury was used as a criterion of reliability of the parameters. Results obtained from computer simulations based on ab initio data [Dimitrov and Raev, 2000; Bopp and Heinzinger 1998; noted as Hg0] served for us as a benchmark.

It is clear from the Figure 2-3 that the density profiles are rather insensitive to the choice of Lennard-Jones parameters, however slight differences in positions and heights of peaks can be found. The Hg2 parameters were selected for our further study due to the best reproducibility of ab initio data. The rigid solid mercury surface was used systematically in all our simulations. It was shown by Bosio *et al.* [Bosio, 1979] and Porter and Zinn [Porter and Zinn, 1993] that liquid mercury surface is smooth down to the atomic level with average Hg-Hg distance very close to the distance found in bulk mercury (appr. 3.0 Å), and can be approximated by a solid α-mercury lattice. The final surface atom density of mercury surface was 11.7 atoms.nm^{-2}.

2.3 Quartz (101)

Quartz surface was extensively studied by us [OK1] and new partial charges that extend original ClayFF force field [Cygan, 2004] to be able to describe deprotonated surfaces were presented in our study.

Silicon dioxide with all its crystalline and amorphous modifications is one of the most abundant materials of Earth's crust. α-quartz (α-SiO_2) is a crystalline form of silicon dioxide, which can be found in soils, clays, and rocks and constitute about 20% of the Earth's exposed crust. α-SiO_2 is very important for environmental applications as well as for mimicking laboratory experiments (e.g. oligonucleotides or other molecules attached to glass surface).

Quartz surface exposed to water is covered with rather strongly acidic hydroxyl groups, silanols, that become partially deprotonated above the point of zero charge. It has been suggested that the pH_{pzc} at the point of zero charge (PZC) for quartz is approximately 2.0−4.5 (Figure 2-4). As the pH is increased, the number of deprotonated silanols and the negative charge of the surface increase and the properties of the surface and the interface change considerably.

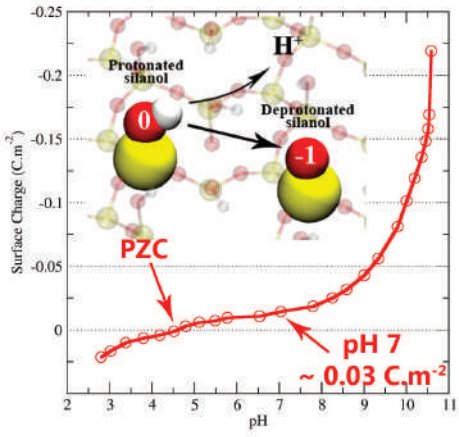

Figure 2-4. Charging curve of the α-quartz surface. Inset: scheme of the deprotonation reaction.

From this point of view it was rather surprising, that for neutral crystalline and amorphous forms of SiO_2 there were several force fields available, whereas force fields that incorporate deprotonated silanol groups were rare [Hassanali, 2010; Butenuth, 2012; Emami, 2014]. Moreover, some of these force fields used terms that were incompatible with common biomolecular force fields (see also Chapter 2.4) and hardly implementable to standard simulation packages like Gromacs or Amber.

For this reason we modified the well established ClayFF force field to be able to model charged quartz surfaces properly. Based on ab initio cluster calculations, we proposed method how to redistribute remaining partial charge after deprotonation and we have tested our new modification against experimental data. Results were quite encouraging, giving good agreement between simulation and experiment in positions of the water and ions above the charged surface. The availability of the modified force field allowed us to carry out much more realistic simulations of quartz compared to existing models of neutral surface (see Chapter 3.2)

2.4 Rutile (110)

Rutile (110) surface was extensively studied by Předota *et al.* in series of papers that have focused on water behavior at the rutile interface [Předota, 2004], ions at the rutile interface [Předota, 2004] and viscosity and diffusivity measurements at the rutile interface [Předota, 2007].

Matsui and Akaogi (MA) parameters [Matsui and Akaogi, 1991] (originally developed to model bulk properties of TiO_2) have been used by Předota for a rutile/water interface in combination with SPC/E water model [Berendsen, 1987]. It was proved, that MA model gives very good agreement with the experimental data, although originally derived for different application. Unfortunately, MA parameters are unsuitable for simulations in standard MD packages (Gromacs, Amber, Charmm) in combination with standard force fields for (bio)molecules. The reason is Buckingham potential (Equation 1-4) used in MA model to describe van der Waals interaction between Ti and O atoms of the surface. Unfortunately, biomolecular force fields use almost exclusively Lennard-Jones potential (Equation 1-2) to describe van der Waals forces and combination of both potentials is extremely demanding in terms of computation time and preparation of the cross interaction tables. At least two publications [Brandt and Lyubartsev, 2015; Luan, 2015] have dealt with this problem and have tried to fit MA parameters with Lennard-Jones potential.

Table 2-2 shows that at the end both studies have reached similar values of ε and σ parameters and shapes of fitting Lennard-Jones curves match original Buckingham potentials with similar accuracy. None of the mentioned studies has focused on rutile (110) albeit it was shown [Fenter, 2000] that this crystallographic face is the most abundant in nature. For that reason we had to test these new fitting parameters and

Table 2-2. Buckingham potential parameters and Lennard-Jones potential parameters for titanium and oxygen atoms in

	Matsui-Akaogi[1]			Brandt-Lyubartsev[2]		Luan-Huynh-Zhou[3]	
	A $(kJ.mol)^{-1}$	b (Å)	C $(kJ.mol^{-1}.Å^{-6})$	σ (nm)	ε $(kJ.mol^{-1})$	σ (nm)	ε $(kJ.mol^{-1})$
Ti-Ti	3002664	0.154	506	0.1958	2.542	0.1960	2.427
O-O	1136872	0.234	2916	0.2875	1.390	0.2887	1.297
Ti-O	1636167	0.194	1215	0.2417	1.880	0.2423	1.774

[1] ref. [Matsui and Akaogi, 1991], [2] ref. [Brandt and Lyubartsev, 2015], [3] ref. [Luan, 2015]

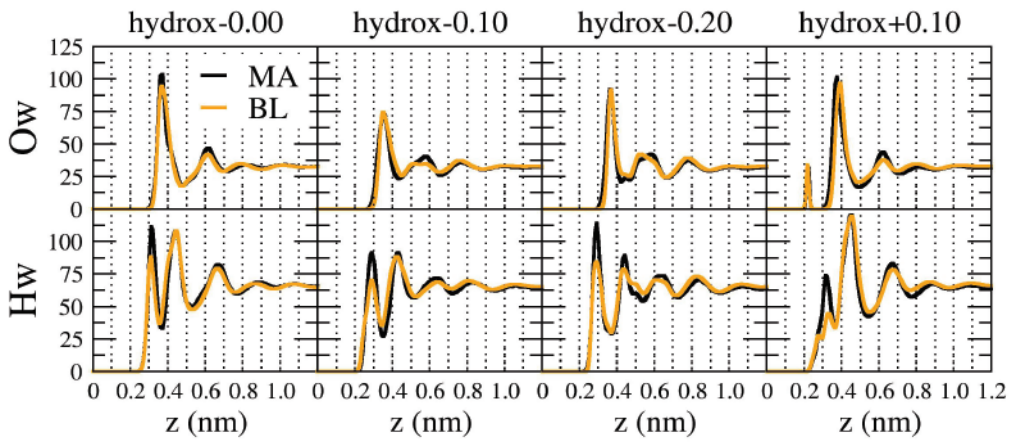

Figure 2-5. Comparison of the water oxygen (top) and hydrogen (bottom) axial density profiles extracted from simulations with Matsui-Akaogi parameters (black lines) and Brandt and Lyubartsev parameters (orange lines). Hydroxylated TiO_2 (110) surfaces with surface charge densities 0.00, -0.10, -0.20 and +0.10 $C.m^{-2}$ were used as substrates.

compare new results with those using original MA model. Due to complexity of the published data, we have decided to test parameters of Brandt and Lyubartsev (BL) [Brandt and Lyubartsev, 2015].

Figure 2-5 shows water oxygen and hydrogen axial density profiles at the TiO_2 (110) surfaces with various surface charge densities. Comparison of original data from Předota *et al.* [Předota, 2004a; Předota, 2004b] and new data based on Brandt and Lyubartsev fit indicates that for oxygen, satisfactory agreement is obtained. In all systems, second peaks are slightly lower with BL and the one in the system with positive surface charge is shifted by 0.02 nm to higher values. Water hydrogen distribution is more sensitive to the choice of potentials. First peaks are lower with BL, indicating somewhat different orientation of water molecules in the first adsorbed layer.

Distributions of sodium and chloride ions were compared too (Figure 2-6). Sodium ions give good agreement between original and fitted parameters, however height of the peaks is slightly lower with BL. Although not so important for the systems with negative surface charges (notice the different vertical scales in Figure 2-6), differences in distributions of chloride ions for the original and fitted parameters are greater. First peaks are underpopulated with BL while second peaks are higher with BL than with MA. The same holds true for second and third peaks in the system with positive surface charge,

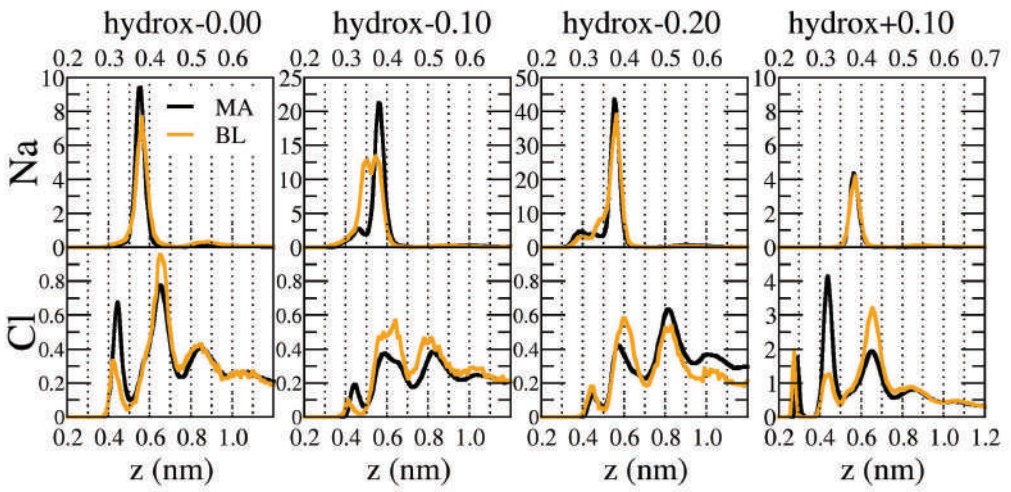

Figure 2-6. Comparison of the sodium (top) and chloride (bottom) axial density profiles from simulations with Matsui-Akaogi parameters (black lines) and Brandt and Lyubartsev parameters (orange lines). Hydroxylated TiO_2 (110) surfaces with surface charge densities 0.00, -0.10, -0.20 and +0.10 $C.m^{-2}$ were used as substrates. Note different *x* and *y* scales.

while positions and heights of the first peaks are comparable for both sets of parameters used.

It is clear that simulations with new parameters slightly differ from those with original Matsui-Akaogi parameters. New parameters slightly underestimate strength of the non-bonded interactions giving less populated first peaks, mainly for water hydrogen and chloride. On the other hand, simulations with new parameters result in very similar results for water oxygen and sodium ions. Despite these deviations, both force fields comparably well agree with experimental data, where available. Because of advantages of using Lennard-Jones potential with Brandt and Lyubartsev parameters for studying interactions with standardly parameterized molecules, we have used these fit parameters in consequent study on oxalate adsorption on rutile surface (for oxalate parameterization see Chapter 3.1).

2.5 Discussion

Due to their similarities and differences, it is worthwhile to draw a comparison between graphene and mercury surfaces and, similarly, between quartz and rutile surfaces. All the studied surfaces have in common exploration of the effect of electrostatics on the behavior of liquid phase including ions and molecules present, namely surface charge or applied voltage in a simulation cell. As mentioned previously, on the metal oxide surfaces charging naturally arises from deprotonation of the surface hydroxyl groups. On metal/metalloid surfaces, charging can be realized by putting partial charge on surface atoms (used in the case of graphene) or by switching up electric field in a simulation cell (used in the case of mercury). All used surface charge densities and corresponding electric fields are summarized in Table 2-3. We used Equation 2-1 to relate surface charge density with electric field:

$$\sigma = E\varepsilon_0 \tag{2-1}$$

where σ is surface charge density in C.m^{-2}, E is electric field in V.m^{-1} and ε_0 is permittivity of vacuum.

2.5.1 Graphene vs. mercury

Graphene and mercury surfaces were used as monoatomic layers in our simulations. While in the graphene case carbon atoms were held together by bond and angle potentials, in the mercury case the initial α-mercury lattice was kept frozen during simulations and mercury atoms were treated as solid Lennard-Jones spheres. Final Lennard-Jones

Table 2-3. Surface charge densities σ and electric field intensities E used in simulations with different surfaces. Similar surface charge densities are highlighted by orange and blue color, respectively.

Graphene		Mercury		Quartz (101)		Rutile (110)	
σ (C.m^{-2})	E (V.nm^{-1})	σ (C.m^{-2})	E (V.nm^{-1})	σ (C.m^{-2})	E (V.nm^{-1})	σ (C.m^{-2})	E (V.nm^{-1})
0.000	0.00	0.000	0.00	0.000	0.00	0.000	0.00
±0.059	3.33	±0.001	±0.14	-0.030	-1.69	0.100	5.65
±0.118	6.66	±0.011	±1.25	-0.060	-3.39	-0.100	-5.65
±0.297	16.77	±0.030	±3.45	-0.120	-6.78	-0.200	-11.29
±0.594	33.54	±0.061	±6.89			-0.400	-22.59

parameters for graphene carbon atoms were σ_{CC} = 0.340 nm, ε_{CC} = 0.360 kJ.mol^{-1}, and σ_{Hg} = 0.2969 nm, ε_{Hg} = 6.23 kJ.mol^{-1} for mercury atoms.

The differences in σ and ε parameters as well as differences in surface charging reflect in behavior of water at the studied surfaces (Figure 2-7). In uncharged systems, water is closer to mercury surface by 0.033 nm compared to graphene. Situation is the same for both oxygen and hydrogen. On mercury surface, the peaks are higher, indicating greater water structuring. Non-zero surface charge reduce the difference in positions and heights of the peaks between graphene and mercury surface. Interestingly, despite different charging method both surfaces give similarly pronounced small peak around ~0.22 nm on Hw axial density profile.

2.5.2 Quartz vs. rutile

Both surfaces have some characteristics in common: surface hydroxyl groups, charging via partial deprotonation of these groups and several types of the hydroxyl groups. Surface number density of the hydroxyl groups on quartz and rutile is 5.8 and 10.4 OH.nm^{-2}, respectively, i.e. rutile surface carries almost two times more hydroxyl groups on its surface.

To quantify the adsorption, we plot in Figure 2-8 the dependence of the amount of adsorbed ions (considering inner-sphere adsorption and first peak of outer-sphere adsorption) on surface charge density for both quartz (101) and (110) rutile surfaces

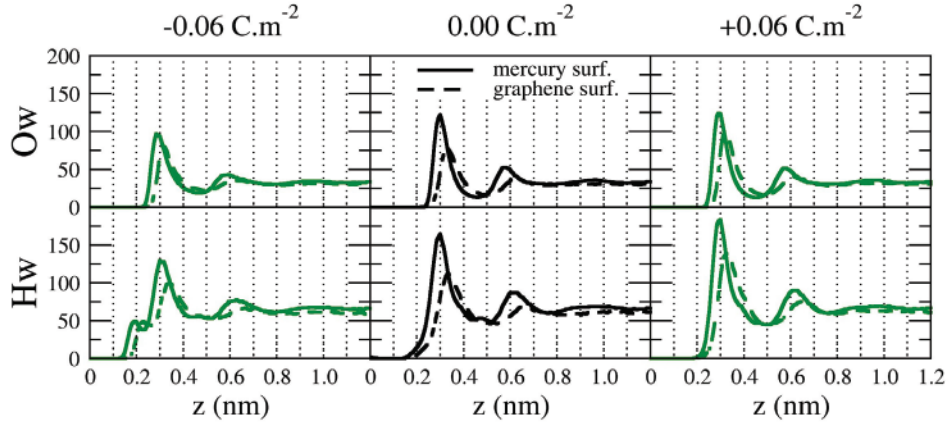

Figure 2-7. Comparison of the water oxygen (top) and hydrogen (bottom) axial density profiles on mercury (full line) and graphene (dashed line) surfaces with various surface charge densities.

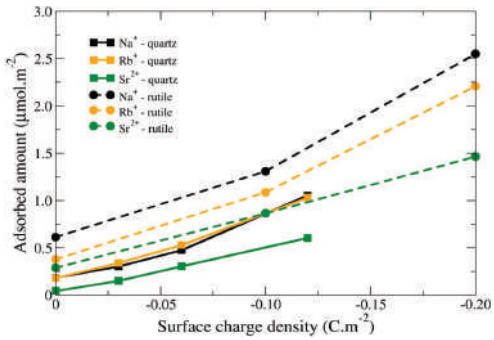

Figure 2-8. Dependence of the adsorbed amount of sodium (black), rubidium (orange), and strontium (green) ions on surface charge density. Data for rutile (dashed lines) surface are taken from Table 8 of Předota *et al.* [Předota, 2013]

[Předota, 2013]. Adsorption on rutile is stronger compared to quartz for all ions. Differences are bigger for neutral surfaces where the rutile surface adsorbs 3.3, 2.1, and 6.6 times more sodium, rubidium, and strontium ions, respectively, than the quartz surface. With increasing surface charge density these ratios decrease. Rutile has higher selectivity to different ion species, with Na^+ adsorption being larger than that of Rb^+ and Sr^{2+} on all surfaces. On quartz, the adsorption of sodium and rubidium is practically the same, but the adsorption of Sr^{2+} is much lower, particularly on the neutral surface. The experimental value of adsorbed rubidium on quartz in the first two adsorption layers is 0.23 ± 0.03 Rb/A_{UC} (where $A_{UC} = 0.338$ nm^2 is the area of a unit cell along the (101) plane) [Bellucci, 2015]. Our simulations predict a value of 0.20 Rb/A_{UC} when integrating over the first two well-pronounced peaks or 0.24 Rb/A_{UC} if even the third peak (up to 0.93 nm from the surface) is taken into account.

3. Physisorption of organic molecules and nucleobases

3.1 Oxalic acid parameterization

Unlike standard biomolecular residues (e.g. amino acids, DNA nucleotides, carbohydrates, etc.), small organic molecules have to be parametrized prior to use in simulations. As we witnessed, this step can be non-trivial. Unsuitable bonding parameters together with inappropriately-optimized partial charges and Lennard-Jones parameters can lead to distorted structures, too strong or weak interactions with water and ions, too high or low affinity to the surface, etc. Thus, one has to take care while parameterizing new residues. In the case of nucleobases (Chapter 1.2.2) standard RESP procedure [Cornell, 1993] to get partial charges was sufficient since these molecules are quite standard and represent subunits of the well-parameterized nucleotides. In the case of oxalic acid and its anions, situation was more complicated and required more complex approach.

3.1.1 Simulation setup

Periodic boundary conditions AIMD simulations based on Born-Oppenheimer approximation were carried on using a hybrid Gaussian plane-wave method (GPW) implemented in CP2K software. Charge density cut-off of 400 Ry with NN50 smoothing was used in all simulations. BLYP functional with the empirical dispersion term for the main group elements was used in conjunction with double-ξ molecularly optimized basis functions augmented by polarization function (DZVP) and appropriate pseudopotential of Goedecker, Teter and Hutter (GTH). All hydrogens were replaced by deuterium to reduce quantum effects of the hydrogen nuclei and to increase the time step. Each simulation box

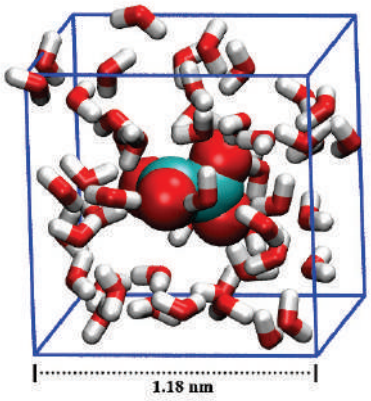

Figure 3-1. AIMD simulation setup. Oxalate dianion by vdw spheres and water by licorice representation.

(Figure 3-1) was composed of (hydrogen) oxalate anion and 50 heavy water (D_2O) molecules. The net charge of the system was compensated by the neutralizing background charge. Production runs were carried out within NVT ensemble with a Nosé-Hoover thermostat and time step of 1 fs. A temperature was set to 300 K and each trajectory was 30 ps long.

Classical MD simulation in NVT ensemble had been performed during parametrization phase with one oxalate ion and 918 water molecules. The net charge of the system was compensated by the neutralizing background charge. Simulation step was set to 1 fs, temperature to 300 K and trajectories had been 2.5 ns long. *Gaff* force field with partial charges derived by standard RESP procedure had been used both for oxalate and SPC/E model of water.

3.1.2 Results

First, we have focused on both forms of oxalic acid anions, i.e. hydrogenoxalate anion and oxalate dianion, in computational study that has combined ab initio optimizations with ab initio molecular dynamics [OK4]. We have confirmed that the most stable conformation of oxalate dianion both in gas phase and in the implicit solvent is the staggered D_{2d} form. From AIMD calculations we have seen that the rotational barrier around C-C bond can be relatively easily overestimated in the explicit solvent. Preferred conformation remains the staggered one in explicit solvent, but it can partially deviate (~20°) from the ideal value. Regarding hydrogenoxalate anion, we have found discrepancy between implicit and explicit solvent calculations: while implicit solvent (and gas phase) calculations predicted global minimum to be the planar structure (*ox-1-closed* in Figure 1-1), where hydrogen of COOH group is involved in intramolecular hydrogen bond with neighboring COO^- group, the AIMD calculations predicted staggered conformation in the presence of more than 8 water molecules and in the bulk. The rotation around C-C bond was almost free at the room temperature in the bulk. It was shown that the solvation pattern around negatively charged carboxylate group is very similar for both anions with approximately 2.5 water molecules around each oxygen, and number of water

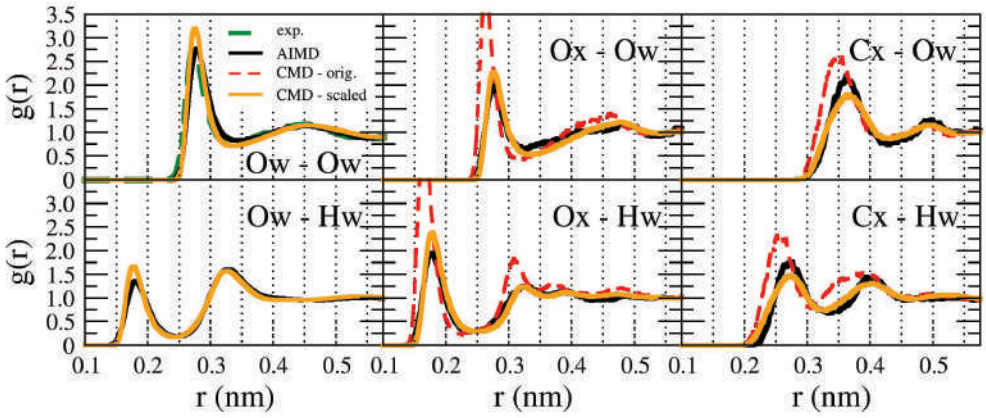

Figure 3-2. Radial distribution functions between water oxygen (top)/hydrogen (bottom) and oxalate dianion oxygen and carbon. Comparison between AIMD data (black), CMD fit with full charges (red, dashed) and scaled charges (orange). Ox stands for oxalate oxygen and Cx for oxalate carbon, respectively.

molecules in the first solvation shell (~15) was found to be the same for both anions and in the agreement with previously reported data [Rosas-García, 2013; Gao and Liu, 2005].

With AIMD data serving as a benchmark, we have designed new model of an oxalate dianion. Standard RESP procedure combined with Antechamber routine was applied to get partial charges and all bonding and nonbonding parameters. However, resulting model showed exceptionally strong interactions with water (Figure 3-2) and ions (Figure 3-3), as indicated by red dashed curves in both graphs. Especially overshooting of interaction with sodium ion could lead to unrealistic adsorption behavior. This is probably caused by relatively large charge localized on two functional groups close to each other. Thus, we have adopted the concept of MDEC (Molecular Dynamics in Electronic Continuum), alternatively

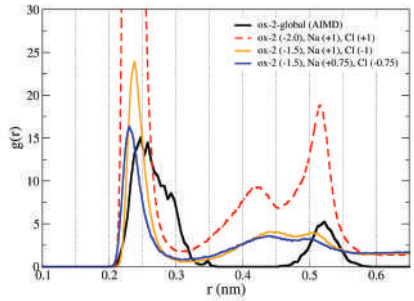

Figure 3-3. Radial distribution functions between oxalate oxygen and sodium cation. 10 ps long AIMD run (black) is compared to CMD simulations with full charges on all ions (red, dashed), scaled charges on oxalate (orange) and scaled charges on all ions (blue).

also called ECC (electronic continuum correction), [Leontyev and Stuchebrukhov, 2012] and according to this concept we have scaled down all partial charges on an oxalate dianion to give 75% charge of the ion, in this case -1.5e. Resulting rdf's between oxalate oxygen/carbon and water oxygen/hydrogen are in good agreement with AIMD data (Figure 3-2). Similarly, interaction with sodium ion has improved considerably (Figure 3-3). In our final choice, charge on sodium ion is scaled down to +0.75e and agreement between CMD and AIMD is even better.

3.2 Physisorption of nucleic acid building blocks

We have focused on studying interactions of nucleobases with quartz (101) surfaces of various charge to bring molecular modeling much closer to real conditions. The main goal is to provide a detailed description of the binding behavior of the four nucleobases (guanine, cytosine, adenine, thymine) to see the influence of the surface charge, to show the best binding arrangement, and to quantify the strength of their interactions with the inorganic surface. Simulated quartz surfaces cover the surface charge densities 0.00, -0.03 and -0.06 C.m^{-2}, approximately corresponding to pH values 4.5, 8.5 and 9.5.

3.2.1 Simulation setup

For simulations of a nucleobase adsorption, we prepared box with dimensions 5.50 × 3.98 × 24.00 nm (Figure 3-4) and two quartz (101) slabs with equally charged (or neutral) surfaces positioned in the middle of the box. The gap between slabs (~5.3 nm) was filled with 1 nucleobase (~ 0.01 M), sodium and chloride ions (giving conc. 0.13 M) and approx. 5400 water molecules. Modified ClayFF force field for quartz [OK1] was used in combination with SPC/E water model. Amber99SB force field for nucleobases was completed by partial charges generated by RESP procedure.

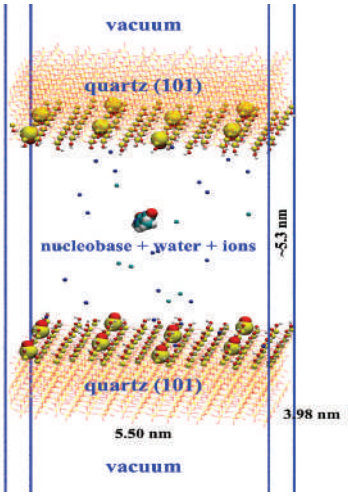

Figure 3-4. Simulation setup. Silanol groups shown by a ball-and-stick and deprotonated silanols by vdw spheres.

Simulation protocol consisted of and equilibration phase in NVT (200 ps) and NPT ensemble (200 ps), followed by production run in NVT ensemble for 100 ns. Time step was set to 2 fs and temperature to 298 K. Other setting were similar to those in [OK1].

3.2.2 Results

During 100 ns runs nucleobases have undergone several adsorption/desorption events on both quartz surfaces in the simulation cell. We have plotted *z* coordinate of the center of mass of the nucleobases and using these plots we have determined borders limiting adsorption event. Structures within these limits were analyzed.

Bivariate plots can unambiguously describe orientation of the nucleobase above the surface [Jedlovszky, 2006]. Bivariate plot is a combined plot of two angles, one between vector *p* and *z* axis and second between vector *o* and *z* axis. Both vectors are depicted in Figure 1-2. Adenine is the only nucleobase without oxygen in the structure and shows the most distinctive adsorption motifs among studied nucleobases (Figure 3-5). For neutral surface, there is one characteristic adsorption structure around angles (75, 20) indicating binding motif with N7 atom and NH_2 group making hydrogen bonds with silanol group.

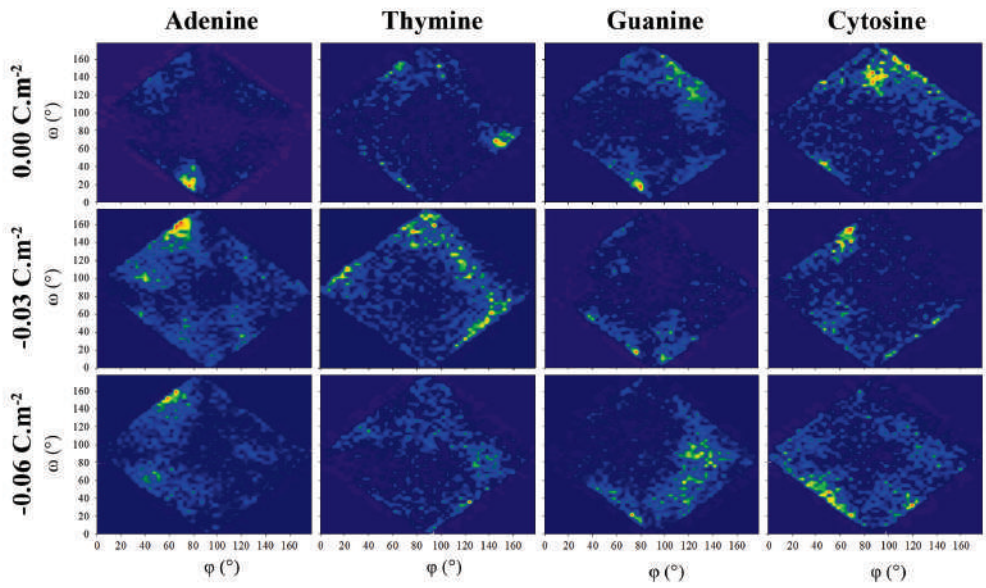

Figure 3-5. Bivariate plots showing orientation of the adsorbed nucleobases. φ is an angle between vector *p* and *z* axis and ω is an angle between vector *o* and *z* axis. For definition of the vectors see Figure 1-2.

On surfaces with charge densities -0.03 and -0.06 $C.m^{-2}$, adenine behaves similarly being adsorbed by N9H group (70, 160). Thymine is remarkable due to its bulky hydrophobic CH_3 group. Thymine interacts by N1H group and O2 with uncharged surface (160, 80) with second maximum around (70, 150), i.e. interaction by N1H group. On -0.03 $C.m^{-2}$ surface, thymine shows wide scale of adsorption motifs, going from O4 through N3H and O2 to N1H group. Adsorption motif of thymine on -0.06 $C.m^{-2}$ surface is hardly recognizable. Guanine on neutral surface binds mainly by its nitrogen groups N9H, N3 and NH_2 (120-140, 120-140), accompanied by portion of structures adsorbing by O6 atom (80, 20). The same structure occurs on charged surface, in the case of the -0.06 $C.m^{-2}$ surface completed by structures interacting by NH_2 and N1H (120-140, 20-90). Cytosine interacts mainly by O2, N3 and NH_2 group on uncharged surface having slightly tilted position (90, 140). On -0.03 $C.m^{-2}$ surface the predominant adsorption site is (60, 140) NH_2 group with N3 nitrogen. Contrary, on -0.06 $C.m^{-2}$ surface cytosine interacts the most by its hydrophobic part, i.e. two CH groups (35-70, 30-60).

These preliminary results suggest that each nucleobase behaves uniquely and it is hard to find any unifying binding motif even within purine or pyrimidine bases. The only binding motif occurring in multiple systems is the one where one nitrogen (or oxygen) of nucleobase forms hydrogen bond with hydrogen on one silanol group, and simultaneously NH or NH_2 group binds to oxygen on another silanol. Work on other results, including role of ions or deprotonated silanol groups, is in progress.

3.3 Physisorption of an oxalate dianion

Hydroxylated rutile (110) surface with new parameters by Brandt and Lyubartsev (Chapter 2.4) together with oxalate dianion with newly developed parameters (Chapter 3.1) were combined to simulate adsorption of this chemical compound.

We have focused on uncharged and positively charged surfaces, since these particular surfaces are the most attractive for oxalate dianions, as observed experimentally by Ridley *et al.* [pers. comm., 2016].

Figure 3-6a shows plot of the axial density of the oxygen is oxalate above hydroxylated rutile surface with surface charge densities 0.00 and +0.10 $C.m^{-2}$. For comparison, corresponding water oxygen density profiles are included. One can notice that Ox of oxalate can interact with surface very similarly as Ow of water – the position of the first peak (~0.37 nm) is very similar. Regarding the 2nd peak around 0.6 nm, the story can be much more complex for oxalate. First possibility is that this peak represents outer

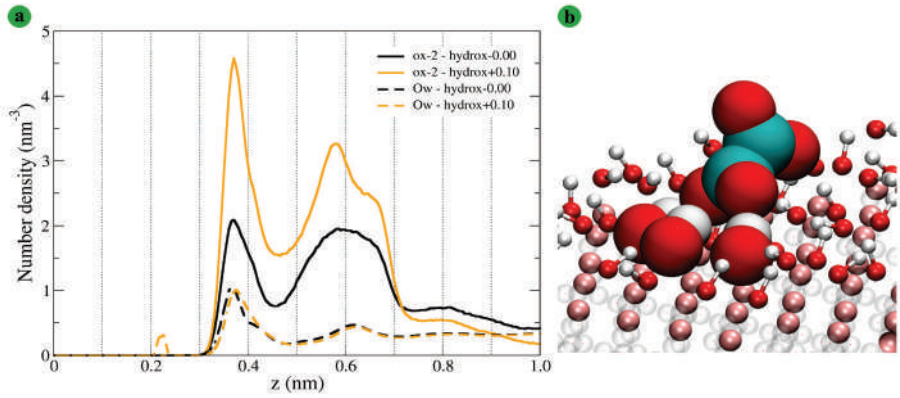

Figure 3-6. (a) Axial density profile of the oxalate dianion on hydroxylated rutile surface with surface charge density 0.00 C.m^{-2} and +0.10 C.m^{-2}, *y* axis values of the water oxygen profiles are scaled down by 100; (b) Snapshot of the typical adsorption motif.

sphere oxalate, i.e. oxygen of oxalate which does not interact directly by any of its (four) oxygens with surface atoms. Alternatively it can represent another oxalate oxygen of oxalate molecule interacting directly with the surface via another oxygen atom. Not surprisingly, oxalate axial density near the surface increases with increasing positive surface charge due to enhanced electrostatic attraction. Figure 3-6b shows snapshot of a typical adsorption configuration.

Further work on this topic is the current focus of the work of doctoral student Denys Biriukov and is beyond the scope of this thesis.

4. Chemisorbed biomolecules

4.1 Chemisorbed nucleic acid on a graphene surface

From the chemical point of view, work on the chemisorbed nucleic acids on graphene surface [OK2], follows and extends work on physisorption of the nucleic acid bases on a quartz surface. This study is tightly connected to biosensing, microarrays or DNA chips, and its main purpose was to investigate the role of the surface charge density in the structure and orientation of covalently attached single-stranded and double-stranded DNAs (Chapter 1.2.3).

The graphene surface (Chapter 2.2) has been selected as the substrate in our simulations, because it is a relatively simple but realistic surface and its structure is independent of pH, salt concentration, etc. Finally, some theoretical studies on DNA interaction with carbon nanotubes (i.e. with surfaces based on graphene geometry) have already been conducted [Hummer, 2001; Lu, 2005; Zhao, 2007; Johnson, 2009]. The binding of DNA to carbon nanotubes has been identified as a way to open the door to carbon-nanotube-based applications in biotechnology [Zheng, 2003].

4.1.1 Simulation setup

Full simulation setup was described in detail in [OK2]. Just few parameters important for comparison with peptide/mercury system (Chapter 4.2) are mentioned here.

Simulation box is depicted on Figure 4-1. Two graphene layers of size of 6.81 × 6.64 nm and separation 6.33 nm enclose space for water, ions, and DNA attached to a charged surface. The role of the second graphene surface, which was always neutral, was to close the system. In order to minimize the influence of the electric field generated by the

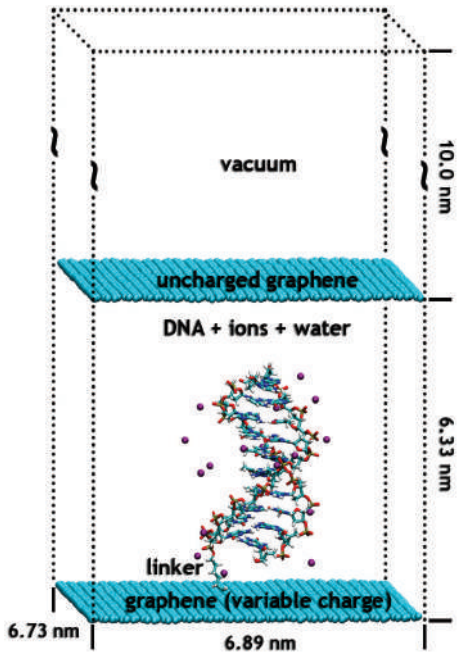

Figure 4-1. A schematic representation of the simulated system.

charged graphene layer on the periodic images, the replicas of the system were separated by a 10 nm vacuum gap. Similar setup was used later for peptide/mercury system (Chapter 4.2).

ds-DNA and ss-DNA decamers with the base sequence 5'-CCACTAGTGG-3' at the canonical B-form were covalently bonded to the graphene layer via an aliphatic carbon linker consisting of six methylene groups (C6). The linker was attached to the 5' end of the cytosine nucleotide by the phosphodiester bond. In the initial position, the DNA helix axis was orientated perpendicularly to the graphene slab.

In order to test the role of the charge of the graphene layer on the position and the orientation of the DNA, all of the carbon atoms of the graphene layer, to which DNA is anchored, were charged to one of the following values: -0.1, -0.05, -0.02, -0.01, 0, +0.01, +0.02, +0.05 or +0.1 elementary charge (e) per carbon, corresponding to the range of the surface charge densities -0.594 to +0.594 $C.m^{-2}$ (see Table 2-3) comparable to those used in the experiment. The sodium/chloride ions were used in order to neutralize fully the charge applied on the graphene, whereas the DNA was neutralized independently by sodium cations.

All of the molecular dynamics simulations were carried out with an atomic resolution including all the hydrogens and in explicit water. An equilibration protocol consisted of a series of energy minimizations and short restrained NPT MD runs. The equilibration phase was followed by an NVT MD production run at 298 K. The restraint of 10 $kcal.mol^{-1}.Å^{-2}$ on all of the graphene atoms was used for the production run in order to keep the graphene layer planar during the simulations. The separation of the two graphene layers in the *z*-direction, 6.33 nm, was sufficient to prevent the interaction of the 3'-DNA terminus with the neutral graphene layer. Each trajectory covered 50 ns.

4.1.2 Results

The probe surface excess concentration used in our study $\Gamma_P = 3.32 \times 10^{-12}$ mol.cm^{-2} was selected to be of the same order of magnitude as a microarray maximum sensitivity for a 10-mer long probe ($\Gamma_P = 9.96 \times 10^{-12}$ mol.cm^{-2}) [Vainrub and Pettitt, 2003]. Probe surface excess concentration used in peptide/mercury study (Chapter 4.2) was comparable, $\Gamma_P = 2.68 \times 10^{-12}$ mol.cm^{-2}.

For comparison with peptide/mercury system just results for ss-DNA are highlighted here. Detailed results can be found in the original manuscript [OK2].

The ss-DNA exhibits ordered stacked helical structure if left free in solution, but it shows localized structural collapse when a graphene layer is present, even if it is not charged. In neutral system, interactions between the surface and the ss-DNA confirm both the experimental and theoretical results, that more bases than merely the first one are adsorbed to the surface because of the higher flexibility of the ss-DNA.

For low negative charge density (-0.01e), an attractive dispersion interaction between the closest base and the graphene layer (majority of the simulation) and attraction of the polar amino group of the closest cytosine and the graphene (shorter periods of the simulation) was seen. For the medium negative charge densities, -0.02 to -0.05e, the electrostatic interactions become the leading factor for the stabilization of the DNA-graphene complex and the attraction of the amino group of the closest cytosine and the surface is crucial. In addition to these interactions, in the -0.05e system, the interaction of the negatively charged sugar-phosphate backbone in the middle part of the ss-DNA with the counterions localized close to the surface is observed as well. In systems with the highest applied negative charge density on the graphene (-0.1e), an oppositely charged layer of counterions was formed and a strong attraction of the phosphates with the sodium cations was observed immediately after the beginning of the simulation.

In the system with lowest positive surface charge (+0.01e), approximately after 10 ns of the simulation the whole ss-DNA is localized close to the surface and interacts via phosphates (by electrostatic forces) and as well as with majority of its bases (by dispersion forces) with the surface. When the charge of the carbons in graphene is changed to +0.02e, the electrostatic attraction between the phosphates and the surface causes a parallel orientation of the DNA already in the early stage of the simulation. In addition, an electrostatic interaction of the guanine with the surface mediated via the O6 oxygen atom of the base is observed. Occasionally, one or few bases still interact with the surface by dispersion forces. For the system containing graphene with a charge of +0.05e on the carbon atoms, the electrostatic forces attracting the phosphates to the surface are crucial,

but it takes about 10 ns before the parallel orientation of the DNA with the surface is reached (probably owing to the presence of a non-negligible amount of chloride anions next to the surface). At the surface with a charge of +0.1e, the ss-DNA remains extended and perpendicularly orientated to the graphene surface covered by an almost immobile layer of counterions (Cl^-) at the beginning of the simulation. This rather strong repulsion between the chloride anions and phosphates leads to the extension of the linker as well as the DNA.

4.2 Chemisorbed peptides on a mercury surface

Having experience with simulations of graphene surface and chemisorbed oligonucleotides, we have joined experimentalists J. Vacek (Department of Medical Chemistry and Biochemistry, Palacký University Olomouc) and V. Dorčák (Institute of Biophysics, Brno) who have studied peptides on mercury electrode by label-free electrochemical method called constant-current chronopotentiometric stripping (CPS, Chapter 1.2.4). Method was described in detail in experimental and theoretical study by Dorčák *et al.* [OK3]. In this study, proton transfer ability of peptidic H-wires was characterized experimentally in an adsorbed state using an approach based on a label-free electrocatalytic reaction. The experimental findings were complemented by theoretical calculations on the ab initio level in vacuum and implicit solvent. Experimental and

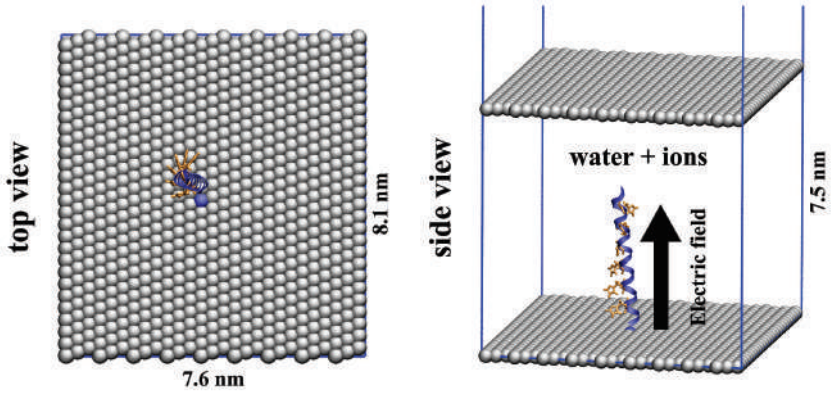

Figure 4-2. Initial configurations of studied systems. Top and side view of the simulation box. Histidine residues are highlighted by orange color and licorice representation, anchoring surface mercury atom is highlighted by blue color.

theoretical results indicated $Ala_3(His\text{-}Ala_2)_6$ to be a high proton-affinity peptidic H-wire model.

As a follow-up to experimental and ab initio results, we continued with MD simulations. Our task was to prepare and simulate systems with different surface charge densities, with different densities of the chemisorbed peptides and with different protonation state of the histidine residues to show how these three parameters influence conformations and dynamics of the peptide strands covalently attached to mercury surface. Our findings should support experimental data [OK3] and give detailed insight on the molecular level.

4.2.1 Simulation setup

Verification of the proper parameters for the mercury surface was described earlier in Chapter 2.2.

The simulated system is depicted in Figure 4-2. All the simulations were carried out in a periodic box with dimensions 7.6 × 8.1 x 100.0 nm. Water, ions and peptide were confined between two solid monolayer mercury surfaces; one surface was positioned at z = 0 and the second one in z = 7.5 nm. Similarly to previous study with graphene surface, role of the upper surface was to close the system. Overall height of the simulation box was set to 100 nm to suppress influence of the applied electric field on images of basic simulation box in z direction. A 21-mer peptide of sequence AAA HAA HAA HAA HAA HAA HAA peptide (Figure 4-3a) was covalently anchored to the mercury surface through modified cystein residue. Two possible protonation states of histidine residues were systematically employed in our simulations (Figure 4-3b): a) all histidines were neutral with proton on ε-nitrogen atom of the imidazole ring (system abbreviated as "HIE" in the following

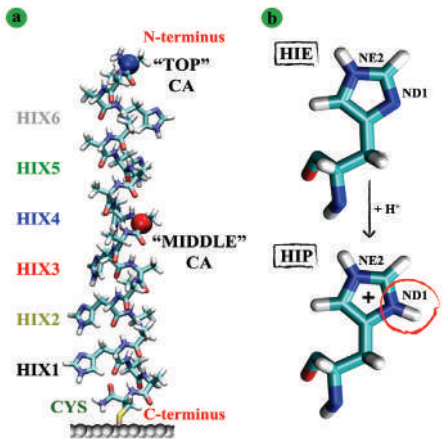

Figure 4-3. a) Top CA carbon atom (blue) and middle CA carbon atom (red) used for further analysis highlighted by vdw sheres representation. Color coding of the histidine residues used in following graphs shown on the left; b) Neutral (HIE) and protonated (HIP) histidine residues.

text); b) all histidines were protonated with protons both on ε- and δ-nitrogen atoms of the imidazole ring (system abbreviated as "HIP" in the following text).

The ionic strength of the NaCl solution was set to 0.05 M to mimic usual experimental conditions. The charge on mercury surface was realized by application of the voltage between the mercury surface and opposite wall of the periodic box. The series of voltages -50 V, -25 V, -10 V, -1 V, 0 V , +1 V, +10 V, +25 V, +50 V was applied in the simulations with one peptide strand (for corresponding surface charge densities see Table 2-3). Voltage between two mercury surfaces was generated by setting up the appropriate electric field times the height of the gap between these surfaces (7.5 nm). During 2 ns long equilibration phase only water molecules and ions were allowed to move, while peptide was held in its upright position applying position constraints. Simulation time of the production run was 50 ns for each trajectory. During production run all the molecules except mercury surfaces were allowed to move.

4.2.2 Results

System with only one peptide strand represents limiting situation where interactions with neighbor strands are excluded and the anchored peptide is moving freely under given conditions. Surface excess concentration for this setup is $\Gamma_P = 2.68 \times 10^{-12}$ mol.cm^{-2}, corresponding to the available area for one peptide strand $a_P = 62.06$ nm^2.

HIE system. Time evolution of positions of middle and top points on peptide backbone is depicted in Figure 4-4. The initial conformation oriented perpendicularly to the surface has a tendency to slowly approach the surface and adsorb on it. The center of the peptide started interacting with the surface no later than in 20 ns under any applied electric field. Even the top of the protein in negative and low positive voltages can be found in the vicinity of the surface. Only the highest applied positive voltages (+25 V and +50 V) cause notable fluctuations of this part of the peptide. This can be caused by repulsion between surface and positively charged N-terminus of the peptide. Despite these fluctuations, results clearly indicate an effort of the peptide to maximize the interaction with the surface, no matter what value of the voltage is applied. This view is supported by Figure 4-5a where time evolutions of distances of the imidazole rings from the surface are depicted. Positions of side chains fluctuate notably only when voltage of +50 V is applied, otherwise all the imidazole rings are located no farther than 1 nm from the surface during analyzed time.

HIP system. As one can expect, the electrostatic forces between charged histidines (HIP) and mercury surface influence behavior of the peptide-surface complex.

On the first sight and rather surprisingly, there are not so big differences between orientation of protonated and deprotonated peptide relative to the mercury layer. The time evolutions of their distances from the surface are similar both for HIE and HIP systems for majority of applied voltages (Figure 4-4). Only when highly positive voltages of +25 V and +50 V were used, HIP system shows enhanced fluctuations of its middle part compared to the HIE system with neutral histidines since parts of the peptide are more repealed from the surface forming various kinks and loops. Although the upper end of the peptide is adsorbed on the surface, the central part remains desorbed, making loop with positive histidine residues pointing out of the surface. On the other side, this also illustrates that relatively high positive charge on the surface cannot fully prevent positively charged residues from approaching the vicinity of the surface. Stacking interactions between the surface and the histidine residues as well as the hydrophobic

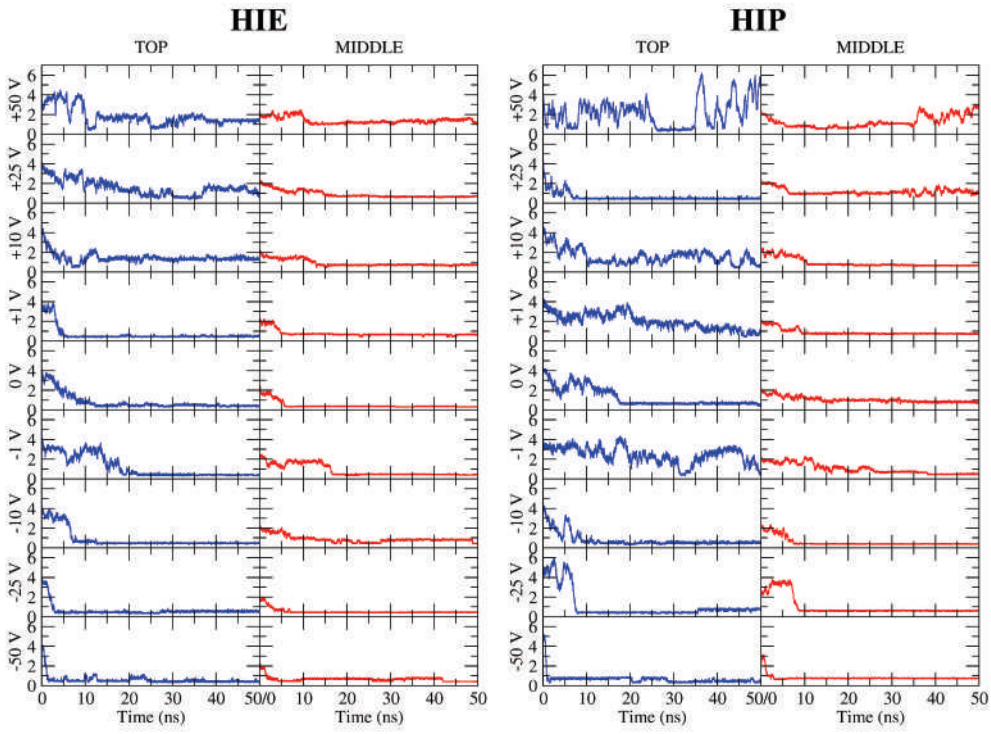

Figure 4-4. Time evolution of the *z* coordinates of the two points on protein backbone for 1 strand system. "TOP" is the CA carbon on the alanine most distant from the surface at the initial configuration; "MIDDLE" refers to CA carbon on middle alanine (see Figure 4-3a). Results in the left column are for deprotonated histidine (HIE), results in the right column for protonated histidine (HIP).

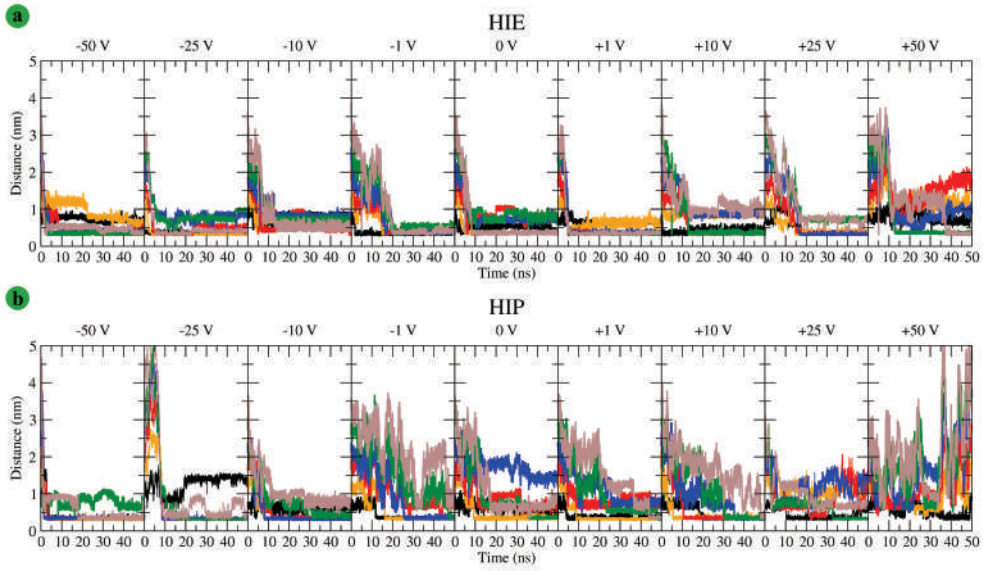

Figure 4-5. Time evolution of the *z* coordinates of the geometric centers of the heavy atoms in imidazole rings. Color coding according to Figure 4-3. (a) for HIE system and (b) for HIP system.

interactions of the alanine residues (CH_3 group) can stand behind this behavior.

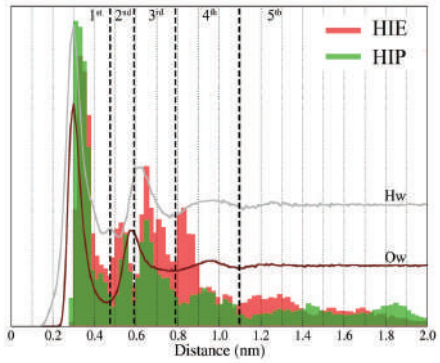

Figure 4-6. Merged histograms of the *z* coordinates of the geometric centers of the heavy atoms in imidazole rings for all applied electric fields. Axial density profiles of water oxygen and hydrogen included.

Graph with time evolution of the *z* coordinates of the geometric centers of the imidazole rings (Figure 4-5b) shows that in the most negative system all imidazole rings except one are located within 0.3 nm from the surface. In -25 V system electrostatics still pushes histidine residues close to the surface and number of the adsorbed species is greater than in the HIE system. While in -10 V system charged histidine residues behaves similarly as in the matching HIE system, starting from -1 V system histidine residues show greater fluctuations and, thus, positions close to the surface are less populated at the expense of the peaks far from the surface. Difference between neutral and charged

histidine residues is most visible for +25 V and +50 V systems, where fluctuations in the HIP systems are considerable.

Position of imidazole rings. If we merge histograms of perpendicular positions of the imidazole rings for all applied voltages in HIE and HIP systems, four well separated peaks appear (Figure 4-6). The same holds true even for HIP system. Peaks are approximately located at regions 0 - 0.47, 0.48 - 0.57, 0.58 - 0.78 and 0.79 - 1.02 nm above the surface. A probable reason for this discrete arrangement of histidine residues is an inability of adsorption of all histidine residues to the surface due to steric reasons and structured water near the surface. Water oxygen density profile is depicted in the same graph as merged histograms (Figure 4-6). One can see that up to ~1 nm imidazole rings are mostly positioned between minima and maxima of the water oxygen density curve. This curve shows two distinct peaks positioned at 0.3 and 0.58 nm, respectively. In the case of HIE system the more distant peaks are more populated due to overall lower affinity of this system to the surface than in HIP system.

4.3 Discussion

There are certain similarities in both studies that dealt with chemisorbed biomolecules. First, in both studies an atomically flat surface with a regular structure was used as a substrate. Second, positive and negative electric fields were applied in both systems and to some extend their intensities overlapped (see Table 2-3). Third, DNAs and peptides with protonated histidines (HIP system) carry significant charge, although one has to keep in mind that these charges have opposite values and are located on different parts of biomolecules (ss-DNA backbone vs. histidine residue). And finally, both used biomolecules contain heteroatomic aromatic rings that can be involved in similar type of the weak intermolecular interactions.

In the following text we will focus on ss-DNA/graphene systems denoted as 0.00, ±0.01 and in the original manuscript [OK2] and on peptide/mercury systems denoted as 0 V and ±50 V in previous chapter, because according to the Table 2-3 these systems have comparable voltage applied in a simulation cell. But it is important to recall different approach to generate electric field in a simulation cell. While in ss-DNA/graphene simulations electric field was generated by partial charges on each carbon atom in a substrate, in peptide/mercury simulations external electric field was applied by switching on corresponding option in Gromacs software. An approach applied in ss-DNA/graphene

simulations required enormous number of the compensating ions in the simulation cell and this could lead (besides other factors) to differences in two studied systems.

Comparing systems with no voltage applied (Figure 4-7, middle graphs) is the most straightforward. One can see that it took ss-DNA molecule almost 40 ns to get close to the surface, while HIP peptide reached the surface in 20 ns. In neutral HIE peptide, middle part of the peptide reached surface even faster, within less than 10 ns. But overall behavior is very similar. Short initial period where ss-DNA/peptide strand remained in upright position was followed by sorption of other nucleobases/imidazole rings and this led after several nanoseconds to a spreading of the strand onto the surface with some nucleobases/imidazole rings stacked and some not. Figure 4-8 illustrates this on snapshots with typical conformations. For ss-DNA this behavior on graphene surface was supported by other experimental and theoretical studies [Hummer, 2001; Zhao, 2007; Johnson, 2009]. In the case of peptide, it is hard to find supporting data due to unusual substrate and specific peptide constitution. It was suggested for pH neutral solution of the histidine amino acids, that the orientation of neutral HIE or charged HIP on the mercury electrode [Słojkowska and Jurkiewicz-Herbich, 1999] was with the neutral imidazole ring perpendicular to the Hg surface and NH_3 group also directed towards the metal. Contrary, study conducted on gold surface concluded, that the HIE molecules are adsorbed through

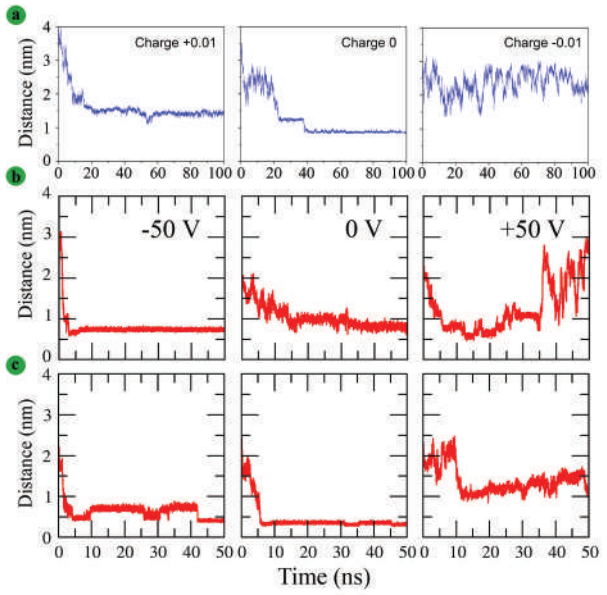

Figure 4-7. The distance of the (a) central phosphorus atom (in nm) of ss-DNA; and (b) middle CA atom of the HIP peptide strand; and (c) middle CA atom of the HIE peptide strand to the graphene and mercury layer, respectively.

the deprotonated nitrogen atom of the imidazole ring and with NH_3 group located nearer to electrode than COO^- [Lim, 2008]. One has to keep in mind, that these studies dealt just with amino acids in solution. Theoretical study on adsorption of the amino acids on the gold substrate [Hoefling, 2010] predicted very high affinity of amino acids with aromatic rings to the gold. Another study [Iori, 2009] also found stronger-than-expected interactions for aromatic amino acids. It was suggested [Hoefling, 2010] that these strong interactions may be caused by π-electron mediated effects and, simultaneously, the planarity of aromatic amino acids allows maximizing the dispersion interaction with the equally planar surface.

Positive voltage in ss-DNA/graphene system has the same effect as negative one in peptide/mercury system (Figure 4-7 and Figure 4-8, left graphs). In +0.01 ss-DNA system,

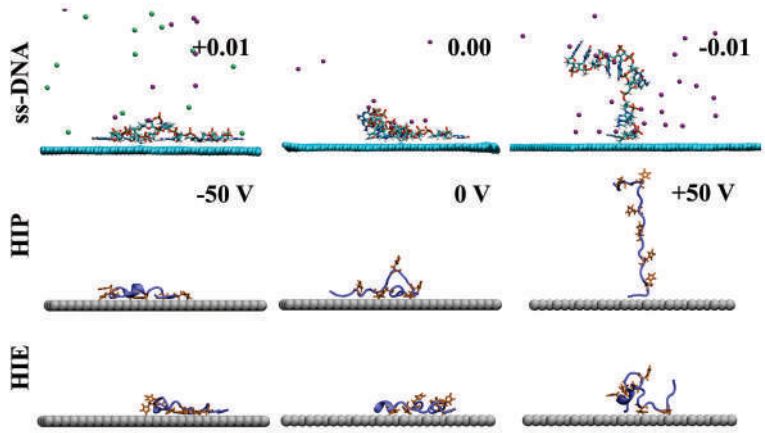

Figure 4-8. The typical conformations of ss-DNA, HIP and HIE peptides after the equilibrium is reached.

ss-DNA benefits from the mutual cooperative effect of the electrostatic and dispersion interactions and after few nanoseconds the whole ss-DNA is localized close to the surface and interacts via phosphates (by electrostatic forces) and as well as with majority of its bases (by dispersion forces) with the surface (80 %, Figure 4-9). In -50 V HIP system, the strands collapse on a shorter time scale (<5 ns) compared to +0.01 ss-DNA, but the number of the adsorbed heterocycles is similarly 80 % (Figure 4-9) and peptide adopts flat conformation as ss-DNA. Lower attraction between HIE system and negative surface compared to HIP system causes lower number of the stacked imidazole rings and structure with several kings.

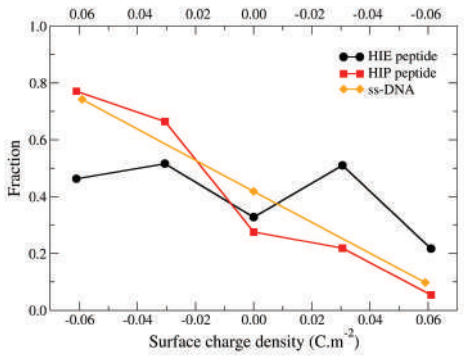

Figure 4-9. Fraction of the adsorbed nucleobases and imidazole rings in ss-DNA/graphene and peptide/mercury systems, respectively. Heterocycles were considered as stacked when N1/NE and N3/ND atoms in their heteroatomic rings were within 0.45 nm from the surface. Upper horizontal scale is for ss-DNA/graphene.

Negative voltage in ss-DNA/graphene system and positive one in peptide/mercury system causes notable fluctuations of the strands (Figure 4-7 and Figure 4-8, right graphs). Electrostatic repulsion plays key role here while stacking interactions are suppressed, especially in the ss-DNA/graphene system. Mutual repulsion of the sugar-phosphate backbone and surface leads to bent structure of the ss-DNA with just first nucleobase stacked onto the surface (Figure 4-9). Peptide systems with negative voltage are highly dependent on protonation state of the histidine residue. Whereas HIE system shows mild response on increasing voltage and structures are still very close to the surface, remarkable fluctuations and upright position can be seen for the highest voltage applied in the HIP system (Figure 4-8). Similarly to negative surface charge, number of the stacked imidazole rings in HIP system is comparable to number of stacked bases in ss-DNA system.

5. Conclusion

This thesis represents author's effort to learn advanced computer modeling methods and to apply them to study interactions of biomolecules with mineral surfaces. Where necessary, auxiliary studies (in terms of the main goal of this thesis, but otherwise representing interesting studies themselves) of interactions of molecules with the aqueous solutions without a presence of surfaces or interactions of water and ions with the surfaces (inevitable to understanding of the adsorption of molecules) were carried out. As a result of this effort three articles on adsorption and two others that dealt with biomolecules in water were published in international peer-reviewed journals. One more is submitted.

Four different surface models were prepared, parameterized and used in simulations. Special effort was paid to the quartz (101) surface that was parameterized to reflect its nature under neutral and basic pH conditions [OK1], i.e. to device models of charged surface corresponding to these conditions. The validity of the quartz and graphene surface [OK2] models was confirmed by comparison with experimental data. In both case, agreement in positions of the structured water molecules above the surface was satisfactory. Fairly good agreement was found in positions of the rubidium ions above the quartz surface, where two experimentally observed peaks were suggested to be completed with one more peak positioned between these two. In the case of the mercury surface, several parameters taken from literature were compared with ab initio derived data. The best matching parameters were used in subsequent study on chemisorption of peptides. Due to compatibility issues, well-established parameters by Matsui and Akaogi for rutile surface were replaced by parameters by Brandt and Lyubartsev that suit better for systems combining inorganic surface with biomolecules. Since good agreement was found, rutile surfaces with implemented Brandt and Lyubartsev parameters were used in subsequent oxalate adsorption study. All prepared models will serve for further simulations in the Předota's group.

Prior to an adsorption study, oxalate dianion and hydrogenoxalate ion were inspected by means of AIMD to get detailed information about structures and solvation shells of these species [OK4]. Oxalate was confirmed to adopt staggered conformation in water. The most stable conformation of a hydrogenoxalate from ab initio optimizations in implicit solvent was denied by AIMD in explicit water environment. Extended analysis supported AIMD results that predicted disruption of intramolecular hydrogen bond and transitions from planar to staggered structure is correct. Solvation shell of both ions was described in detailed and final results served as benchmark for oxalate model parameterization. RESP procedure was used to derive first trial model of an oxalate for CMD. Subsequent tuning of partial charges together with bonded and non-bonded parameters led to new model of oxalate dianion that should behave properly in contact with water and ions.

Preliminary results for physisorption of the oxalate on a rutile surface and nucleobases on a quartz surface were presented here. Different adsorption patterns of four nucleobases were revealed with a help of bivariate plots. Results suggested that each nucleobase behaves uniquely and it is hard to find any unifying binding motif even within purine or pyrimidine bases. Regarding oxalate on rutile surface, it was shown that despite its high negative charge oxalate occupies similar positions as structured water above the surface. An adsorption activity increased with increasing positive charge on a surface. Further work on this topic is currently followed by another doctoral student .

Two published studies dealt with chemisorbed biomolecules: in one of them we studied single- and double-stranded DNA on a graphene surface [OK2] and in other we focused on peptide wires on a mercury surface [OK3]. Study of DNA on a graphene surface outlined the role of surface charge on DNA adsorption and found notable differences in ss- and ds-DNA adsorption. While in ds-DNA electrostatic forces between charged surface and ds-DNA backbone play major role, in ss-DNA stacking interactions become also involved and in particular cases stacking interactions can compete with electrostatic forces, making adsorption of ss-DNAs more varied compared to ds-DNA. In combined experimental and ab initio study [OK3], ability of peptides with particular composition to act like proton wires was confirmed. Subsequent CMD study focused on a more detailed analysis of chemisorbed peptide(s). Mainly the role of the surface charge in combination with different protonation states of the histidine residues was described. While peptides with neutral histidines were found to be rather insensitive to different surface charge, peptides with protonated histidines showed greater sensitivity to surface charge applied.

To summarize, in this thesis the author attempted to demonstrate the applicability of methods of molecular dynamics to describe adsorption of various chemical species (going from water and ions through small organic molecules to larger biomolecules) on various types of inorganic surfaces. Since adsorption events stand behind various natural and artificial processes and experimental techniques, presented results provide information relevant for many fields of biophysics.

References

Baú, J., Carneiro, C., de Souza Junior, I., de Souza, C., da Costa, A., di Mauro, E., Zaia, C., Coronas, J., Casado, C., de Santana, H., Zaia, D., 2012. Adsorption of Adenine and Thymine on Zeolites: FT-IR and EPR Spectroscopy and X-Ray Diffractometry and SEM Studies. Orig. Life Evol. Biospheres 42, 19–29. doi:10.1007/s11084-011-9246-1

Bellucci, F., Lee, S.S., Kubicki, J.D., Bandura, A., Zhang, Z., Wesolowski, D.J., Fenter, P., 2015. Rb^+ Adsorption at the Quartz(101)–Aqueous Interface: Comparison of Resonant Anomalous X-ray Reflectivity with ab Initio Calculations. J. Phys. Chem. C 119, 4778–4788. doi:10.1021/jp510139t

Berendsen, H.J.C., Grigera, J.R., Straatsma, T.P., 1987. The missing term in effective pair potentials. J. Phys. Chem. 91, 6269–6271. doi:10.1021/j100308a038

Bogdan, D., Morari, C., 2012. Electronic Properties of DNA Nucleosides Adsorbed on a Au(100) Surface. J Phys Chem C 116, 7351–7359. doi:10.1021/jp210229e

Bomont, J.-M., Bretonnet, J.-L., 2006. An effective pair potential for thermodynamics and structural properties of liquid mercury. J. Chem. Phys. 124, 54504.

Bopp, P.., Heinzinger, K., 1998. MD studies of electrolyte solution|liquid mercury interfaces. J. Electroanal. Chem. 450, 165–173. doi:10.1016/S0022-0728(97)00638-4

Bosio, L., Cortes, R., Segaud, C., 1979. X-ray diffraction study of liquid mercury over temperature range 173 to 473 K. J. Chem. Phys. 71, 3595–3600. doi:10.1063/1.438817

Brandt, E.G., Lyubartsev, A.P., 2015. Systematic Optimization of a Force Field for Classical Simulations of TiO2–Water Interfaces. J. Phys. Chem. C 119, 18110–18125. doi:10.1021/acs.jpcc.5b02669

Brindley, G.W., Lailach, G.E., Thompson, T.D., 1968. Absorption of pyrimidines, purines, and nucleosides by Li-, Na-, Mg-, and Ca-montmorillonite /clay-organic studies XII/. Clays Clay Miner. 16, 285–293.

Butenuth, A., Moras, G., Schneider, J., Koleini, M., Köppen, S., Meißner, R., Wright, L.B., Walsh, T.R., Ciacchi, L.C., 2012. Ab initio derived force-field parameters for molecular dynamics simulations of deprotonated amorphous-SiO2/water interfaces. Phys. Status Solidi B 249, 292–305. doi:10.1002/pssb.201100786

Butt, H.-J., Graf, K., Kappl, M., 2003. Front Matter, in: Physics and Chemistry of Interfaces. Wiley-VCH Verlag GmbH & Co. KGaA, pp. i–xii.

Carneiro, C.E.A., Berndt, G., de Souza Junior, I.G., de Souza, C.M.D., Paesano, A., Jr, da Costa, A.C.S., di Mauro, E., de Santana, H., Zaia, C.T.B.V., Zaia, D.A.M., 2011. Adsorption of adenine, cytosine, thymine, and uracil on sulfide-modified montmorillonite: FT-IR, Mössbauer and EPR spectroscopy and X-ray diffractometry studies. Orig. Life Evol. Biosphere J. Int. Soc. Study Orig. Life 41, 453–468. doi:10.1007/s11084-011-9244-3

Cleaves, H.J., Jonsson, C.M., Jonsson, C.L., Sverjensky, D.A., Hazen, R.M., 2010. Adsorption of Nucleic Acid Components on Rutile (TiO2) Surfaces. Astrobiology 10, 311–323. doi:10.1089/ast.2009.0397

Cornell, W.D., Cieplak, P., Bayly, C.I., Kollmann, P.A., 1993. Application of RESP charges to calculate conformational energies, hydrogen bond energies, and free energies of solvation. J. Am. Chem. Soc. 115, 9620–9631. doi: 10.1021/ja00074a030

Cygan, R.T., Liang, J.-J., Kalinichev, A.G., 2004. Molecular Models of Hydroxide, Oxyhydroxide, and Clay Phases and the Development of a General Force Field. J. Phys. Chem. B 108, 1255–1266. doi:10.1021/jp0363287

Dimitrov, D.I., Raev, N.D., 2000. Molecular dynamics simulations of the electrical double layer at the 1 M KCl solution | Hg electrode interface. J. Electroanal. Chem. 486, 1–8.

Dorčák, V., Ostatná, V., Paleček, E., 2013. Electrochemical reduction and oxidation signals of angiotensin peptides. Role of individual amino acid residues. Electrochem. Commun. 31, 80–83. doi:10.1016/j.elecom.2013.03.016

Emami, F.S., Puddu, V., Berry, R.J., Varshney, V., Patwardhan, S.V., Perry, C.C., Heinz, H., 2014. Force Field and a Surface Model Database for Silica to Simulate Interfacial Properties in Atomic Resolution. Chem. Mater. 26, 2647–2658. doi:10.1021/cm500365c

Enache, T.A., Oliveira-Brett, A.M., 2013. Peptide methionine sulfoxide reductase A (MsrA): Direct electrochemical oxidation on carbon electrodes. Bioelectrochemistry 89, 11–18. doi:10.1016/j.bioelechem.2012.08.004

Fenter, P., Cheng, L., Rihs, S., Machesky, M., Bedzyk, M.J., Sturchio, N.C., 2000. Electrical Double-Layer Structure at the Rutile–Water Interface as Observed in Situ with Small-Period X-Ray Standing Waves. J. Colloid Interface Sci. 225, 154–165. doi:10.1006/jcis.2000.6756

Feyer, V., Plekan, O., Šutara, F., Cháb, V., Matolín, V., Prince, K.C., 2011. Guanine adsorption on the Cu(110) surface. Surf. Sci. 605, 361–365. doi:10.1016/j.susc.2010.11.002

Francis, S.H., Corbin, J.D., 1999. Cyclic Nucleotide-Dependent Protein Kinases: Intracellular Receptors for cAMP and cGMP Action. Crit. Rev. Clin. Lab. Sci. 36, 275–328. doi:10.1080/10408369991239213

Gao, B., Liu, Z., 2005. First Principles Study on the Solvation and Structure of C2O42-(H2O) n, n= 6-12. J. Phys. Chem. A 109, 9104–9111.

Hassanali, A.A., Zhang, H., Knight, C., Shin, Y.K., Singer, S.J., 2010. The Dissociated Amorphous Silica Surface: Model Development and Evaluation. J. Chem. Theory Comput. 6, 3456–3471. doi:10.1021/ct100260z

Heyrovský, M., 2005. Catalytic Hydrogen Evolution at Mercury Electrodes from Solutions of Peptides and Proteins, in: Emil Paleček, F.S. and J.W. (Ed.), Perspectives in Bioanalysis, Electrochemistry of Nucleic Acids and Proteins – Towards Electrochemical Sensors for Genomics and Proteomics. Elsevier, pp. 657–687.

Ho, T.A., Striolo, A., 2013. Polarizability effects in molecular dynamics simulations of the graphene-water interface. J. Chem. Phys. 138, 54117. doi:10.1063/1.4789583

Hodge, R., 2009. The Molecules of Life: DNA, RNA, and Proteins. Infobase Publishing.

Hoefling, M., Iori, F., Corni, S., Gottschalk, K.-E., 2010. Interaction of Amino Acids with the Au(111) Surface: Adsorption Free Energies from Molecular Dynamics Simulations. Langmuir 26, 8347–8351. doi:doi: 10.1021/la904765u

Hummer, G., Rasaiah, J.C., Noworyta, J.P., 2001. Water conduction through the hydrophobic channel of a carbon nanotube. Nature 414, 188–190. doi:10.1038/35102535

Iori, F., Di Felice, R., Molinari, E., Corni, S., 2009. GolP: An atomistic force-field to describe the interaction of proteins with Au(111) surfaces in water. J. Comput. Chem. 30, 1465–1476. doi:10.1002/jcc.21165

Jedlovszky, P., Předota, M., Nezbeda, I., 2006. Hydration of apolar solutes of varying size: a systematic study. Mol. Phys. 104, 2465–2476. doi:10.1080/00268970600761101

Johnson, R.R., Kohlmeyer, A., Johnson, A.T.C., Klein, M.L., 2009. Free Energy Landscape of a DNA-Carbon Nanotube Hybrid Using Replica Exchange Molecular Dynamics. Nano Lett. 9, 537–541. doi:doi: 10.1021/nl802645d

Jordheim, L.P., Durantel, D., Zoulim, F., Dumontet, C., 2013. Advances in the development of nucleoside and nucleotide analogues for cancer and viral diseases. Nat. Rev. Drug Discov. 12, 447–464. doi:10.1038/nrd4010

Kawamura, K., Ikushima, K., 1993. Seasonal changes in the distribution of dicarboxylic acids in the urban atmosphere. Environ. Sci. Technol. 27, 2227–2235. doi:10.1021/es00047a033

Kundu, J., Neumann, O., Janesko, B.G., Zhang, D., Lal, S., Barhoumi, A., Scuseria, G.E., Halas, N.J., 2009. Adenine− and Adenosine Monophosphate (AMP)−Gold Binding Interactions Studied by Surface-Enhanced Raman and Infrared Spectroscopies. J Phys Chem C 113, 14390–14397. doi:10.1021/jp903126f

Kuss, J., Holzmann, J., Ludwig, R., 2009. An elemental mercury diffusion coefficient for natural waters determined by molecular dynamics simulation. Environ. Sci. Technol. 43, 3183–3186.

Langmuir, I., 1918. THE ADSORPTION OF GASES ON PLANE SURFACES OF GLASS, MICA AND PLATINUM. J. Am. Chem. Soc. 40, 1361–1403. doi:10.1021/ja02242a004

Leach, A., 2001. Molecular Modelling: Principles and Applications (2nd Edition). Prentice Hall.

Leontyev, I.V., Stuchebrukhov, A.A., 2012. Polarizable Mean-Field Model of Water for Biological Simulations with AMBER and CHARMM Force Fields. J. Chem. Theory Comput. 8, 3207–3216. doi:10.1021/ct300011h

Li, X., Yi Kuang, Shi, J., Gao, Y., Lin, H.-C., Xu, B., 2011. Multifunctional, Biocompatible Supramolecular Hydrogelators Consist Only of Nucleobase, Amino Acid, and Glycoside. J Am Chem Soc 133, 17513–17518. doi:10.1021/ja208456k

Lim, J.K., Kim, Y., Lee, S.Y., Joo, S.-W., 2008. Spectroscopic analysis of l-histidine adsorbed on gold and silver nanoparticle surfaces investigated by surface-enhanced Raman scattering. Spectrochim. Acta. A. Mol. Biomol. Spectrosc. 69, 286–289. doi:10.1016/j.saa.2007.05.007

Lu, G., Maragakis, P., Kaxiras, E., 2005. Carbon Nanotube Interaction with DNA. Nano Lett. 5, 897–900. doi:10.1021/nl050354u

Luan, B., Huynh, T., Zhou, R., 2015. Simplified TiO2 force fields for studies of its interaction with biomolecules. J. Chem. Phys. 142, 234102. doi:10.1063/1.4922618

Maleki, A., Alavi, S., Najafi, B., 2011. Molecular Dynamics Simulation Study of Adsorption and Patterning of DNA Bases on the Au(111) Surface. J Phys Chem C 115, 22484–22494. doi:10.1021/jp207533p

Marrubini, G., Mendoza, B.E.C., Massolini, G., 2010. Separation of purine and pyrimidine bases and nucleosides by hydrophilic interaction chromatography. J. Sep. Sci. 33, 803–816. doi:10.1002/jssc.200900672

Matsui, M., Akaogi, M., 1991. Molecular Dynamics Simulation of the Structural and Physical Properties of the Four Polymorphs of TiO2. Mol. Simul. 6, 239–244. doi:10.1080/08927029108022432

Mignon, P., Ugliengo, P., Sodupe, M., 2009. Theoretical Study of the Adsorption of RNA/DNA Bases on the External Surfaces of Na+-Montmorillonite. J Phys Chem C 113, 13741–13749. doi:10.1021/jp901699q

Monti, S., Walsh, T.R., 2011. Molecular Dynamics Simulations of the Adsorption and Dynamical Behavior of Single DNA Components on TiO2. J Phys Chem C 115, 24238–24246. doi:10.1021/jp207950p

Munro, L.J., Johnson, J.K., Jordan, K.D., 2001. An interatomic potential for mercury dimer. J. Chem. Phys. 114, 5545. doi:10.1063/1.1351877

Pagliai, M., Caporali, S., Muniz-Miranda, M., Pratesi, G., Schettino, V., 2012. SERS, XPS, and DFT Study of Adenine Adsorption on Silver and Gold Surfaces. J Phys Chem Lett 3, 242–245. doi:10.1021/jz201526v

Paleček, E., Bartošík, M., 2012. Electrochemistry of Nucleic Acids. Chem. Rev. 112, 3427–3481. doi:10.1021/cr200303p

Paleček, E., Černocká, H., Ostatná, V., Navrátilová, L., Brázdová, M., 2014. Electrochemical sensing of tumor suppressor protein p53–deoxyribonucleic acid complex stability at an electrified interface. Anal. Chim. Acta 828, 1–8. doi:10.1016/j.aca.2014.03.029

Paleček, E., Tkáč, J., Bartošík, M., Bertók, T., Ostatná, V., Paleček, J., 2015. Electrochemistry of Nonconjugated Proteins and Glycoproteins. Toward Sensors for Biomedicine and Glycomics. Chem. Rev. 115, 2045–2108. doi:10.1021/cr500279h

Panigrahi, S., Bhattacharya, A., Banerjee, S., Bhattacharyya, D., 2012. Interaction of Nucleobases with Wrinkled Graphene Surface: Dispersion Corrected DFT and AFM Studies. J Phys Chem C 116, 4374–4379. doi:10.1021/jp207588s

Piana, S., Bilic, A., 2006. The Nature of the Adsorption of Nucleobases on the Gold [111] Surface. J. Phys. Chem. B 110, 23467–23471. doi:10.1021/jp064438i

Plekan, O., Feyer, V., Ptasińska, S., Tsud, N., Cháb, V., Matolín, V., Prince, K.C., 2010. Photoemission Study of Thymidine Adsorbed on Au(111) and Cu(110). J. Phys. Chem. C 100812144836018. doi:10.1021/jp105341k

Plekan, O., Feyer, V., Šutara, F., Skála, T., Švec, M., Cháb, V., Matolín, V., Prince, K.C., 2007. The adsorption of adenine on mineral surfaces: Iron pyrite and silicon dioxide. Surf. Sci. 601, 1973–1980. doi:10.1016/j.susc.2007.02.032

Plekan, O., Feyer, V., Tsud, N., Vondráček, M., Cháb, V., Matolín, V., Prince, K.C., 2012. Adsorption of 5-halouracils on Au(111). Surf. Sci. 606, 435–443. doi:10.1016/j.susc.2011.11.002

Porter, J.D., Zinn, A.S., 1993. Ordering of liquid water at metal surfaces in tunnel junction devices. J. Phys. Chem. 97, 1190–1203. doi:10.1021/j100108a015

Předota, M., Bandura, A.V., Cummings, P.T., Kubicki, J.D., Wesolowski, D.J., Chialvo, A.A., Machesky, M.L., 2004a. Electric Double Layer at the Rutile (110) Surface. 1. Structure of Surfaces and Interfacial Water from Molecular Dynamics by Use of ab Initio Potentials. J Phys Chem B 108, 12049–12060. doi:10.1021/jp037197c

Předota, M., Cummings, P.T., Wesolowski, D.J., 2007. Electric Double Layer at the Rutile (110) Surface. 3. Inhomogeneous Viscosity and Diffusivity Measurement by Computer Simulations. J Phys Chem C 111, 3071–3079. doi:10.1021/jp065165u

Předota, M., Machesky, M.L., Wesolowski, D.J., Cummings, P.T., 2013. Electric Double Layer at the Rutile (110) Surface. 4. Effect of Temperature and pH on the Adsorption and Dynamics of Ions. J. Phys. Chem. C 117, 22852–22866. doi:10.1021/jp407124p

Předota, M., Zhang, Z., Fenter, P., Wesolowski, D.J., Cummings, P.T., 2004b. Electric Double Layer at the Rutile (110) Surface. 2. Adsorption of Ions from Molecular Dynamics and X-ray Experiments. J Phys Chem B 108, 12061–12072. doi:10.1021/jp037199x

Rajarajeswari, M., Iyakutti, K., Kawazoe, Y., 2011. Adsorption mechanism of single guanine and thymine on single-walled carbon nanotubes. J. Mol. Model. 17, 2773–2780. doi:10.1007/s00894-010-0946-7

Rapino, S., Zerbetto, F., 2005. Modeling the Stability and the Motion of DNA Nucleobases on the Gold Surface. Langmuir 21, 2512–2518. doi:10.1021/la047091o

Ridley, M.K., n.d. personal communication.

Rosas-García, V.M., del Carmen Sáenz-Tavera, I., Rodríguez-Herrera, V.J., Garza-Campos, B.R., 2013. Microsolvation and hydration enthalpies of $CaC_2O_4(H_2O)$ n (n=0-16) and $C_2O_4^{2-}(H_2O)$ n (n=0-14): an ab initio study. J. Mol. Model. 19, 1459–1471. doi:10.1007/s00894-012-1707-6

Sanghvi, Y.S., Guo, Z., Pfundheller, H.M., Converso, A., 2000. Improved Process for the Preparation of Nucleosidic Phosphoramidites Using a Safer and Cheaper Activator. Org Process Res Dev 4, 175–181. doi:10.1021/op990086k

Schlick, T., 2002. Molecular Modeling and Simulation: An Interdisciplinary Guide. Springer-Verlag New York, Inc., Secaucus, NJ, USA.

Sestáková, I., Mader, P., 2000. Voltammetry on mercury and carbon electrodes as a tool for studies of metallothionein interactions with metal ions. Cell. Mol. Biol. Noisy--Gd. Fr. 46, 257–267.

Sharma, S., Nath, R., Thind, S.K., 1993. Recent advances in measurement of oxalate in biological materials. Scanning Microsc. 7, 431–441.

Słojkowska, R., Jurkiewicz-Herbich, M., 1999. Adsorption of L-histidine from aqueous solutions on the mercury electrode and air/solution interface. Pol. J. Chem. 73 nr 3, 527–539.

Sowerby, S.J., Cohn, C.A., Heckl, W.M., Holm, N.G., 2001. Differential adsorption of nucleic acid bases: Relevance to the origin of life. Proc. Natl. Acad. Sci. U. S. A. 98, 820–822.

Umadevi, D., Sastry, G.N., 2011. Quantum Mechanical Study of Physisorption of Nucleobases on Carbon Materials: Graphene versus Carbon Nanotubes. J Phys Chem Lett 2, 1572–1576. doi:10.1021/jz200705w

Vainrub, A., Pettitt, B.M., 2003. Sensitive Quantitative Nucleic Acid Detection Using Oligonucleotide Microarrays. J. Am. Chem. Soc. 125, 7798–7799. doi:doi: 10.1021/ja035020q

Varghese, N., Mogera, U., Govindaraj, A., Das, A., Maiti, P.K., Sood, A.K., Rao, C.N.R., 2009. Binding of DNA Nucleobases and Nucleosides with Graphene. ChemPhysChem 10, 206–210. doi:10.1002/cphc.200800459

Vidossich, P., Lledós, A., Ujaque, G., 2016. First-Principles Molecular Dynamics Studies of Organometallic Complexes and Homogeneous Catalytic Processes. Acc. Chem. Res. doi:10.1021/acs.accounts.6b00054

Yang, B., Wang, Y., Li, G., Cun, H., Ma, Y., Du, S., Xu, M., Song, Y., Gao, H.-J., 2009. Influence of Deoxyribose Group on Self-Assembly of Thymidine on Au(111). J Phys Chem C 113, 17590–17594. doi:10.1021/jp906944c

Zhang, Z., Fenter, P., Cheng, L., Sturchio, N.C., Bedzyk, M.J., Předota, M., Bandura, A., Kubicki, J.D., Lvov, S.N., Cummings, P.T., Chialvo, A.A., Ridley, M.K., Bénézeth, P., Anovitz, L., Palmer, D.A., Machesky, M.L., Wesolowski, D.J., 2004. Ion Adsorption at the Rutile–Water Interface: Linking Molecular and Macroscopic Properties. Langmuir 20, 4954–4969. doi:10.1021/la0353834

Zhao, Payne, C.M., Cummings, P.T., 2007. Controlled Translocation of DNA Segments through Nanoelectrode Gaps from Molecular Dynamics. J Phys Chem C 112, 8–12. doi:10.1021/jp709652y

Zheng, M., Jagota, A., Semke, E.D., Diner, B.A., Mclean, R.S., Lustig, S.R., Richardson, R.E., Tassi, N.G., 2003. DNA-assisted dispersion and separation of carbon nanotubes. Nat Mater 2, 338–342. doi:10.1038/nmat877

Zhou, H., Ganesh, P., Presser, V., Wander, M.C.F., Fenter, P., Kent, P.R.C., Jiang, D., Chialvo, A.A., McDonough, J., Shuford, K.L., Gogotsi, Y., 2012. Understanding controls on interfacial wetting at epitaxial graphene: Experiment and theory. Phys. Rev. B 85, 35406. doi:10.1103/PhysRevB.85.035406

Zuman, P., Paleček, E., 2005. Polarography of Proteins: A History, in: Emil Paleček, F.S. and J.W. (Ed.), Perspectives in Bioanalysis, Electrochemistry of Nucleic Acids and Proteins – Towards Electrochemical Sensors for Genomics and Proteomics. Elsevier, pp. 755–771.

[OK1]

Kroutil O., Chval Z., Skelton A. A., Předota M.

Computer Simulations of Quartz (101)–Water Interface over a Range of pH Values

The Journal of Physical Chemistry C 119 (17), 9274-9286, (2015)

[IF(2014) = 4.772]

Participation of Ondřej Kroutil:

OK implemented new force field to Gromacs software package, performed all molecular dynamics simulations of water and ions interacting with the quartz surface and carried out all analyses. He participated in the paper writing.

THE JOURNAL OF PHYSICAL CHEMISTRY C

Article

pubs.acs.org/JPCC

Computer Simulations of Quartz (101)−Water Interface over a Range of pH Values

O. Kroutil,[†,‡] Z. Chval,[‡] A. A. Skelton,[§] and M. Předota*[,†]

[†]Faculty of Science, University of South Bohemia, Branišovská 1760, 370 05 České Budějovice, Czech Republic

[‡]Faculty of Health and Social Studies, University of South Bohemia, J. Boreckého 27, 37 011 České Budějovice, Czech Republic

[§]School of Health Sciences, University of KwaZulu-Natal, Durban 4001, South Africa

Supporting Information

ABSTRACT: The original force field for clay materials (ClayFF) developed by Cygan et al. (*J. Phys. Chem. B* **2004**, 108, 1255) is modified to describe negative charging of the (101) quartz surface above its point of zero charge (pH ≈ 2.0−4.5). The modified force field adopts the scaled natural bond orbital charges derived by the quantum mechanical calculations which are used to obtain the desired surface charge density and to determine the delocalization of the charge after deprotonation of surface silanol groups. Classical molecular dynamics simulations (CMD) of the (101) surface of α-quartz with different surface charge densities (0, −0.03, −0.06, and −0.12 C m^{-2}) are performed to evaluate the influence of the negative surface charge on interfacial water and adsorption of Na^+, Rb^+, and Sr^{2+} ions. The CMD results are compared with ab initio calculations, X-ray experiment, and the triple-layer model. The modified force field can be easily implemented in common molecular dynamics packages and used for simulations of interactions between quartz surfaces and various (bio)molecules over a wide range of pH values.

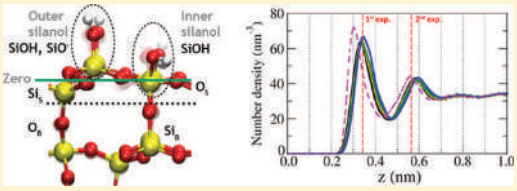

1. INTRODUCTION

Silicon dioxide with all its crystalline and amorphous modifications is one of the most abundant materials of Earth's crust. α-Quartz (α-SiO_2) is a crystalline form of silicon dioxide, stable up to 573 °C,[1] which can be found in soils, clays, and rocks, constituting about 20% of the Earth's exposed crust.[2,3] Because of the abundance of water in natural environments, the quartz−water interface is of particular interest for many geological,[4−7] biological,[8,9] and technological[10,11] applications. Interfacial water can also mediate the interaction of (bio)-molecules with surfaces,[12−14] and these interactions play a primary role in many detection techniques, such as microarray technology,[15,16] quartz microbalance,[17] chromatography,[18] and nanopore synthetic silicate membranes.[19] These interactions are also relevant for prebiotic chemistry.[20] Furthermore, it is believed that the presence of the hydroxyl groups on the quartz surface and their ability to make strong hydrogen bonds with biomolecules is the main cause of pulmonary inflammation (silicosis).[21]

Quartz surface exposed to water is covered with rather strongly acidic hydroxyl groups, silanols, that become partially deprotonated above the point of zero charge. It has been suggested that the pH_{pzc} at the point of zero charge (PZC) for quartz is approximately 2.0−4.5.[22−25] As the pH is increased, the number of deprotonated silanols and the negative charge of the surface increase and the properties of the surface and the interface are changed considerably. Accurate determination of pH_{pzc} is hampered by the fact that the curve of surface charge density versus pH is very flat in the range from 0 to 4.[25,26] Measurements of PZC of quartz are, moreover, more difficult because of its high dissolution rate in water.[27−29]

For neutral crystalline[30−32] and amorphous[31,33−37] forms of SiO_2 there are several force fields available that were parametrized against different benchmarks (quantum mechanical simulations or experimental results), and these use diverse force field terms and serve to describe different features of silicates. On the other hand, force fields that incorporate deprotonated silanol groups are rare. Hassanali et al.[38] augmented their force field for neutral amorphous silica surface[33] with new Si−O^- parameters. Concerning charges, only the partial charge on oxygen of the deprotonated silanol group was changed from −1.2 to −1.6, all other charges were not modified. Because of the rather large charge of the hydrogen, +0.6, this force field correctly accounts for the change in surface charge upon deprotonation. The simple BKS potential that uses only pair interactions to maintain the proper structure of a SiO_2 slab had to be extended with three-body "blocking potentials" to prevent unintentional, and sometimes unphysical, bond formation driven by strong Coulomb interactions within both nondissociated and dissociated models. Furthermore, Buckingham potential parameters between Na^+ and surface oxygens were added to existing Buckingham interactions among surface atoms; however, all other interactions between salt, water, and silica were described by

Received: January 5, 2015
Revised: April 4, 2015
Published: April 6, 2015

DOI: 10.1021/acs.jpcc.5b00096
J. Phys. Chem. C 2015, 119, 9274−9286

Table 1. Comparison of the ClayFF Charges and the Scaled NBO Charges[a]

method	Si_B	O_B	Si_S	O_S	Si_h	O_h	H_h	Si_{O^-}	O^-
ClayFF/0.00 = q_{i0}	2.100	−1.050	2.100	−1.050	2.100	−0.950	0.425	–	–
NBO/0.00	2.100	−1.050	2.090	−1.050	2.070	−0.900	0.420	–	–
Δ(NBO/−1.0) = Δq_i	**0.000**	**0.000**	**−0.040**	**0.019**	**−0.035**	**0.015**	**−0.003**	**−0.130**	**−0.031**[b]

[a]The relative changes of the surface atom charges upon deprotonation are shown in the third row. [b]A relative change of charge of the deprotonated oxygen O^- with respect to the O_h atom type.

a Lennard-Jones potential. Three-body blocking and SiOH bending potentials, together with a combination of two types of van der Waals potentials, limit compatibility of the Hassanali et al. force field with common biomolecular force fields. As a starting point for another force field with deprotonated silanol groups, Butenuth et al.[39] chose the force field of Cole et al.[34] Bader charge analyses on quartz periodic systems, amorphous periodic, and cluster systems have revealed that upon deprotonation, charge spreads only to the nearest neighbors; thus, only charges of deprotonated oxygen, bonded silicon, and three adjacent oxygens were changed to yield the overall change of charge of −1. On the contrary, the ESP method has provided less consistent results for given systems and has predicted a greater penetration of the charge to more distant atoms. All other parameters of the original force field were not modified. The resulting force field was evaluated against ab initio derived interaction curves for a water molecule over different surface species. This force field includes specific cutoff functions of the three-body interactions,[39,34] which might limit the implementation of this force field in standard simulation software. Emami et al.[40] developed a force field for silica that is compatible with all main simulation software packages and is parametrized for commonly used force field terms (12−6 Lennard-Jones for nonbonded interactions, harmonic terms for bonded interactions, etc.). This article follows previous work of this group on Interface force field,[41] but it does not explicitly state that it is the part of this force field, so we will call this force field "Emami et al. force field" in the following text. Emami et al. force field was validated against various structural and dynamical properties of bulk silica and the silica−water−ions interface and is projected as a universal force field for different silica modifications and different cleaved faces. Because the Emami et al. force field was released during preparation of this paper, we included results on the quartz (101) system with this force field for comparison.

Molecular dynamics simulations of ions interacting with negative amorphous silica surface are described in a few articles.[42,43] Haria and Lorenz[42] studied behavior of 0.5 M NaCl and $CaCl_2$ solutions in amorphous silica nanopores of different radius and under an applied external electric field. A surface charge density of the substrate was set to −0.144 C m^{-2}. Zhang et al.[43] focused on the validity of the Gouy−Chapman−Stern layer utilizing both molecular dynamics simulations and continuum theory. Amorphous silica with surface charge density −0.127 C m^{-2} was used as a model surface. For neutral quartz surface, Joseph and Aluru[44] provided atomistic modeling data on adsorption of K^+ and Cl^- ions in nanochannels of various diameter.

In this contribution, the negatively charged quartz surface is described by a modified ClayFF force field because it was shown in our previous work[45,46] that for neutral α-quartz surfaces ClayFF gives a closer agreement with the ab initio molecular dynamics (AIMD) results for water interactions with silanol groups than Lopes et al.[30] and CWCA[35] force fields. Simulations using ClayFF compared favorably with dielectric spectroscopy data in the work of Wander and Clark[47] who studied the structure, orientation, and dielectric properties of water on the (0001) surface of quartz. It was also shown in the work of Bourg and Steefel[48] that ClayFF force field predicts structural parameters of SiO_2 (radial distribution functions, RDFs) much more accurately than other tested two-body interaction models. Moreover, a considerable advantage of the ClayFF force field is its easy transferability into various MD software packages used for biomolecules simulations (Amber, Gromacs, LAMMPS) because only two terms for nonbonded interactions are employed, namely Coulombic and Lennard-Jones van der Waals terms, and two harmonic terms to maintain proper angles and bond lengths in silanols. In contrast, Hassanali et al. and Butenuth et al. force fields for charged silica surface include nonstandard terms.

In the present study, using both cluster and periodic plain-wave quantum mechanical calculations, partial charges of the original ClayFF force field were modified to incorporate deprotonation of the silanol groups, which changes the surface charge by exactly −1e. Only the partial charges of atoms are modified; the other interaction parameters remain identical to those of the original ClayFF. New parameters were tested on the three systems with surface charge densities −0.03, −0.06, and −0.12 C m^{-2}, corresponding to pH values of about 7.5, 9.5, and 11, respectively.[24] These results were compared with those for a neutral, fully hydroxylated surface (pH 2.0−4.5). The present work extends our previous studies involving the oxide surfaces, quartz (α-SiO_2), rutile (α-TiO_2), and cassiterite (SnO_2), which used a combined CMD/ab initio/X-ray approach[45,46,49−54] to study the metal-oxide−aqueous solution interface.

2. QUANTUM MECHANICS

2.1. Surface Optimization. The neutral quartz (101) surface was optimized with the CASTEP program package.[39] A three-dimensional (3D) supercell consisting of 1 × 1 surface unit cells was used to model the 101 surface geometry. In analogy to the earlier TiO_2 study of Bandura et al.,[55] SiO_2 surface slabs, five Si layers thick, were considered, separated by a 15 Å vacuum gap. Calculations employed the Perdew−Burke−Ernzerhof functional and ultrasoft potentials that allow small plane wave cutoff energy of −340 eV to be applied. K-points were chosen according to the default CASTEP scheme.

2.2. Charge Derivation. From the crystal structure we have generated a cluster with 392 atoms and a surface area of about 5.40 nm^2. The cluster was used for the calculation of the wave function using the B3LYP/6-31(+)G* level of theory (diffuse functions were used only for electronegative oxygen atoms). Partial atomic charges were derived using ChelpG and natural bond orbital (NBO) methods as implemented in the Gaussian 03 program. Only atoms at least three bonds from the edges of the cluster were used for the charge parametrization.

DOI: 10.1021/acs.jpcc.5b00096
J. Phys. Chem. C 2015, 119, 9274−9286

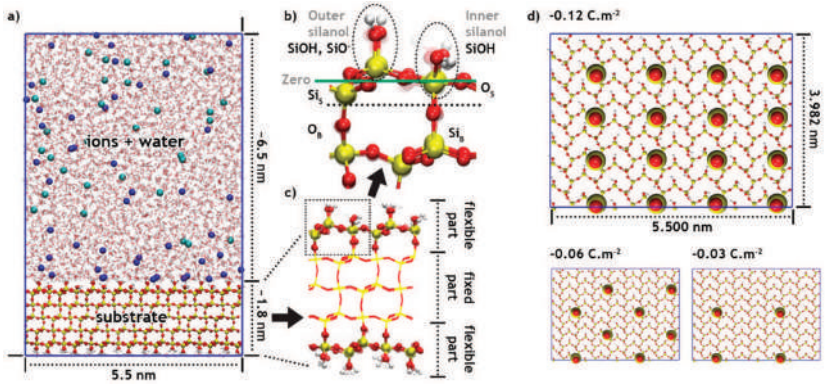

Figure 1. System setup. (a) The simulation cell with dimensions. (b) Magnified part of the surface with the outer and inner silanols labeled. The green line defines the zero plane. The black dotted line distiguishes the boundary between bulk and surface atoms in our force field (see the text) labeled as bulk silicon (Si_B), bulk oxygen (O_B), surface silicon (Si_S), surface oxygen (O_S), and silanol groups SiOH, SiO^-. (c) Flexible and fixed part of the substrate during *NVT* equilibration and production runs. (d) Positions of the deprotonated silanol groups for the three studied surface charge densities.

At first the NBO and ChelpG charges were calculated for a *neutral* cluster model of SiO_2. The NBO method offered much smaller variations, of the charges, between the atoms of the same type compared to the ChelpG method. Thus, we decided to continue with more compact NBO charges in subsequent calculations. The NBO charges calculated for the *neutral* system were systematically larger than the ClayFF ones; however, using one scaling factor of 1/1.27 for all atom types, the NBO charges were able to reproduce almost exactly the ClayFF charges. Because the differences between our scaled NBO charges and the ClayFF ones were small, we decided to use ClayFF charges without modifications. The two sets of atomic charges for the neutral surface are summarized in Table 1; atoms Si_h, O_h, and H_h denote silanol atoms and O^- deprotonated silanol oxygen. The other atom types are identified in Figure 1.

The scaled NBO charges were also calculated for the *negatively charged* surface. We started with the same cluster as for the neutral surface, but this time one hydrogen atom was removed from the OH group located roughly in the middle of the surface. On the basis of the comparison of the optimized geometries of $Si_3(OH)_9Si(OH)$ and $Si_3(OH)_9SiO^-$ complexes, the $Si-O^-$ distance was shortened to 0.1539 nm in the cluster model. This procedure should be realistic because the Si−OH distance of 0.1636 nm in the $Si_3(OH)_9SiOH$ complex is in a good agreement with the Si−OH distance of 0.1629 nm found in the neutral optimized crystal.

Differences between the scaled NBO charges of the atoms on the *neutral* and *negatively charged* surface, Δq_i, are given in the third row of Table 1. Deprotonation leads to a local deformation of the crystal structure due to two basic effects: (1) Disruption of the regular arrangement of the silanol SiOH groups on the surface enhances repulsion between the oxygens in the silanol groups and promotes reorientation of the neighboring OH groups. (2) The strong and polar $Si-O^-$ bond in the optimized $Si_3(OH)_9SiO^-$ cluster depolarizes and prolongs the neighboring Si−O bonds, compared with the neutral $Si_3(OH)_9SiOH$ structure, by about 0.06 Å. This disturbance is not localized on the deprotonated silanol group, but the more loosely bound oxygen atoms are, on the contrary, more strongly bound to the adjacent Si centers (the bonds are 0.04 Å shorter than in the neutral structure), which forms three prolonged Si−O bonds (by 0.02 Å) with more distant oxygen atoms. In this way, the disturbance of the crystal structure, caused by the deprotonation, decays with increasing distance. Our model reflects these geometrical changes showing less negative charges of the O_h and O_s atoms on the deprotonated surfaces, despite a more negatively charged surface, which weaken the $Si-O_S$ and Si−OH bonds by a decrease of their polarity (see the discussion below).

We did not consider the charge penetration into the crystal, but the excess charge was spread over the atoms on the surface only. The same simplification was used previously in the parametrization of the charged TiO_2 surface;[35] it enabled us to minimize the number of the atom types, keeping the force field as simple as possible.

We tested two possible schemes of charge assignments for negatively charged surfaces: (i)The missing charge −0.575 e was distributed proportionally to the calculated Δq_i differences. This led to a monotonous lowering of the negative charge on the O_h and O_s atoms, decreasing continuously the polarity of the $Si-O_S$ and Si−OH bonds with increasing negative surface charge. (ii) The atomic charges were modified by the unscaled Δq_i differences, and the rest of the negative charge was spread uniformly over all atoms of the surface. The final atomic charges, q_{in}, were calculated according to eq 1, where q_{i0} are atomic charges on the neutral surface, Δq_i are charge differences (Table 1, third row), N_i is a number of atoms of the given atom type i, and n is the number of deprotonated silanol groups. Because the removed hydrogen had a positive charge of 0.425 e, the charge of −0.575 e per one deprotonated silanol had to be redistributed over the remaining surface atoms.

$$q_{in} = q_{i0} + \left(\Delta q_i + \frac{n[-0.575 - \sum_i (\Delta q_i N_i)]}{\sum_i N_i} \right) \quad (1)$$

The polarity of the $Si-O_S$ and Si−OH bonds was roughly the same for all negatively charged surfaces because the higher the negative surface charge, the larger the amount of the charge redistributed uniformly. The charge redistribution resulted in a

DOI: 10.1021/acs.jpcc.5b00096
J. Phys. Chem. C 2015, 119, 9274−9286

Table 2. Partial Charges (q_{in}) on Various Atom Types for All Studied Surface Charge Densities

	atom type				SiOH			SiO$^-$	
surface charge	Si_B	O_B	Si_S	O_S	Si_h	O_h	H_h	Si_{O^-}	O^-
0.00[a]	2.10	−1.05	2.10	−1.05	2.10	−0.95	0.425	–	–
−0.03	2.10	−1.05	2.05842	−1.03258	2.06342	−0.93658	0.42042	1.96792	−0.98258
−0.06	2.10	−1.05	2.05590	−1.03510	2.06090	−0.93910	0.41790	1.96560	−0.98510
−0.12	2.10	−1.05	2.05078	−1.04022	2.05578	−0.94422	0.41278	1.96024	−0.99022

[a]Original ClayFF charges.[32]

nonmonotonous dependence of the O_h and O_s partial charges with the surface charge (Table 2). However, scheme (ii) led to a better agreement between the MM and ab initio MP2 interaction curves for the water−surface interactions (see Figure 2) compared to that resulting from scheme (i). Note that differences in atomic charges were small (up to 0.05 e) when comparing the two schemes, and a negligible influence on the results of MD simulations was observed.

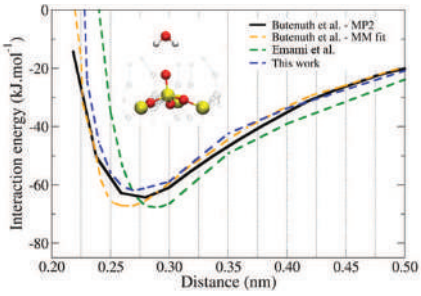

Figure 2. Interaction curves of water molecule approaching oxygen on deprotonated silanol group.

The final charges of the surface atoms for four studied surface charge densities, resulting from the coverage of the deprotonated oxygen atoms, are summarized in Table 2.

2.3. Interaction Curves. To make a first evaluation of our new derived charges for the deprotonated surface, we calculated an interaction curve for a single water molecule approaching a deprotonated silanol group using several CMD force fields. Similarly to the studies of Hassanali et al.[38] and Butenuth et al.,[39] a single water molecule was rigidly moved perpendicularly to the deprotonated silanol from height 1.0 to 0.2 nm. The configuration with H atoms of water (the dipole moment) pointing toward the oxygen on a deprotonated silanol group was chosen for this study because of its attractive nature, the available reference interaction curve for the same configuration calculated on the MP2 level in the study of Butenuth et al.[39] (Figure 2) and, finally, because of good reproducibility of this path compared to more favorable but not uniquely described configuration mentioned in Hassanali et al.[38] (Figure 3 and Path 1 therein). Results show that our modification of ClayFF force field provides a very good fit to the reference MP2 interaction curve, with the energy minimum on our interaction curve 1.5 kJ mol^{-1} above the reference curve and steeper repulsion at separations <0.25 nm. Note that our force field performs better around the minimum of potential compared to the MM fit of Butenuth et al.[39] The interaction curve computed with Emami et al. force field has a minimum shifted to a larger distance compared to the MP2 curve, otherwise its shape is similar to Butenuth's curve. Results for another path with water vertically approaching deprotonated silanol with one of its hydrogen atoms facing the deprotonated silanol are provided in the Supporting Information, Figure SI1.

3. CLASSICAL MD

3.1. Setup. The unit cell of the α-quartz (101) surface has been cleaved from a default bulk quartz crystal structure using the Inorganic builder plugin of the VMD software.[56] The simulation supercell replicated 4 × 4 × 1 from the unit cell had dimensions a = 5.500 nm, b = 3.982 nm, and c = 1.8 nm with five Si layers within the slab (Figure 1a,c). The total area of the simulation cell was 21.901 nm^2. Each unit cell had 8 silanol groups (SiOH) on one side, replicated to 128 silanol groups on one side of the simulation supercell. As shown in Figure 1d, 4, 8, and 16 silanol groups were deprotonated on one side of the surface to obtain surface charge densities of approximately −0.03, −0.06, and −0.12 C m^{-2}, respectively. The other side of the surface was left neutral. A regular distribution of the deprotonated silanol groups on the surface was chosen to minimize their mutual Coulombic repulsion.[50] It is presumed that outer silanols are more accessible for water and more acidic than inner silanols; thus, only silanol groups in the upper rows (outer silanols) were deprotonated.[45] This presumption could be verified by computing pK_a values of outer and inner silanol groups using ab initio free energy calculations in explicit solvent. The difference in ab initio energies between the nonhydrated minimized structures with deprotonated upper versus lower silanols, about 74 kJ mol^{-1}, is large enough to indicate preferential deprotonation of the upper silanol.[57]

Sodium and chloride ions were dissolved in the aqueous phase to maintain electroneutrality and to explore their interactions with the surface. Concentration of chloride ions was set to approximately 0.3 M, and the number of cations equaled the number of chloride ions plus the number of deprotonated silanols to compensate the negative surface charge. Numbers of ions are summarized in Table 3; the number of Cl$^-$ applies to all combinations with cations. The bulk concentrations of salts were about 0.40 M for NaCl and RbCl and 0.20 M for $SrCl_2$.

ClayFF force field[32] was used to describe the fully hydroxylated and partially deprotonated surfaces. This force field applies nonbonded Coulombic and Lennard-Jones terms. Only two bonding terms are included, one for the O−H bond stretching and one for the Si−O−H angle bending.

Table 3. Numbers of Ions Used in Simulations

surface charge density (C m^{-2})	Na^+	Rb^+	Sr^{2+}	Cl^-
0.00	32	32	16	32
−0.03	36	36	18	32
−0.06	40	40	20	32
−0.12	48	48	24	32

DOI: 10.1021/acs.jpcc.5b00096
J. Phys. Chem. C 2015, 119, 9274−9286

$$E_{\text{bond stretch}}(r_{ij}) = \frac{1}{2}k_b(r_{ij} - r_0)^2$$

$$E_{\text{angle bend}}(\theta_{ijk}) = \frac{1}{2}k_\theta(\theta_{ijk} - \theta_0)^2$$

The Si−O distance in the silanol group as well as any Si−O interaction is controlled only by nonbonded interactions, which properly describe both the equilibrium Si−O distance in protonated silanols[45,58] as well as the shortening of this bond in deprotonated silanols caused by a charge enhancement of the deprotonated silanol oxygen (O^-) upon its deprotonation. This trend is in a good agreement with the density functional theory (DFT) calculations described above. The same van der Waals and bonding parameters were used for both uncharged and charged systems. The force fields for neutral and charged surfaces thus differ only in partial charges of the surface atoms (Table 2). SPC/E water model[59] was employed in conjunction with new parameters for Na^+ and Cl^- ions derived to prevent a cocrystallization of ions during long nanosecond runs.[60] Standard Lorentz−Berthelot mixing rules were used for the cross interactions. All used force field parameters are summarized in Table 4.

Table 4. Summary of Nonbonded and Bonded Parameters

	Nonbonding Parameters		
	σ (nm)	ε (kJ mol^{-1})	q (e)
Si (bulk/surface)[a]	0.302 000	7.698 56 × 10^{-6}	Table 2
O (bulk/hydroxyl)[a]	0.316 557	0.650 629	Table 2
H (hydroxyl)[a]	0.000 000	0.000 000	Table 2
O (water)[b]	0.316 557	0.650 629	−0.8476
H (water)[b]	0.000 000	0.000 000	+0.4238
Na^+[c]	0.215 954	1.475 450	+1.0
Na^+[d]	0.282 415	0.393 296	+1.0
Rb^+[c]	0.309 498	1.862 310	+1.0
Sr^{2+}[e]	0.331 410	0.418 400	+2.0
Cl^-[c]	0.483 045	5.349 24 × 10^{-2}	−1.0
Cl^-[e]	0.440 104	0.418 400	−1.0
	Bonding Parameters		
	r_0 (nm)	k_b (kJ mol^{-1} nm^{-2})	
$\lvert O_h-H_h\rvert$[a]	0.1000	463 700	
	θ_0 (deg)	k_θ (kJ mol^{-1} rad^{-2})	
$\angle Si-O_h-H_h$[a]	109.47	251	

[a]ClayFF force field parameters.[32] [b]SPC/E.[59] [c]Joung and Cheatham.[60] [d]Heinz et al.[41] [e]Palmer et al.[61]

Molecular dynamics simulations were performed using the Gromacs 4.5.3 software package.[62] Systems were minimized using a steepest descent integrator. The equilibration stage consisted of a 0.1 ns simulation run in *NVT* ensemble and 1 ns simulation run in *NPT* ensemble to achieve a system pressure of 1 bar. The subsequent production (*NVT*) run lasted 50 ns. In all simulations, a 1 fs step was used with the leapfrog algorithm, the cutoff distance was set to 1.2 nm for both short-range electrostatic and van der Waals interactions, and the Lincs algorithm was used to constrain the bonds involving hydrogen atoms. Three-dimensional particle mesh Ewald summation (PME) with the correction for the 2D periodic geometry (EW3DC)[63] was used to treat the long-range electrostatics. The Nose−Hoover thermostat with a coupling time set to τ = 1.0 ps maintained the temperature of 298 K. The pressure during the *NPT* equilibration phase was controlled by semi-isotropic pressure scaling only in the *z*-direction using the Parinello−Rahman barostat set to 1 bar with a coupling time of τ = 1.0 ps.

The silanol atoms and surface Si_S and O_S atoms (see Figure 1c) were completely flexible in all simulations. In *NVT* simulations, all other atoms of the crystal were kept immobile to prevent the surface displacement in the *z*-direction, which would smear the axial profiles determined from the *z*-distribution of atoms.[45] During the *NPT* simulations, these atoms were allowed to move only in the *z*-direction to allow pressure equilibration, while preserving the correct surface geometry. The configurations were saved every 1 ps. To compare axial profiles of all simulated systems, the zero height was defined by a mean position of all surface silicon atoms of the topmost layer, i.e., silicon atoms in silanol groups and surface silicon atoms (Si_S) (Figure 1b).

Equilibration phase of the systems simulated with Emami et al. force field consisted of two phases. First, the surface alone was equilibrated in *NPT* ensemble with isotropic scaling for 0.1 ns, followed by (after adding solvent molecules and ions) a 1 ns run in *NVT* ensemble. Production runs with the Emami et al. force field were performed in *NPT* ensemble with pressure controlled by semi-isotropic pressure scaling only in the *z*-direction using the Parinello−Rahman barostat set to 1 bar with a coupling time of τ = 1.0 ps. The time step was set to 2 fs, and the overall trajectory lasted 50 ns. Because this force field includes bonding terms for all surface atoms, all atoms in the simulation box were allowed to move freely.

3.2. Interfacial Water. Behavior of water molecules was not affected by the type of dissolved cations; therefore, only results for simulations with sodium ions are discussed below.

Figure 3 shows axial number density profiles of water oxygens (O_w) and hydrogens (H_w) for all surface charge densities with positions of the peaks summarized in Table 5. For O_w, the position of the first and second peak shifts slightly farther from the surface (by less than 0.02 nm) with increasing charge density due to increasing electrostatic repulsion between negatively charged O_w and the negatively charged surface. The heights of the peaks are nearly the same for all profiles. Our

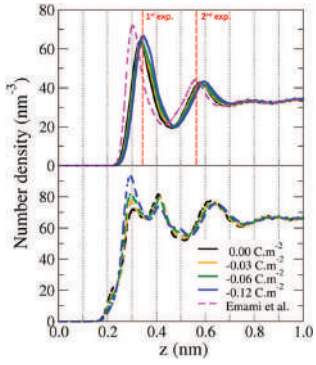

Figure 3. Axial density profiles of water oxygen O_w (solid lines) and hydrogen H_w (dashed lines) for all surface charge densities. Positions of experimentally observed density peaks for water are shown by red dashed lines. In the case of the Emami et al. force field, just results for the system with surface charge density −0.12 C m^{-2} are shown. Only results for sodium are shown.

DOI: 10.1021/acs.jpcc.5b00096
J. Phys. Chem. C 2015, 119, 9274−9286

Table 5. Positions of the Maxima (in Nanometers) of Water and Rubidium Density Peaks for the Most Charged System (-0.12 C m^{-2})

	exptl.[a]	this work	Emami et al.[b]	DFT neutral[c]	DFT charged[d]
water first peak	0.34 ± 0.01	0.341	0.305	0.365	
water second peak	0.56 ± 0.08	0.601	0.565	0.652	
rubidium first peak	0.33 ± 0.01	0.381	0.335	0.398	∼0.39 or 0.494
rubidium second peak	0.79 ± 0.2	0.591	0.555	0.768	0.604

[a]Experimental work by Bellucci et al.[64] [b]Our simulations with Emami et al. force field.[40] [c]DFT data by Bellucci et. al for neutral surface.[64] [d]DFT data by Bellucci et. al for charged surface.[64]

simulations with the Emami et al. force field show both peaks consistently shifted by 0.035 nm toward the surface compared to simulations with our modification of ClayFF force field, but the overall shape of O_w axial density profile is similar for both force fields.

New experimental data of Bellucci et al.[64] allow us to compare positions of the water density peaks from simulations and experiment. In their work, they used as the zero height reference the positions of the *unrelaxed* oxygens in the silanols; therefore, in Table 5 we list their data increased by 0.17 nm, i.e., the vertical separation between silicon atoms (our definition of zero height) and oxygen atoms in the topmost layer.

For water (with 0.01 M RbCl dissolved), the best fit model to X-ray reflectivity measurements had two adsorbed water layers with first peak positioned at 0.34 nm and second peak at 0.56 nm above last layer of silicon atoms. Our modification of ClayFF force field gives perfect agreement in position of the first peak (Table 5), while Emami et al. force field has first peak shifted by 0.035 nm closer to surface. In the case of the second peak, the situation is reversed. Emami et al. force field perfectly matches the experimental position of the second peak while our force field gives position shifted by 0.04 nm out of the surface. Both force fields thus confirm occurrence of two ordered layers of water near the quartz surface that was not observed in the study of Schlegel et al.[65]

For H_w, the situation is different. With increasing charge density, the position of the first peak around 0.28 nm shifts toward slightly lower z values while the position of the second peak remains around 0.38 nm. The heights of the peaks change considerably. While the 0.00 profile has a higher density of hydrogen atoms in the second peak, with increasing charge density the height of the first peak grows at the expense of the second peak because of attraction of H_w toward the negative surface and particularly the deprotonated silanols. Another remarkable change is a disappearance of the shoulder visible around 0.2 nm for the neutral surface. This shoulder can be attributed to hydrogen bonds between H_w and the inner silanol oxygen atoms O_h^{I4S}. The decrease in the number of these H-bonds on the negatively charged surfaces can be explained by an increased preference of water molecules toward deprotonated outer silanol.

To visualize the binding positions of the water molecules in the first layer (z < 0.45 nm), lateral density profiles are reported in Figure 4. For the neutral surface (Figure 4a), one can recognize a periodic pattern with two distinct maxima. The first one is located near each outer silanol group with H_w hydrogen bonded to silanol oxygen O_h and O_w facing the neighboring silanol group. The second maximum lies near the inner silanol groups with a bonding pattern similar to that in the first case. With increasing charge density the situation quantitatively and even qualitatively changes. Each deprotonated silanol group strongly attracts water molecules, and this is clearly reflected in lateral density patterns. O_w and H_w lateral densities move from neutral silanol groups toward deprotonated ones, creating four

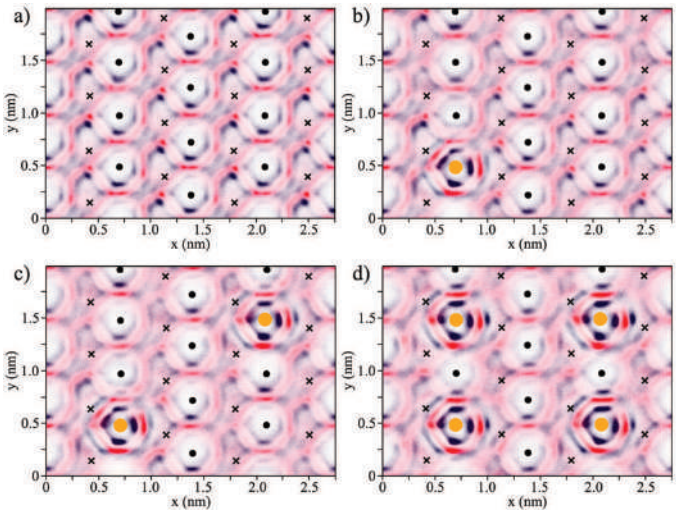

Figure 4. Lateral density of water computed for the distances 0.00−0.45 nm above the surface, corresponding to the first layer. Density of hydrogens (H_w) is in blue and density of oxygens (O_w) in red. Positions of outer silanols are highlighted by black dots, and positions of inner silanols are highlighted by black crosses; deprotonated silanols are highlighted by orange dots. Graphs are for surface charge densities (a) 0.00 C m^{-2}, (b) −0.03 C m^{-2}, (c) −0.06 C m^{-2}, and (d) −0.12 C m^{-2}. Only results with sodium are shown.

DOI: 10.1021/acs.jpcc.5b00096
J. Phys. Chem. C 2015, 119, 9274−9286

maxima (Figure 4b,c,d). At the same time, water lateral density around neutral silanol groups decreases, mainly around the inner ones.

Radial distribution functions between various atoms complement the bonding pattern of water. Figure 5a shows RDFs of

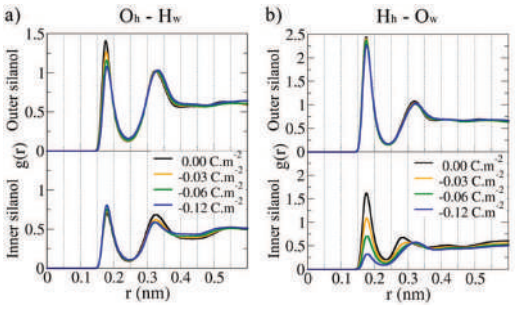

Figure 5. Radial distribution functions (a) of the silanol oxygen (O_h) and water hydrogen (H_w) and (b) the silanol hydrogen (H_h) and water oxygen (O_w). Upper graphs are for the protonated outer silanol groups, and the lower graphs are for the inner silanol groups.

the O_h and H_w, and it is clear that except for the height of the first peak of the outer silanol, curves do not change with increasing charge density. The heights of the first peaks for protonated outer silanols decrease from 0.00 to −0.12 systems; the running coordination number (RCN) decreases from 1.23 to 1.13, respectively (Figure SI2a in Supporting Information). This can be explained by greater hydration of deprotonated silanols that attract water molecules from neighboring protonated outer silanol groups. This is probably also true for the inner silanols, but here RCN slightly increases from 0.73 to 0.84 for 0.00 and −0.12 systems (Figure SI2a in Supporting Information). This is caused by greater solvent accessibility of O_h atoms of inner silanol groups on the charged surface because of a change of the O_h−H_h bond orientation. This can be documented by a dramatic decrease of H_h−O_w RDFs with increasing charge density (the lower part of Figure 5b), which means that hydrogen bonding between inner silanol H_h and water oxygen O_w almost disappears for the −0.12 surface. This can be also illustrated on RCN that changes from 0.73 to 0.18 for 0.00 and −0.12 systems, respectively (Figure SI2b in Supporting Information). The analysis of average H_h positions explains this behavior (Figure SI3a in Supporting Information). For the neutral system, hydrogen atoms of inner silanols H_h (on average) face the solution and are fully accessible for hydrogen bonding with water oxygen atoms, O_w. However, with increasing negative charge density these hydrogens are more strongly attracted by the negative charge of the surface. As a result, they are oriented more toward the surface (Figure SI3b in Supporting Information) and become less accessible for the water molecules. Thus, the number of H_h−O_w hydrogen bonds decreases with increasing charge density, while the number of O_h−H_w bonds increases very slightly.

The number of water molecules coordinated to deprotonated silanol changes from about 3 to 3.5 when increasing charge density from −0.03 to −0.12 C m^{-2} (Figure SI4 in Supporting Information), while the number of water molecules coordinated to protonated silanol oxygen is about 1 for all surfaces (Figure SI2 in Supporting Information). Information on the orientation of water molecules at the interface for quartz, including comparison with rutile, is given in Figure SI5 in Supporting Information.

3.3. Ions. The axial density profiles of sodium, rubidium, and strontium ions are shown in Figure 6, with shading

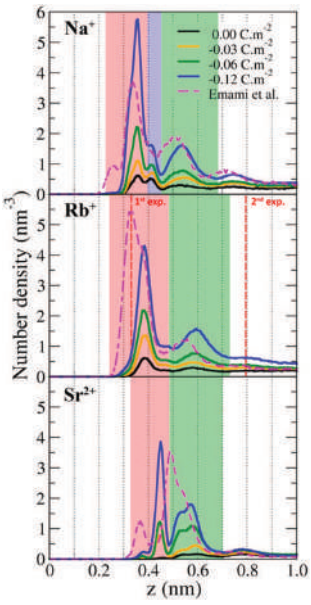

Figure 6. Axial density profiles of sodium (top panel), rubidium (middle panel), and strontium (bottom panel) ions for all surface charge densities. Our results for simulations with the Emami et al. force field[40] are for surface charge density −0.12 C m^{-2}. Positions of experimentally observed density peaks for rubidium are shown by vertical red dashed lines.

identifying distinct adsorption types. For all types of cations one can see an increasing number of cations close to the surface with increasing negative surface charge density. The amount of adsorbed ions is nearly proportional to the surface charge, though for monovalent ions (Na^+, Rb^+) it is nonzero for the neutral surface (see also Figure 8). In other aspects the density profiles differ from each other. In the case of the sodium cation, there are four distinguishable peaks up to a distance of 1 nm; in the −0.12 system, the second peak overlaps with the first one and makes a shoulder. Similarly to ion adsorption on the hydroxylated rutile surface,[51,66] positions of the adsorption peaks do not change with increasing charge density. Haria and Lorenz,[42] who studied amorphous silica nanopores with a surface charge density of −0.144 C m^{-2} and applied external electric field, E = 0.5 V nm^{-1}, found only one broad peak for Na^+ ions with a maximum at 0.40 nm. This broadening of the Na^+ peak may be caused by an irregular distribution of deprotonated sites on the amorphous silica surface. The shift of their maximum to a higher value compared to our maximum (0.35 nm) can be caused by a different definition of the zero plane; ref 42 does not provide this definition.

To distinguish between inner-sphere and outer-sphere types of adsorption and to evaluate the number of contacts with silanol groups in the case of inner-sphere adsorption

DOI: 10.1021/acs.jpcc.5b00096
J. Phys. Chem. C 2015, 119, 9274−9286

Table 6. Denticities of Different Ions Interacting with Most Charged (-0.12 C m^{-2}) Surface[a]

		no. of contacts with *outer* silanols								
		Na			Rb			Sr		
	no. of contacts with *inner* silanols	0	1	2	0	1	2	0	1	2
first inner-sphere layer	0	0.11	6.29	0.01	0.15	5.57	2.46	2.52	**91.62**	0.00
	1	**59.32**	**34.19**	0.09	**10.60**	**58.16**	**21.14**	2.21	3.64	0.01
second inner-sphere layer	0	8.62	**82.16**	0.00						
	1	9.21	0.02	0.00						
outer-sphere layer	0	**98.49**	1.51	0.00	**81.92**	**16.74**	0.04	**99.59**	0.40	0.00
	1	0.00	0.00	0.00	1.03	0.27	0.00	0.00	0.00	0.00

[a]Dominant combinations are given in bold.

(denticity), Table 6 lists, within each peak, the percentage of ions having a given number of contacts with outer silanols (columns) and inner silanols (rows). Cut-off values necessary to distinguish between outer- and inner-sphere type of adsorption were taken from radial distribution functions of the ion and silanol oxygens. These values are 0.31, 0.37, and 0.36 nm for sodium, rubidium and strontium cations, respectively. For sodium in the first peak ~60% of cations are monodentate inner-sphere complexes adsorbed to inner silanols and ~34% of the cations create bidentate inner-sphere complexes with one inner silanol group and one outer silanol group. More than 80% of cations in the second peak form monodentate inner-sphere complexes with outer silanols, and almost all cations in the third peak are outer-sphere complexes.

The density profile of rubidium shows only three peaks with the first two much more pronounced than the last peak. Compared to sodium cations, the inner-sphere peak is slightly (0.03 nm) shifted farther from the surface as well as the outer-sphere peak (0.06 nm). This is caused by a larger ionic radius of the rubidium cation and different nature of its solvent shell, which results in the different binding behavior. This is supported by analysis of denticities in different density peaks. Unlike the sodium cations, the majority (~58%) of rubidium cations in the first peak create bidentate inner-sphere complexes with one outer silanol and one inner silanol and ~21% create even tridentate configurations. Only 10% of cations in the first peak makes monodentate complexes with inner silanols. The second peak represents mainly outer-sphere complexes (~82%) with the minority (~17%) of monodentate inner-sphere complexes with outer silanols.

The rubidium density profile can be compared directly to experimental and DFT data of Bellucci et al.[64] The best fit to resonant anomalous X-ray reflectivity (RARX) measurements in experimental work predicts a two-layer model of rubidium adsorption with discrete inner-sphere complexes in the first and outer-sphere complexes in the second peak. The adsorption height for the first peak from experiment is 0.33 nm above our reference zero. With our modification of ClayFF force field, the first peak is shifted by 0.051 nm away from the surface (0.381 nm), while the Emami et al. force field perfectly matches (0.335 nm) the experimental value (Table 5). DFT calculations in Bellucci et al.[64] predict a value of 0.398 nm for the neutral surface and two values for the charged surface: ~0.39 and 0.494 nm. Although the latter value is much farther from the surface compared to experiment and our simulation, Belluci et al. favored this value because the structure with this distance had the lowest energy compared to the configurations with Rb^+ positions ~0.39 nm above our reference zero. Conversely, one has to keep in mind that DFT calculations deal with only a few configurations, providing poor statistics compared to the thousands of configurations in MD simulations, and completely omit entropy factors. Because the position (~0.39 nm) and denticities (bidentate inner-sphere) of the less favored configurations, from DFT calculations for charged surface, nicely fit our MD simulation values, we suppose that entropy factors and statistics play a major role in this case, and we suggest that the DFT values discussed but refused by Bellucci et al. could be the correct values.

Concerning position of the second adsorption peak, both CMD models predict it ~0.2 nm closer to the surface than experimental and DFT calculations data on the *neutral* surface. However, the experimental data show larger uncertainty for the position of the second peak (±0.1 nm), and the value from DFT calculations is taken from the neutral surface model. The DFT calculations of Belluci et al. predict the position of the second Rb^+ peak for the *charged* surface 0.6 nm above the surface, in good agreement with our MD simulations (0.59 nm); Bellucci et al.[64] treated this value as a discrepancy with their RAXR data 0.79 nm.

To further analyze this discrepancy, we plot together in Figure SI6 in Supporting Information the number density profiles of rubidium from our simulations with ClayFF force field, Emami et al. force field, and electron density profile derived from analysis of the RAXR data.[64] One can notice that the first peak of the experimental density profile (when scaled to approximate height of the first peak from simulations) spans the first and second peaks derived from simulations, while the second experimental peak occurs in a region where both simulations have a small third peak. This can indicate that, because of surface roughness, small Si vacancy concentration, and resolution of RAXR (~0.1 nm), the first experimental peak might include the first two peaks from MD and DFT simulations.

Because the strontium cation carries +2 charge, the molecules (ligands) in its first solvation shell are much more tightly bound and the adsorption pattern is different compared to monovalent cations. The first peak is located 0.43 nm above the surface, i.e., 0.1 nm farther than for sodium. Table 6 shows that the adsorption behavior is much more specific compared to that of monovalent ions. More than 90% of Sr^{2+} in the first peak represents monodentate inner-sphere complexes bound to outer silanols, and almost all cations in the second peak are outer-sphere complexes. Strong solvation of Sr^{2+} by water molecules prevents inner-sphere adsorption on the neutral surface; significant adsorption begins for -0.06 C m^{-2}, and a further increase of surface charge density to -0.12 C m^{-2} causes a more than proportional increase of inner-sphere adsorption.

DOI: 10.1021/acs.jpcc.5b00096
J. Phys. Chem. C 2015, 119, 9274−9286

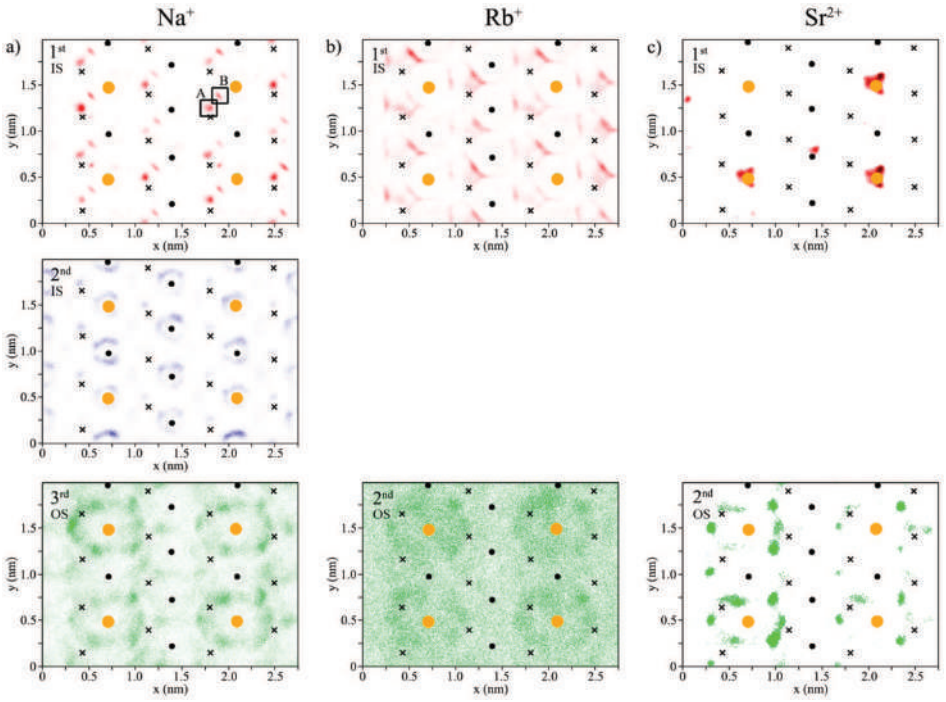

Figure 7. Lateral density profiles of (a) sodium, (b) rubidium, and (c) strontium ions for the surface charge density −0.12 C m^{-2}. "1st IS" corresponds to the first inner-sphere peak in Figure 6. "2nd IS" corresponds to the second inner-sphere axial peak. "OS" corresponds to the outer-sphere peak. Positions of the outer protonated silanols, outer deprotonated silanols, and inner silanols are represented by black dots, bigger orange dots, and crosses, respectively.

The lateral positions of the adsorption sites remain the same for all ions and all charge densities studied. In Figure 7 the lateral density profiles of the −0.12 C m^{-2} systems are presented because these are statistically the most accurate ones. The results for the other systems are given in Figure SI7 in Supporting Information. Lateral density profiles of sodium were analyzed separately for the first three adsorption peaks, i.e., for distances 0−0.362, 0.362−0.430, and 0.430−0.642 nm. Analysis of the fourth adsorption peak is not shown because its intensity is too low compared to previous ones and we have not found any recognizable pattern in its lateral profile. Within the first peak, two distinct adsorption sites denoted as A and B can be found (Figure 7a). Site A represents monodentate inner-sphere adsorption of sodium ion directly above the inner silanol oxygen with one water molecule bridging the sodium ion and the oxygen atom of the outer silanol group. Site B is a bidentate inner-sphere adsorption site with sodium ions equally distributed between inner and outer silanol oxygens. These two binding motifs occur in the vicinity of all inner silanol groups, but adsorption is increased in the neighborhood of the deprotonated outer silanol groups due to higher electrostatic attraction.

The lateral density profile for the second adsorption peak (Figure 7a) reveals one highly populated adsorption site. It represents an inner-sphere monodentate adsorption site of the sodium ion coordinated to outer silanol oxygen. The position of the sodium ion is a bit offset relative to the position of the silanol group because of the presence of an additional interaction with neighboring outer silanol groups mediated by a water molecule. The surprisingly stronger binding preference of Na^+ for protonated silanols over deprotonated ones can be attributed to higher (and stronger) solvation of deprotonated hydroxyls than protonated ones (see Figures 4 and 5 and Figure SI4 in Supporting Information); this solvation hinders the binding of incoming ions. Within the third adsorption peak there are sites with increased density of outer-sphere adsorbed ions around deprotonated silanols (Figure 7a). The intensity of this peak decreases dramatically with decreasing charge density.

The lateral distribution of Rb^+ (Figure 7b) shows a more continuous distribution of adsorption sites, including a transition between bidentate and tridentate sites. The distribution in the second layer is already flat, with a slightly increased adsorption of outer-sphere cations around deprotonated silanols. The lateral distribution of Sr^{2+} (Figure 7c) confirms strong preference for monodentate sites atop outer silanols, particularly the deprotonated ones. In the second layer formed by outer-sphere Sr^{2+} adsorption, preference of sites around the deprotonated silanols is still evident.

The radial distribution function of the sodium ion around the oxygen of deprotonated silanol (not shown) has an inner-sphere adsorption peak around 0.225 nm and outer-sphere adsorption overlapping peaks around 0.39 and 0.45 nm. Positions of these peaks do not depend on the surface charge density. The position of the inner-sphere peak around 0.225

DOI: 10.1021/acs.jpcc.5b00096
J. Phys. Chem. C 2015, 119, 9274−9286

nm is in very good agreement with AIMD data of Hassanali et al.[38] who report the value 0.23 nm; in fact, it is closer than the position around 0.245 nm from their empirical force field.

To quantify the adsorption, we plot in Figure 8 the dependence of the amount of adsorbed ions (considering

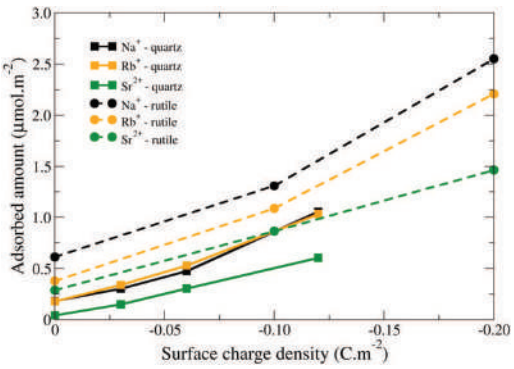

Figure 8. Dependence of the adsorbed amount of sodium (black), rubidium (orange), and strontium (green) ions on surface charge density. Data for rutile (dashed lines) surface are taken from Table 8 of Předota et al.[66]

inner-sphere adsorption and first peak of outer-sphere adsorption) on surface charge density and compare it to the same data on hydroxylated (110) rutile surface.[66] Adsorption on rutile is stronger compared to quartz for all ions. Differences are bigger for neutral surfaces where the rutile surface adsorbs 3.3, 2.1, and 6.6 times more sodium, rubidium, and strontium ions, respectively, than the quartz surface. With increasing surface charge density these ratios decrease. Rutile has higher selectivity to different ion species, with Na^+ adsorption being larger than that of Rb^+ and Sr^{2+} on all surfaces. On quartz, the adsorption of sodium and rubidium is practically the same, but the adsorption of Sr^{2+} is much lower, particularly on the neutral surface. The experimental value of adsorbed rubidium in the first two adsorption layers is 0.23 ± 0.03 Rb/A_{UC} (where A_{UC} = 0.338 nm^2 is the area of a unit cell along the (101) plane).[64] Our simulations predict a value of 0.20 Rb/A_{UC} when integrating over the first two well-pronounced peaks (up to 0.73 nm from the surface, see Figure 6) or 0.24 Rb/A_{UC} if even the third peak (up to 0.93 nm from the surface) is taken into account.

Sorption activities and properties of various electrolyte/solid interfaces are often modeled by different surface complexation models such as constant capacitance,[67] Smit,[68] triple-layer[69] models, and others. For example, the popular thermodynamic model of Sverjensky extends a triple-layer model and relates adsorption of various electrolyte ions on the mineral surfaces to the inverse dielectric constant of the mineral.[70] It was derived[71] that quartz (together with silica) belongs to a family of minerals with low dielectric constant and ions adsorb on these types of surfaces as outer-sphere complexes with intact solvation shell. Specifically for quartz, it was suggested[71] that sodium ions should be 0.59 nm and rubidium 0.56 nm above the reference plane and sodium and rubidium ions should be 0.67 and 0.64 nm above the reference plane[69] (Table 7). Position of the reference plane is not fully explained to the molecular level, but by comparison with rutile surface we infer that it can be set to

Table 7. Heights (in Nanometers) of Adsorbed Ions above Surface from Our Simulations and the Work of Sverjensky[69,71]

	this work (our reference zero height)	this work (Sverjensky's reference zero)	Sverjensky[71]	Sverjensky[69]
Na^+	0.46	0.41	0.59	0.67
Rb^+	0.50	0.44	0.56	0.64
Sr^{2+}	0.48	0.42	0.72	0.80

the average position of all silanol oxygens together with uppermost layer of the surface oxygens, i.e., at a height −0.06 relative to our zero plane given by the average position of silanol oxygens. Table 7 compares the weighted averages of the heights of adsorbed ions in the inner-sphere sites and the first outer-sphere peak from our simulations with the adsorption heights predicted by Sverjensky's model with respect to the reference plane. It is clear that in CMD we observe ions adsorbing much closer to the surface than predicted by Sverjensky's model. Moreover, several experimental[72,73] and theoretical[58,74] works including the recent work of Bellucci et al.[64] predict occurrence of inner-sphere complexes of ions on quartz and amorphous silica.

4. CONCLUSIONS

We have generalized the ClayFF force field for the simulation of negatively charged quartz (101) surfaces obtained from neutral surfaces by the partial deprotonation of outer silanol groups. We have preserved the simplicity of the ClayFF force field, namely its simple form of Lennard-Jones nonbonding terms and standard harmonic bonding terms (silanol O−H bend−stretching and Si−O−H angle bending). Moreover, even the parameters in these terms were kept equal to their values in neutral surfaces. The modification consists of sets of ab initio derived charges of surface atoms, dictating the resulting surface charge density. The atomic charges of the ClayFF, including our modified surface charges, are close to those of Butenuth,[39] which provided good agreement with ab initio potential profiles. Our modification of ClayFF force field allows its easy incorporation into simulation software and carrying out simulation of negatively charged surfaces, which are characteristic for ambient pH, as opposed to neutral surfaces.

We have found that atoms of both outer and inner silanol groups play a key role in the adsorption of water molecules and ions. The simulation results are in very good agreement with ab initio results and recent experimental data for water and rubidium ions from X-ray diffraction. Large discrepancies are reported only for the second peak of Rb^+ adsorption, which is, however, determined experimentally with a significant uncertainty. Comparison of our simulations with ab initio calculations and experimental data suggests that the experimental first peak might cover our inner-sphere and outer-sphere peaks, while the second experimental peak corresponds to the farther outer-sphere peak.

In addition to our simulations of charged quartz (101) surfaces using generalized ClayFF, we have also carried out simulations of these surfaces with recent Emami et al. force field, which is also a simple force field applicable for simulations of quartz surfaces in common simulation software. The Emami et al. force field gives slightly worse agreement with experimental data for water but excellent agreement with the position of the first peak of Rb^+ from X-ray.

DOI: 10.1021/acs.jpcc.5b00096
J. Phys. Chem. C 2015, 119, 9274−9286

Our results present the first and thorough analysis of interactions of water and Na^+, Rb^+, and Sr^{2+} ions with negatively charged quartz (101) surfaces. The detailed analysis of ion adsorption including denticities provides data for surface complexation modeling of this surface. The simulation data predict adsorption of smaller Na^+ at shorter distance from the surface than larger Rb^+ ion, both adsorbing as inner-sphere and outer-sphere complexes, which is in contrast to the triple-model of Sverjensky, which assumes adsorption of hydrated outer-sphere complexes on surfaces of low dielectric constant materials and Na^+ adsorbing at larger distances than Rb^+. CMD simulations indicate that the orientation of water at the interfaces with quartz and rutile is affected by the interactions with surface groups to a comparable extent, while Sverjensky expects water to be less oriented at the quartz interface because of higher interfacial dielectric constant.

Study of interactions of organic molecules and biomolecules with quartz surfaces over a range of pH values is already in progress.

■ ASSOCIATED CONTENT

Supporting Information

Interaction energies for alternative path, interfacial dipolar orientation, and additional structural analyses. This material is available free of charge via the Internet at http://pubs.acs.org.

■ AUTHOR INFORMATION

Corresponding Author

*Phone: +420 38777 6258, E-mail: predota@prf.jcu.cz

Notes

The authors declare no competing financial interest.

■ ACKNOWLEDGMENTS

O.K. and M.P. were supported by the Czech Science Foundation Project 13-08651S. Z.Ch. was supported by the Czech Science Foundation Project P208/12/0622. Computational resources were provided by the MetaCentrum under the program LM2010005 and the CERIT-SC under the program Centre CERIT Scientific Cloud, part of the Operational Program Research and Development for Innovations, Reg. CZ.1.05/3.2.00/08.0144. We thank J. D. Kubicki for providing ab initio interaction energies of deprotonated silanol groups and F. Bellucci for providing his data prior to publication.[64]

■ REFERENCES

(1) Legrand, A. P. *The Surface Properties of Silicas*; Wiley: Chichester, 1999.

(2) Zhuravlev, L. T. The Surface Chemistry of Amorphous Silica. Zhuravlev Model. *Colloids Surf., A* **2000**, *173* (1−3), 1−38.

(3) White, A. F.; Blum, A. E.; Schulz, M. S.; Vivit, D. V.; Stonestrom, D. A.; Larsen, M.; Murphy, S. F.; Eberl, D. Chemical Weathering in a Tropical Watershed, Luquillo Mountains, Puerto Rico: I. Long-Term Versus Short-Term Weathering Fluxes. *Geochim. Cosmochim. Acta* **1998**, *62* (2), 209−226.

(4) Yang, X.-S. A Unified Approach to Mechanical Compaction, Pressure Solution, Mineral Reactions and the Temperature Distribution in Hydrocarbon Basins. *Tectonophysics* **2001**, *330* (1−2), 141−151.

(5) Newton, R. C.; Manning, C. E. Thermodynamics of SiO_2−H_2O Fluid near the Upper Critical End Point from Quartz Solubility Measurements at 10 Kbar. *Earth Planet. Sci. Lett.* **2008**, *274* (1−2), 241−249.

(6) Koretsky, C. M.; Sverjensky, D. A.; Salisbury, J. W.; D'Aria, D. M. Detection of Surface Hydroxyl Species on Quartz, Γ-Alumina, and Feldspars Using Diffuse Reflectance Infrared Spectroscopy. *Geochim. Cosmochim. Acta* **1997**, *61* (11), 2193−2210.

(7) Schulz, M. S.; White, A. F. Chemical Weathering in a Tropical Watershed, Luquillo Mountains, Puerto Rico III: Quartz Dissolution Rates. *Geochim. Cosmochim. Acta* **1999**, *63* (3−4), 337−350.

(8) Tamerler, C.; Kacar, T.; Sahin, D.; Fong, H.; Sarikaya, M. Genetically Engineered Polypeptides for Inorganics: A Utility in Biological Materials Science and Engineering. *Mater. Sci. Eng., C* **2007**, *27* (3), 558−564.

(9) Sano, K.-I.; Sasaki, H.; Shiba, K. Specificity and Biomineralization Activities of Ti-Binding Peptide-1 (TBP-1). *Langmuir* **2005**, *21* (7), 3090−3095.

(10) Papakonstantinou, P.; Vainos, N. .; Fotakis, C. Microfabrication by UV Femtosecond Laser Ablation of Pt, Cr and Indium Oxide Thin Films. *Appl. Surf. Sci.* **1999**, *151* (3−4), 159−170.

(11) Pinto, E. M.; Gouveia-Caridade, C.; Soares, D. M.; Brett, C. M. A. Electrochemical and Surface Characterisation of Carbon-Film-Coated Piezoelectric Quartz Crystals. *Appl. Surf. Sci.* **2009**, *255* (18), 8084−8090.

(12) Skelton, A. A.; Liang, T.; Walsh, T. R. Interplay of Sequence, Conformation, and Binding at the Peptide−Titania Interface as Mediated by Water. *ACS Appl. Mater. Interfaces* **2009**, *1* (7), 1482−1491.

(13) Wu, C.; Skelton, A. A.; Chen, M.; Vlcek, L.; Cummings, P. T. Modeling the Interaction between Integrin-Binding Peptide (RGD) and Rutile Surface: The Effect of Cation Mediation on Asp Adsorption. *Langmuir* **2012**, *28* (5), 2799−2811.

(14) Wu, C.; Skelton, A. A.; Chen, M.; Vlcek, L.; Cummings, P. T. Modeling the Interaction between Integrin-Binding Peptide (RGD) and Rutile Surface: The Effect of Na+ on Peptide Adsorption. *J. Phys. Chem. C* **2011**, *115* (45), 22375−22386.

(15) Sassolas, A.; Leca-Bouvier, B. D.; Blum, L. J. DNA Biosensors and Microarrays. *Chem. Rev. (Washington, DC, U.S.)* **2008**, *108* (1), 109−139.

(16) Sobek, J.; Bartscherer, K.; Jacob, A.; Hoheisel, J. D.; Angenendt, P. Microarray Technology as a Universal Tool for High-Throughput Analysis of Biological Systems. *Comb. Chem. High Throughput Screening* **2006**, *9* (5), 365−380.

(17) Buttry, D. A.; Ward, M. D. Measurement of Interfacial Processes at Electrode Surfaces with the Electrochemical Quartz Crystal Microbalance. *Chem. Rev. (Washington, DC, U.S.)* **1992**, *92* (6), 1355−1379.

(18) Nawrocki, J. The Silanol Group and Its Role in Liquid Chromatography. *J. Chromatogr., A* **1997**, *779* (1−2), 29−71.

(19) Ho, C.; Qiao, R.; Heng, J. B.; Chatterjee, A.; Timp, R. J.; Aluru, N. R.; Timp, G. Electrolytic Transport through a Synthetic Nanometer-Diameter Pore. *Proc. Natl. Acad. Sci. U.S.A.* **2005**, *102* (30), 10445−10450.

(20) Plekan, O.; Feyer, V.; Šutara, F.; Skála, T.; Švec, M.; Cháb, V.; Matolín, V.; Prince, K. C. The Adsorption of Adenine on Mineral Surfaces: Iron Pyrite and Silicon Dioxide. *Surf. Sci.* **2007**, *601* (9), 1973−1980.

(21) Murashov, V. V.; Leszczynski, J. Adsorption of the Phosphate Groups on Silica Hydroxyls: An Ab Initio Study. *J. Phys. Chem. A* **1999**, *103* (9), 1228−1238.

(22) Iler, R. K. *The Chemistry of Silica: Solubility, Polymerization, Colloid and Surface Properties, and Biochemistry*; Wiley: New York, 1979.

(23) Fuerstenau, D. W.; Pradip. Zeta Potentials in the Flotation of Oxide and Silicate Minerals. *Adv. Colloid Interface Sci.* **2005**, *114−115* (0), 9−26.

(24) Ridley, M. K. Personal communication.

(25) Lyklema, J.; Fokkink, L. G. J.; de Keizer, A. Interfacial Electrochemistry of Oxides: Recognition of Common Principles. In *Interfaces in Condensed Systems*; Findenegg, G. H., Ed.; Progress in Colloid & Polymer Science; Steinkopff: Damstadt, Germany, **1990**; Vol. *83*, pp 46−51.

DOI: 10.1021/acs.jpcc.5b00096
J. Phys. Chem. C 2015, 119, 9274−9286

(26) Sahai, N. Is Silica Really an Anomalous Oxide? Surface Acidity and Aqueous Hydrolysis Revisited. *Environ. Sci. Technol.* **2002**, *36* (3), 445−452.
(27) Bickmore, B. R.; Wheeler, J. C.; Bates, B.; Nagy, K. L.; Eggett, D. L. Reaction Pathways for Quartz Dissolution Determined by Statistical and Graphical Analysis of Macroscopic Experimental Data. *Geochim. Cosmochim. Acta* **2008**, *72* (18), 4521−4536.
(28) Dove, P. M.; Elston, S. F. Dissolution Kinetics of Quartz in Sodium Chloride Solutions: Analysis of Existing Data and a Rate Model for 25°C. *Geochim. Cosmochim. Acta* **1992**, *56* (12), 4147−4156.
(29) Dove, P. M. The Dissolution Kinetics of Quartz in Aqueous Mixed Cation Solutions. *Geochim. Cosmochim. Acta* **1999**, *63* (22), 3715−3727.
(30) Lopes, P. E. M.; Murashov, V.; Tazi, M.; Demchuk, E.; MacKerell, A. D. Development of an Empirical Force Field for Silica. Application to the Quartz−Water Interface. *J. Phys. Chem. B* **2006**, *110* (6), 2782−2792.
(31) Shan, T.-R.; Devine, B. D.; Hawkins, J. M.; Asthagiri, A.; Phillpot, S. R.; Sinnott, S. B. Second-Generation Charge-Optimized Many-Body Potential for Si/SiO_2 and Amorphous Silica. *Phys. Rev. B: Condens. Matter Mater. Phys.* **2010**, *82* (23), 235302.
(32) Cygan, R. T.; Liang, J.-J.; Kalinichev, A. G. Molecular Models of Hydroxide, Oxyhydroxide, and Clay Phases and the Development of a General Force Field. *J. Phys. Chem. B* **2004**, *108* (4), 1255−1266.
(33) Hassanali, A. A.; Singer, S. J. Model for the Water−Amorphous Silica Interface: The Undissociated Surface. *J. Phys. Chem. B* **2007**, *111* (38), 11181−11193.
(34) Cole, D. J.; Payne, M. C.; Csányi, G.; Mark Spearing, S.; Colombi Ciacchi, L. Development of a Classical Force Field for the Oxidized Si Surface: Application to Hydrophilic Wafer Bonding. *J. Chem. Phys.* **2007**, *127* (20), 204704−204704−12.
(35) Cruz-Chu, E. R.; Aksimentiev, A.; Schulten, K. Water−Silica Force Field for Simulating Nanodevices. *J. Phys. Chem. B* **2006**, *110* (43), 21497−21508.
(36) Kramer, G. J.; Farragher, N. P.; van Beest, B. W. H.; van Santen, R. A. Interatomic Force Fields for Silicas, Aluminophosphates, and Zeolites: Derivation Based on Ab Initio Calculations. *Phys. Rev. B: Condens. Matter Mater. Phys.* **1991**, *43* (6), 5068−5080.
(37) Vashishta, P.; Kalia, R. K.; Rino, J. P.; Ebbsjö, I. Interaction Potential for SiO_2: A Molecular-Dynamics Study of Structural Correlations. *Phys. Rev. B: Condens. Matter Mater. Phys.* **1990**, *41* (17), 12197−12209.
(38) Hassanali, A. A.; Zhang, H.; Knight, C.; Shin, Y. K.; Singer, S. J. The Dissociated Amorphous Silica Surface: Model Development and Evaluation. *J. Chem. Theory Comput.* **2010**, *6* (11), 3456−3471.
(39) Butenuth, A.; Moras, G.; Schneider, J.; Koleini, M.; Köppen, S.; Meißner, R.; Wright, L. B.; Walsh, T. R.; Ciacchi, L. C. Ab Initio Derived Force-Field Parameters for Molecular Dynamics Simulations of Deprotonated Amorphous-SiO_2/water Interfaces. *Phys. Status Solidi B* **2012**, *249* (2), 292−305.
(40) Emami, F. S.; Puddu, V.; Berry, R. J.; Varshney, V.; Patwardhan, S. V.; Perry, C. C.; Heinz, H. Force Field and a Surface Model Database for Silica to Simulate Interfacial Properties in Atomic Resolution. *Chem. Mater.* **2014**, *26* (8), 2647−2658.
(41) Heinz, H.; Lin, T.-J.; Mishra, R. K.; Emami, F. S. Thermodynamically Consistent Force Fields for the Assembly of Inorganic, Organic, and Biological Nanostructures: The INTERFACE Force Field. *Langmuir* **2013**, *29* (6), 1754−1765.
(42) Haria, N. R.; Lorenz, C. D. Ion Exclusion and Electrokinetic Effects Resulting from Electro-Osmotic Flow of Salt Solutions in Charged Silica Nanopores. *Phys. Chem. Chem. Phys.* **2012**, *14* (17), 5935−5944.
(43) Zhang, H.; Hassanali, A. A.; Shin, Y. K.; Knight, C.; Singer, S. J. The Water-Amorphous Silica Interface: Analysis of the Stern Layer and Surface Conduction. *J. Chem. Phys.* **2011**, *134* (2), 024705.
(44) Joseph, S.; Aluru, N. R. Hierarchical Multiscale Simulation of Electrokinetic Transport in Silica Nanochannels at the Point of Zero Charge. *Langmuir* **2006**, *22* (21), 9041−9051.
(45) Skelton, A. A.; Fenter, P.; Kubicki, J. D.; Wesolowski, D. J.; Cummings, P. T. Simulations of the Quartz$(10\bar{1}1)$/Water Interface: A Comparison of Classical Force Fields, Ab Initio Molecular Dynamics, and X-Ray Reflectivity Experiments. *J. Phys. Chem. C* **2011**, *115* (5), 2076−2088.
(46) Skelton, A. A.; Wesolowski, D. J.; Cummings, P. T. Investigating the Quartz $(10\bar{1}0)$/Water Interface Using Classical and Ab Initio Molecular Dynamics. *Langmuir* **2011**, *27* (4), 8700−8709.
(47) Wander, M. C. F.; Clark, A. E. Structural and Dielectric Properties of Quartz−Water Interfaces. *J. Phys. Chem. C* **2008**, *112* (50), 19986−19994.
(48) Bourg, I. C.; Steefel, C. I. Molecular Dynamics Simulations of Water Structure and Diffusion in Silica Nanopores. *J. Phys. Chem. C* **2012**, *116* (21), 11556−11564.
(49) Vlcek, L.; Zhang, Z.; Machesky, M. L.; Fenter, P.; Rosenqvist, J.; Wesolowski, D. J.; Anovitz, L. M.; Predota, M.; Cummings, P. T. Electric Double Layer at Metal Oxide Surfaces: Static Properties of the Cassiterite−Water Interface. *Langmuir* **2007**, *23* (9), 4925−4937.
(50) Předota, M.; Bandura, A. V.; Cummings, P. T.; Kubicki, J. D.; Wesolowski, D. J.; Chialvo, A. A.; Machesky, M. L. Electric Double Layer at the Rutile (110) Surface. 1. Structure of Surfaces and Interfacial Water from Molecular Dynamics by Use of Ab Initio Potentials. *J. Phys. Chem. B* **2004**, *108* (32), 12049−12060.
(51) Předota, M.; Zhang, Z.; Fenter, P.; Wesolowski, D. J.; Cummings, P. T. Electric Double Layer at the Rutile (110) Surface. 2. Adsorption of Ions from Molecular Dynamics and X-Ray Experiments. *J. Phys. Chem. B* **2004**, *108* (32), 12061−12072.
(52) Zhang, Z.; Fenter, P.; Cheng, L.; Sturchio, N. C.; Bedzyk, M. J.; Předota, M.; Bandura, A.; Kubicki, J. D.; Lvov, S. N.; Cummings, P. T.; et al. Ion Adsorption at the Rutile−Water Interface: Linking Molecular and Macroscopic Properties. *Langmuir* **2004**, *20* (12), 4954−4969.
(53) Skelton, A. A.; Walsh, T. R. Interaction of Liquid Water with the Rutile TiO_2 (110) Surface. *Mol. Simul.* **2007**, *33* (4−5), 379−389.
(54) Fenter, P.; Lee, S. S.; Skelton, A. A.; Cummings, P. T. Direct and Quantitative Comparison of Pixelated Density Profiles with High-Resolution X-Ray Reflectivity Data. *J. Synchrotron Radiat.* **2010**, *18* (2), 257−265.
(55) Bandura, A. V.; Kubicki, J. D.; Sofo, J. O. Comparisons of Multilayer H_2O Adsorption onto the (110) Surfaces of α-TiO_2 and SnO_2 as Calculated with Density Functional Theory. *J. Phys. Chem. B* **2008**, *112* (37), 11616−11624.
(56) Humphrey, W.; Dalke, A.; Schulten, K. VMD: Visual Molecular Dynamics. *J. Mol. Graphics* **1996**, *14* (1), 33−38, 27−28.
(57) Kubicki, J. D. Personal communication.
(58) Kubicki, J. D.; Sofo, J. O.; Skelton, A. A.; Bandura, A. V. A New Hypothesis for the Dissolution Mechanism of Silicates. *J. Phys. Chem. C* **2012**, *116* (33), 17479−17491.
(59) Berendsen, H. J. C.; Grigera, J. R.; Straatsma, T. P. The Missing Term in Effective Pair Potentials. *J. Phys. Chem.* **1987**, *91* (24), 6269−6271.
(60) Joung, I. S.; Cheatham, T. E. Determination of Alkali and Halide Monovalent Ion Parameters for Use in Explicitly Solvated Biomolecular Simulations. *J. Phys. Chem. B* **2008**, *112* (30), 9020−9041.
(61) Palmer, B. J.; Pfund, D. M.; Fulton, J. L. Direct Modeling of EXAFS Spectra from Molecular Dynamics Simulations. *J. Phys. Chem.* **1996**, *100* (32), 13393−13398.
(62) Hess, B.; Kutzner, C.; van der Spoel, D.; Lindahl, E. GROMACS 4: Algorithms for Highly Efficient, Load-Balanced, and Scalable Molecular Simulation. *J. Chem. Theory Comput.* **2008**, *4* (3), 435−447.
(63) Yeh, I.-C.; Berkowitz, M. L. Ewald Summation for Systems with Slab Geometry. *J. Chem. Phys.* **1999**, *111* (7), 3155−3162.
(64) Bellucci, F.; Lee, S. S.; Kubicki, J. D.; Bandura, A.; Zhang, Z.; Wesolowski, D. J.; Fenter, P. Rb^+ Adsorption at the Quartz(101)−Aqueous Interface: Comparison of Resonant Anomalous X-Ray Reflectivity with Ab Initio Calculations. *J. Phys. Chem. C* **2015**, *119* (9), 4778−4788.
(65) Schlegel, M. L.; Nagy, K. L.; Fenter, P.; Sturchio, N. C. Structures of Quartz (100)- and (101)-Water Interfaces Determined

DOI: 10.1021/acs.jpcc.5b00096
J. Phys. Chem. C 2015, 119, 9274−9286

by X-Ray Reflectivity and Atomic Force Microscopy of Natural Growth Surfaces. *Geochim. Cosmochim. Acta* **2002**, *66* (17), 3037−3054.
(66) Předota, M.; Machesky, M. L.; Wesolowski, D. J.; Cummings, P. T. Electric Double Layer at the Rutile (110) Surface. 4. Effect of Temperature and pH on the Adsorption and Dynamics of Ions. *J. Phys. Chem. C* **2013**, *117* (44), 22852−22866.
(67) Hiemstra, T.; Van Riemsdijk, W. H. A Surface Structural Approach to Ion Adsorption: The Charge Distribution (CD) Model. *J. Colloid Interface Sci.* **1996**, *179* (2), 488−508.
(68) Smit, W. Surface Complexation Constants of the Site Binding Model. *J. Colloid Interface Sci.* **1986**, *113* (1), 288−291.
(69) Sverjensky, D. A. Prediction of Surface Charge on Oxides in Salt Solutions: Revisions for 1:1 (M^+L^-) Electrolytes. *Geochim. Cosmochim. Acta* **2005**, *69* (2), 225−257.
(70) Sahai, N.; Sverjensky, D. A. Evaluation of Internally Consistent Parameters for the Triple-Layer Model by the Systematic Analysis of Oxide Surface Titration Data. *Geochim. Cosmochim. Acta* **1997**, *61* (14), 2801−2826.
(71) Sverjensky, D. A. Interpretation and Prediction of Triple-Layer Model Capacitances and the Structure of the Oxide-Electrolyte-Water Interface. *Geochim. Cosmochim. Acta* **2001**, *65* (21), 3643−3655.
(72) Shchukarev, A. Electrical Double Layer at the Mineral-Aqueous Solution Interface as Probed by XPS with Fast-Frozen Samples. *J. Electron Spectrosc. Relat. Phenom.* **2010**, *176* (1−3), 13−17.
(73) Shchukarev, A.; Rosenqvist, J.; Sjöberg, S. XPS Study of the Silica−Water Interface. *J. Electron Spectrosc. Relat. Phenom.* **2004**, *137*−*140*, 171−176.
(74) Dewan, S.; Carnevale, V.; Bankura, A.; Eftekhari-Bafrooei, A.; Fiorin, G.; Klein, M. L.; Borguet, E. Structure of Water at Charged Interfaces: A Molecular Dynamics Study. *Langmuir* **2014**, *30* (27), 8056−8065.

DOI: 10.1021/acs.jpcc.5b00096
J. Phys. Chem. C 2015, 119, 9274−9286

[OK2]

Kabeláč M., **Kroutil O.**, Předota M., Lankaš F., Šíp M.

Influence of a charged graphene surface on the orientation and conformation of covalently attached oligonucleotides: a molecular dynamics study

Physical Chemistry Chemical Physics 14 (12), 4217-4229, (2012)

[IF(2014) = 4.493]

Participation of Ondřej Kroutil:

OK prepared the model of graphene and attached oligonucleotide, performed several molecular dynamics simulations and participated in the paper writing.

Influence of a charged graphene surface on the orientation and conformation of covalently attached oligonucleotides: a molecular dynamics study. Kabeláč M., Kroutil O., Předota M., Lankaš F., Šíp M. Physical Chemistry Chemical Physics 2012,14, 4217-4229

DOI: 10.1039/C2CP23540D. Reproduced from [OK2] with permission from the PCCP Owner Societies.

PCCP

Cite this: DOI: 10.1039/c2cp23540d

www.rsc.org/pccp

PAPER

Influence of a charged graphene surface on the orientation and conformation of covalently attached oligonucleotides: a molecular dynamics study†

M. Kabeláč,*[ab] O. Kroutil,[c] M. Předota,[b] F. Lankaš[a] and M. Šíp*[c]

Received 10th November 2011, Accepted 6th February 2012
DOI: 10.1039/c2cp23540d

Molecular dynamics (MD) simulations of single-stranded (ss) and double-stranded (ds) oligonucleotides anchored *via* an aliphatic linker to a graphene surface were performed in order to investigate the role of the surface charge density in the structure and orientation of attached DNA. Two types of interactions of DNA with the surface are crucial for the stabilisation of the DNA–surface system. Whereas for a surface with a zero or low positive charge density the dispersion forces between the base(s) and the surface dominate, the higher charge densities applied on the surface lead to a strong electrostatic interaction between the phosphate groups of DNA, the surface and the ions. At high-charge densities, the interaction of the DNA with the surface is strongly affected by the formation of a low-mobility layer of counterions compensating for the charge of the surface. A considerable difference in the behaviour of the ds-DNA and ss-DNA anchored to the layer was observed. The ds-DNA interacts with the surface at low- and zero-charge densities exclusively by the nearest base pair. It keeps its geometry close to the canonical B-DNA form, even at surfaces with high-charge densities. The ss-DNA, owing to its much higher flexibility, has a tendency to maximise the attraction to the surface exploiting more bases for the interaction. The interaction of the polar amino group(s) of the base(s) of ss-DNA with a negatively charged surface also contributes significantly to the system stability.

I. Introduction

Microarrays or DNA chips are arrays of tens to tens of thousands of microscopic spots containing single-stranded deoxyribonucleotides attached to a solid surface (such as a membrane, a polymer, or glass) used to analyse simultaneously a sample solution containing fragments of nucleic acids. Oligonucleotides (capture probes) in individual spots are identical, but their sequences are different for each spot to match the various complementary DNA sequences (targets) present in a given sample. The extent of binding of a complementary fragment to the surface-attached oligonucleotides is detected mainly fluorometrically.[1–5]

Originally, the main application of microarrays was gene-expression screening. At present, microarrays can be used to detect DNA or RNA sequences of pathogens, organisms, mutations or generally speaking any characteristic sequence of any object of interest: DNA microarrays are used for the detection and identification of bacteria and genes of interest from various environments (*e.g.* soil, sediment, water column),[6] they are suitable for the detection of single nucleotide polymorphisms[7,8] and for many other practical applications, such as for example the detection of viruses.[9–11]

The sequences of surface-immobilised capture probes are designed in a similar manner and according to the same principle as those for probes or primers in a bulk solution: they should not allow the formation of internal structures such as hairpins. They should be sensitive to sequence variations and bind only to complementary strands. The hybridisation on an array requires a similar melting temperature for all of the capture probes. There are many software tools available for probe design that are used during the process of microarray development such as those presented by Li and Wernersson.[12,13] Nevertheless, all of them are based on standard hybridisation conditions, *i.e.* nucleic acids in solution, not being attached to a surface.

However, the surface plays an important role. First, the capture probes are immobilised to a certain extent by surface binding and therefore their molecular dynamics is different

[a] *Institute of Organic Chemistry and Biochemistry, Academy of Sciences of the Czech Republic, Flemingovo nám. 2, 166 10 Prague 6, Czech Republic*
[b] *Faculty of Science, University of South Bohemia, Branišovská 31, 370 05 České Budějovice, Czech Republic. E-mail: martin.kabelac@uochb.cas.cz*
[c] *Faculty of Health and Social Studies, University of South Bohemia, J. Boreckého 27, 37 011 České Budějovice, Czech Republic. E-mail: sip@zsf.jcu.cz*
† Electronic supplementary information (ESI) available. See DOI: 10.1039/c2cp23540d

from that describing a system of two free strands in a solution. Second, the presence of the surface and the interactions of the capture probe with the surface represent an important sterical hindrance making single-strand–double-strand transitions more difficult. Third, in addition to the van der Waals interactions, the surface, whether it is charged or not, generates nontrivial electrostatics and interfacial structure owing to the interactions between the solution and the surface, influencing the density profiles of the water and ions in the vicinity of the surface and attached probes.

In order to accelerate hybridisation, various experimental enhancements have been proposed, such as flow-chamber hybridisation and the application of electrostatic fields. The first steps to estimate some of the aspects concerning the influence of the surface have already been made, based both on experiments[14,15] and on theoretical considerations,[16,17] but the underlying phenomena remain poorly understood.

This molecular study elucidates the role of the surface and the electric field in the spatial distribution of ions, the behaviour of the probes and targets and in the hybridisation process. The anchored microarrays on the surface are represented by a single-stranded oligomer of DNA, whereas the hybridised ones are represented by a double-stranded DNA with one strand (probe) covalently attached to the surface.

Various surfaces are used in biosensing and micro-array technologies. The most used one by far is a silica surface usually covered with various organic molecules in order to enhance or modify its hybridisation efficiency.[18–20] Other types of surfaces include various materials such as polymers, poly(methyl-meta acrylate) (PMMA),[21,22] poly(dimethylsiloxan) (PDMS),[23] polypropylene (PP),[24] gold,[25,26] graphene,[27–30] *etc.* The graphene surface has been selected as the substrate in our simulations, because it is a relatively simple but realistic surface and its structure is independent of pH, salt concentration, *etc.* Finally, some theoretical studies on DNA interaction with carbon nanotubes (with surfaces based on graphene geometry) have already been conducted.[31–37] The binding of DNA to carbon nanotubes has been identified as a way to open the door to carbon-nanotube-based applications in biotechnology.[34]

II. Simulation methods

A. System setup

Two graphene layers of a size of 68.16 × 66.41 Å and a separation of 61.40 Å were generated by the BuildCstruct 1.1 program.[38] Each layer consists of 1728 carbon atoms. The rectangular box contains the system of interest, *i.e.* DNA attached to a charged surface, water and ions. The role of the second graphene surface, which was always neutral, was to close the system. In order to minimise the influence of the electric field generated by the charged graphene layer on the periodic images, the replicas of the system were separated by a 100 Å vacuum gap. The whole model is depicted in Fig. 1.

The initial structures of both the double-stranded (ds-DNA) and single-stranded decamers (ss-DNA) with the base sequence 5′-CCACTAGTGG-3′ in the canonical B-form were generated using the NAB module implemented in the AmberTools 1.2 package.[39]

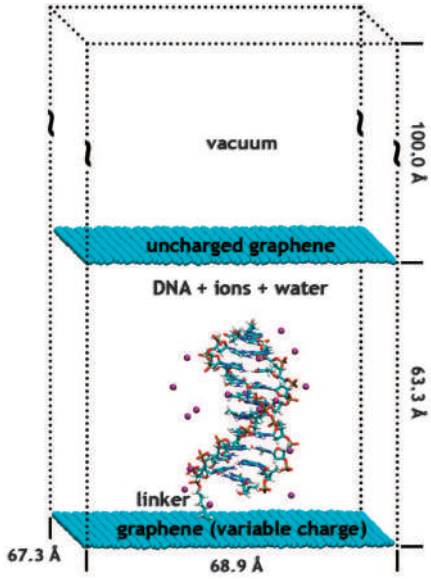

Fig. 1 A schematic representation of the simulated system.

The oligonucleotide was covalently bonded to the graphene layer *via* an aliphatic carbon linker consisting of six methylene groups (C6). The linker was attached to the 5′ end of the cytosine nucleotide by the phosphodiester bond. In the initial position, the DNA helix axis was orientated perpendicularly to the graphene slab.

In order to test the role of the charge of the graphene layer in the position and the orientation of the DNA, all of the carbon atoms of the graphene layer, to which DNA is anchored, were charged to one of the following values: −0.1, −0.05, −0.02, −0.01, 0, +0.01, +0.02, +0.05 or +0.1 elementary charge (e) per carbon, corresponding to the range of the charge densities −0.594 to +0.594 C m^{-2} comparable to those used in the experiments.[40,41] The sodium/chloride ions were used to neutralise fully the charge applied on the graphene, whereas the DNA was neutralised independently by sodium cations. All of the nominal charges per carbon atom, the charge densities and the number of ions used in the simulations are summarised in Table 1.

The probe surface density used in our study (2×10^{12} cm^{-2}) was selected to be of the same order of magnitude as a microarray maximum sensitivity for a 10-mer long probe (6×10^{12} cm^{-2}).[42]

For comparison, ds-DNA and ss-DNA with a minimum distance between the solute and boundaries set to 10 Å in a rectangular periodic box with no graphene layers were also simulated.

B. Parameters

The parmbsc0[43] modification of the parm99 force field for DNA was used, together with the TIP3P[44] water model and Na^+ counterions neutralising the negative charge of the DNA. New parameters[45] for Na^+ and Cl^- ions were adopted to prevent their cocrystallisation. The 'CA' atomic type for the

Table 1 Nominal and real charges per carbon atom, charge densities and number of ions used in the simulations

			Number of ions			
			ds-DNA		ss-DNA	
Nominal charge (e/carbon)	Real charge (e/carbon)	Charge density (C m^{-2})	Na^+	Cl^-	Na^+	Cl^-
−0.10	−0.09954	−0.594	191	0	182	0
−0.05	−0.04977	−0.297	105	0	96	0
−0.02	−0.01967	−0.118	53	0	44	0
−0.01	−0.00984	−0.059	36	0	27	0
0.00	0.00000	0.000	19	0	10	0
0.01	0.00984	0.059	19	17	10	17
0.02	0.01967	0.118	19	34	10	34
0.05	0.04977	0.297	19	86	10	86
0.10	0.09954	0.594	19	172	10	172

carbon atoms of graphene was employed similarly as in other papers simulating carbon-nanotube–DNA interactions.[32,46,47] The partial charges and structural parameters of the aliphatic C6 linker were found using the standard RESP procedure.[48]

C. Simulation methodology

All of the molecular dynamics simulations were carried out with an atomic resolution including all the hydrogens and in explicit water using the AMBER 9 suite of programs.[39] An initial equilibration protocol consisting of a series of energy minimisations and short restrained NPT MD runs resulted in a periodic box of a size of 68.9 × 67.3 Å in the x and y directions. The equilibration phase was followed by an NVT MD production run at 298 K. The restraint of 10 kcal mol^{-1} Å^{-2} on all of the graphene atoms was used for the production run in order to keep the graphene layer planar during the simulations. The separation of the two graphene layers in the z-direction, 63.3 Å, was sufficient to prevent the interaction of the 3′-DNA terminus with the neutral graphene layer. The Particle Mesh Ewald method to treat long-range interactions and the SHAKE algorithm on hydrogen atoms were used. Each trajectory was prolonged to 100 ns. The structures were saved every 1 ps.

D. Analysis of DNA geometry

The DNA conformation was described using the parameters commonly employed in DNA structural analysis. Inter-base-pair or step parameters (tilt, roll, twist, shift, slide and rise) were complemented by the intra-base-pair parameters buckle and propeller. For the ss-DNA, inter-base parameters analogous to the step parameters were employed. The 3DNA program[49] was used to compute the parameters.

To characterise the orientation of the DNA oligomer with respect to the graphene layer, two global geometry descriptors were introduced. First, we computed the distance between the graphene plane and the phosphorus atom of a phosphate group in the middle of the DNA. In the case of ds-DNA, the phosphorus of the strand closer to the graphene was selected. Second, we monitored the angle between the axis of the DNA oligomer and the normal vector of the graphene plane. Zero angle indicates that the DNA is perpendicular to the graphene layer, the angle of 90° corresponds to a DNA configuration parallel to the layer. The oligomer axis is defined as a directional average (*i.e.*, vector sum normalised to unity) of the normal vectors of the bases (ss-DNA) or base pairs (ds-DNA), with the exclusion of terminal bases or base pairs.

In the case of ds-DNA, it may seem more natural to define the oligomer axis as a directional average of the local helical axes for the individual steps. We tested this definition as well (the local axes were computed using the 3DNA program) and obtained results very similar to the normal vector definition. This is not surprising, since the oligomer retains the conformation close to the canonical B-DNA in which the helical axis is perpendicular to the base pair planes. On the other hand, the use of the local helical axes for the ss-DNA turned out to be completely misleading. The local helical axes as defined in the 3DNA program are local axes of rotation between adjacent base pairs or bases. If the structure is irregular, these axes may point in directions perpendicular to the overall shape of the oligomer. To avoid this artefact and to maintain consistency between ds-DNA and ss-DNA, the normal vector definition described above was used in both cases.

The electric charge axial densities were analysed by the g_potential utility of the GROMACS software package.[50]

III. Results and discussion

A. Double stranded DNA

The deviation of the helical axis from the normal vector of the graphene plane depending on the charge of the graphene layer is shown in Fig. 2. The distance of the phosphorus atom of ds-DNA, localised in the middle of the backbone of the closer strand of DNA to the layer, from the charged graphene layer during the MD simulation is shown in Fig. 3 for all of the studied atomic charges of the graphene atoms. The averaged values of above-mentioned properties from the already equilibrated part of the trajectory (last 70 ns) can be found in Table 2. The typical snapshots from the MD trajectories are depicted in Fig. 4.

The free ds-DNA oligomer shows local features consistent with the B-DNA conformational family. Apart from the terminal base pairs and steps, the oligomer retains its B-DNA-like conformation also in the presence of graphene, regardless of the charge of the graphene layer. See Table S1 (ESI†) for a list of the average local parameters.

Uncharged graphene. The interaction between the DNA and uncharged graphene is dominantly governed by dispersion forces mediated by the closest base pair orientated parallel with the graphene layer (Fig. 4). After approximately 5 ns of the MD simulation, the DNA is attracted to the graphene slab by changing the originally extended conformation of the linker to the coiled one. This is characterised by a shortening of the original distance of the central phosphorus atom of DNA to the graphene from the initial 27 Å to ∼15 Å. No further changes in the orientation of the DNA were observed for the rest of the simulation. The DNA remains more or less perpendicularly orientated to the graphene for the whole time of the simulation (an average deviation from perpendicularity of ∼18 degrees; see Table 2). Zhao[33] found similar results for a self-assembled layer of four ds-DNAs on the graphene surface. The angle between the DNA axes and the graphene-surface normal vector in his study varied between 0 and 40 degrees with an average of around 25 degrees. The dispersion interaction

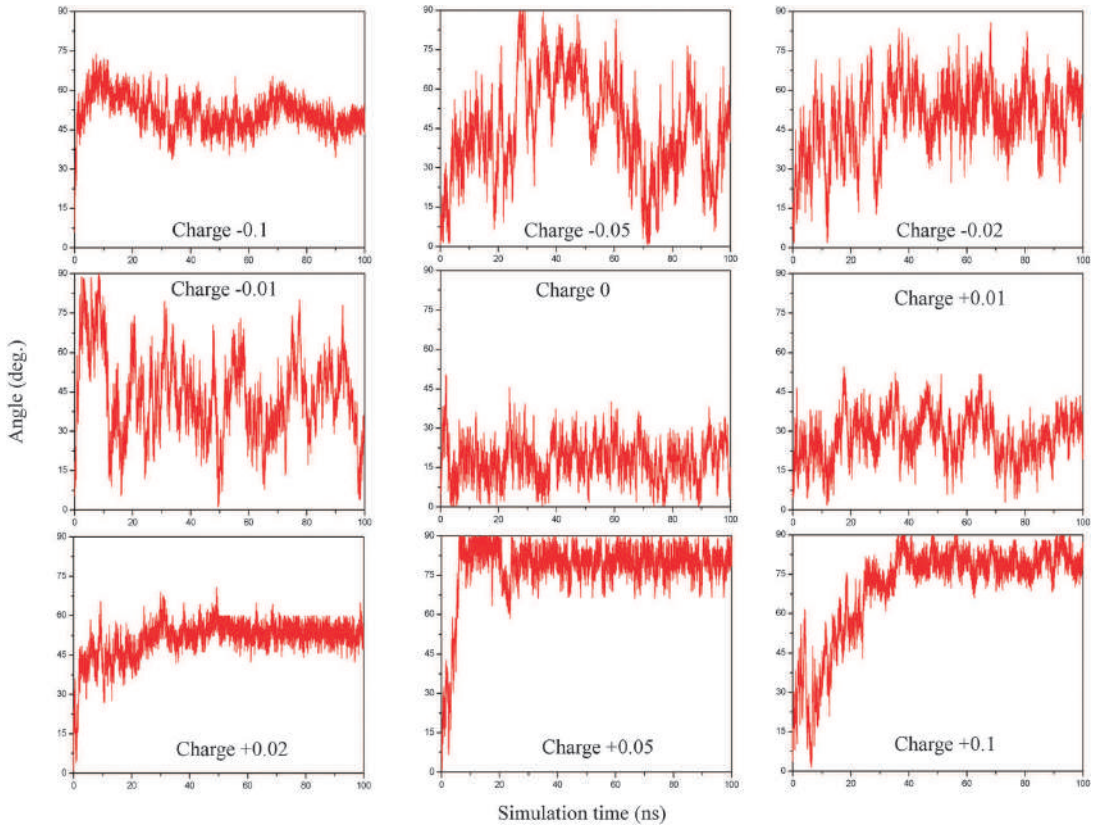

Fig. 2 The deviation of the helical axis of ds-DNA from the normal vector of the graphene plane in dependence on the charge of the graphene layer. The charge of the graphene atoms is indicated in each plot. Zero angle denotes the perpendicular orientation to the surface.

between a carbon nanotube (CNT) and the closest base pair of ds-DNA was also observed in the work of Zhao and Johnson.[46]

Negatively charged graphene. Already a relatively very small charge on each carbon atom of graphene (−0.01e) leads to qualitatively different results in comparison with the system containing uncharged graphene. The negatively charged phosphate groups of DNA are repelled by the negatively charged graphene layer, which results in the preservation of the extended conformation of the linker. The average distance of the central phosphorus of the DNA to the graphene is around 21 Å, but it fluctuates between 15 and 35 Å. The DNA orientation to the graphene surface is quite variable, between 0 and 70 degrees, with the average value of 42 degrees.

Similar conclusions can be drawn about the system containing graphene with an atomic charge of −0.02e. At the time of 11 ns, the disruption of H-bonds in the base pair closest to the graphene was observed. The cytosine base became orientated perpendicularly to the plane of the other bases starting to interact with the negatively charged slab *via* its amino group with partial positive charge. This motif is unique among all of the other systems of ds-DNA with negatively charged graphene, but it is frequently observed for systems containing ss-DNA. This behaviour of the ds-DNA can be explained by a destabilisation role of a negatively charged surface in the stability of the DNA duplex.[51]

When the charge of the carbon atoms of the graphene layer is enhanced to −0.05e, no new significant qualitative differences are observed in comparison with the less charged system. However, a slightly stronger preference of DNA to be situated closer to this surface than to the surface with charge −0.02 was detected, especially in the second half of the simulation. This behaviour can be explained by a significantly higher amount of sodium counterions situated close to the negatively charged graphene layer and having smaller mobility in comparison with simulations of less charged graphene. Thus, the negative phosphate groups of DNA start to feel the presence of the ordered counterions' layer. This can be deduced from the decrease of the average distance of the central phosphorus atom to the slab from 25 Å to 14 Å. Zhao[46] conducted simulations of unattached ds-DNA interacting with the negatively charged CNT (−0.05e per atom). As expected, since there was no linker, the DNA segment rapidly moved away from the CNT.

Applying the charge of −0.1e to all of the carbons of the graphene leads to rather surprising results. The surface of

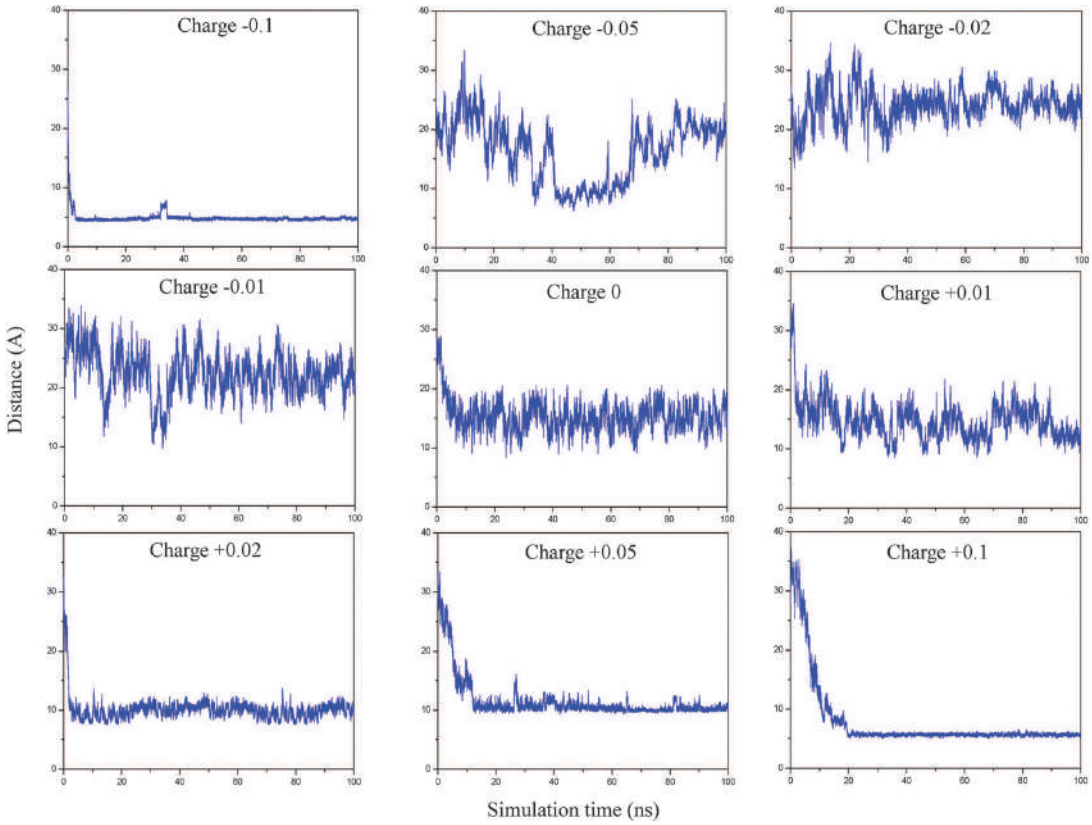

Fig. 3 The distance of the central phosphorus atom of ds-DNA from the graphene layer during the MD simulation. The charge of the graphene atoms is indicated in each plot.

Table 2 The averaged properties (for the definition see the Methods section) characterizing the orientation of the DNA to the graphene layer

	Double stranded DNA		Single stranded DNA	
Charge (e/carbon)	Distance/Å Mean ± SD	Angle/° Mean ± SD	Distance/Å Mean ± SD	Angle/° Mean ± SD
−0.10	4.9 ± 0.4	49.4 ± 4.8	4.1 ± 0.1	72.8 ± 9.3
−0.05	14.7 ± 4.9	47.4 ± 17.7	26.6 ± 2.7	74.6 ± 10.3
−0.02	24.2 ± 2.0	53.9 ± 9.6	25.1 ± 2.2	49.7 ± 18.4
−0.01	21.6 ± 3.3	42.0 ± 13.3	22.0 ± 2.8	34.5 ± 18.3
0.00	15.0 ± 2.1	18.0 ± 6.9	8.7 ± 0.3	83.0 ± 5.7
+0.01	14.0 ± 2.4	29.1 ± 8.4	14.5 ± 0.7	9.9 ± 4.9
+0.02	10.0 ± 0.9	53.9 ± 3.6	10.2 ± 0.4	80.1 ± 6.1
+0.05	10.4 ± 0.6	80.2 ± 4.3	7.8 ± 0.2	81.2 ± 6.8
+0.10	5.6 ± 0.2	79.4 ± 4.7	5.4 ± 0.2	82.8 ± 5.5

the graphene is fully covered by the layer of sodium cations with very low mobility. Thus, already in the equilibration period the DNA molecule is attracted to the graphene–sodium 'bilayer'. The direct contacts with cations are mostly mediated by phosphates, situated at the edges of the DNA, whereas the central part of DNA is somewhat bent, as characterised by the average value of the deviation of the helical axis from the normal vector of the graphene around 50 degrees. The average distance of the central phosphorus atom to the graphene remains constant at about 5 Å during almost all of the time of the simulation.

Positively charged graphene. The smallest positive charge applied to carbon atoms (+0.01e) has a rather minor influence on the distance and orientation of the DNA in comparison with the uncharged graphene. The dispersion forces still contribute dominantly to the attraction of DNA to the slab. However, a bend of the upper part of DNA (*i.e.* the part more distant from the slab) leading to an approach of this part to the layer indicates that the electrostatic attraction between the negatively charged phosphates of DNA and the positively charged slab is already non-negligible.

An increase of the charge of the graphene to +0.02e leads to mutual cooperation of the electrostatic and dispersion interactions between the DNA and the substrate. The closest base pair to the surface still interacts with the surface by dispersion forces, while the rest of the DNA is bent and orientated closer to the surface, allowing thus the interaction of the negative phosphates of the nearer strand with the positive graphene layer. It leads to the decrease of the distance of the central phosphorus atom of DNA to the slab from 15 Å to 10 Å in comparison with the previous simulation.

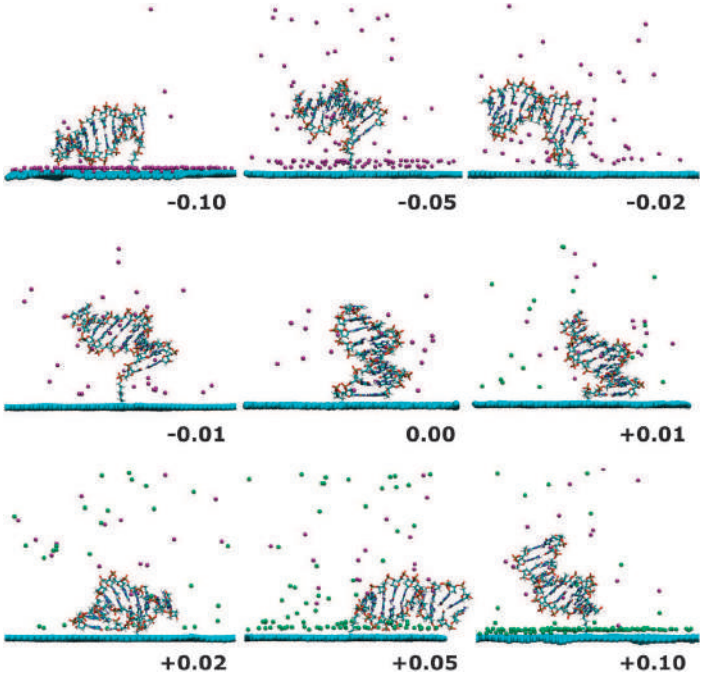

Fig. 4 The typical conformations of ds-DNA after the equilibrium is reached.

When the charge is increased to +0.05e, the electrostatic attraction becomes fully dominant, the ds-DNA is oriented parallel to the surface and thus no stacking interaction between the bases and the surface is observed.

However, since the canonical B-DNA structure of the ds-DNA is more or less conserved during the simulations, not all the phosphates interact with the surface. The middle part of the DNA remains somewhat deflected upon the graphene layer. This is probably the reason that the distance of the central phosphorus atom remains similar to the one in the case of the simulation with a less charged (+0.02e) graphene. The results agree well with the conclusions of Zhao and Johnson,[46] who simulated free ds-DNA adsorbed at the positively charged CNT (+0.05e per atom). They observed a similar bent structure of DNA with the ends closely attached to the CNT and slightly desorbed in the middle part of the DNA. This comparison might indicate the key role of stacking and electrostatic interactions of ds-DNA with carbon layers generally, regardless of the changes in the curvature of the surface.

For the system with the graphene charge of +0.1e, like in the case of graphene with carbons with a charge of −0.1e, the surface is fully covered by an almost immobile layer of counterions (here Cl^-). Initially, a rather strong repulsion between the chloride anions and phosphates leads to the extension of the linker as well as the DNA, resulting in a distance of the central phosphorus atom from the surface of about 35 Å. However, in the next 15 ns, the DNA bent down to the surface and eventually succeeded to penetrate through the layer of Cl^- to the graphene surface. It started to interact with the positive layer of graphene *via* the phosphates situated in the central part of DNA as well as at the terminal part of the DNA opposite the linker. The phosphates at the closest part of the DNA to the linker are far from the surface and thus do not contribute to the stabilisation of the DNA–graphene complex. This situation remains unchanged until the end of the simulation.

B. Single stranded DNA

The deviation of the helical axis of the ss-DNA from the normal vector of the graphene plane is shown in Fig. 5. The distance of the central phosphorus atom of the ss-DNA to the layer is provided in Fig. 6. The averaged values of above-mentioned properties from the already equilibrated part of the trajectory (last 70 ns, resp. 60 ns for the system with graphene of charge +0.1) can be found in Table 2. The typical snapshots from the MD trajectories are depicted in Fig. 7.

The free ss-DNA oligomer exhibits a regular, stacked structure. Neglecting the end bases, the inter-base parameters are not far from their double-stranded counterparts, with the notable exceptions of high positive shift and high twist. However, if a graphene layer is present, the ss-DNA shows severe structural distortions. This applies to all of the charges of the graphene layer, including the zero charge. A visual inspection of the MD snapshots suggests that the ss-DNA, being much more flexible than ds-DNA, uses its conformational freedom to optimise contacts with the graphene layer. The average local conformational parameters are given in Table S2 (ESI†).

Uncharged graphene. The first few nanoseconds of the simulation of the interaction of the ss-DNA with the uncharged graphene provide a picture similar to the simulation of ds-DNA,

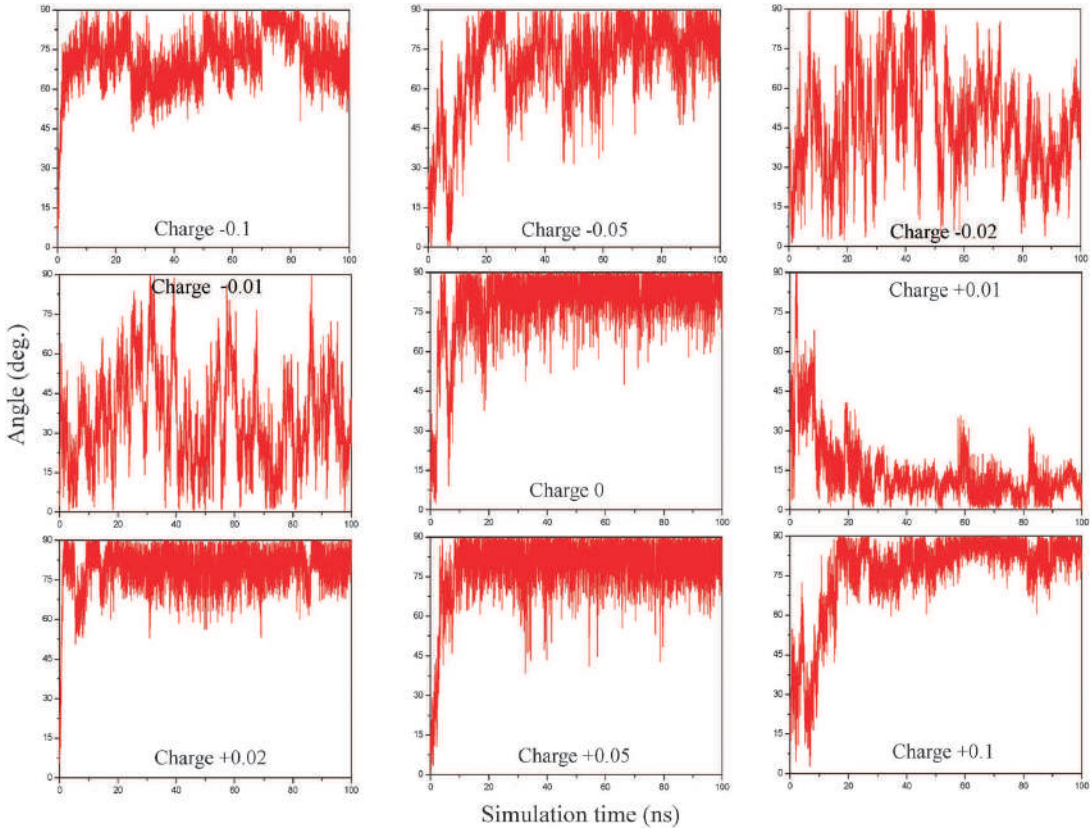

Fig. 5 The deviation of the helical axis of ss-DNA from the normal vector of the graphene plane in dependence on the charge of the graphene atoms. Zero angle denotes the perpendicular orientation to the surface.

i.e. the interaction with the surface is mediated only by the closest base to the surface.

However, an enormous flexibility of the sugar-phosphate backbone later led to a sorption of the unattached terminal base to the graphene surface and after several nanoseconds to a spreading of the single-stranded oligonucleotide onto the surface with some bases stacked and some not. Our conclusions are in agreement with other theoretical and experimental publications: Shi *et al.*[37] studied the adhesion and peeling of ss-DNA from an uncharged graphite surface and observed the DNA bases situated parallel to the surface with not all of the bases simultaneously attached to the substrate. Other simulations of ss-DNA–CNT hybrids[32,52] revealed that the vast majority of the sampled oligonucleotides had all of their bases adsorbed. The experimental results of Tang *et al.*[28] also support a hypothesis that the oligonucleotide adsorbs to a graphene surface with more than one base.

Negatively charged graphene. Since only one half of the negatively charged phosphates are presented and the functional groups of bases with positive partial charges are more accessible in the ss-DNA in comparison with the ds-DNA, a weaker repulsion between DNA and the surface can be expected. It has already been confirmed in the simulation with the smallest applied negative charge (−0.01e) on the carbon atoms of the graphene. The repulsive character of the interaction between DNA and the graphene was not observed like in the case of the simulation with the ds-DNA, but rather an attractive dispersion interaction between the closest base and the layer (a major part of the simulation) and attraction of the polar amino group of the closest cytosine and the graphene (a minor part) were seen.

When the charge of the carbons of the graphene is changed to −0.02e, the electrostatic interactions become the leading factor for the stabilisation of the DNA–graphene complex. The attraction of the amino group of the closest cytosine and the surface is crucial. Such an interaction pattern was also observed for the ds-DNA and the same charge of the graphene, where an unexpected breaking of the closest base pair to the surface was detected.

For the ss-DNA interacting with the graphene slab of charges −0.05e, two types of electrostatic attractions can be deduced: (i) the above-mentioned interaction of the closest cytosine with the surface (supplemented occasionally, especially in the second half of the simulation, by the interaction of the other bases with grapheme—typically an amino group of guanine at the opposite end of DNA); and (ii) the interaction

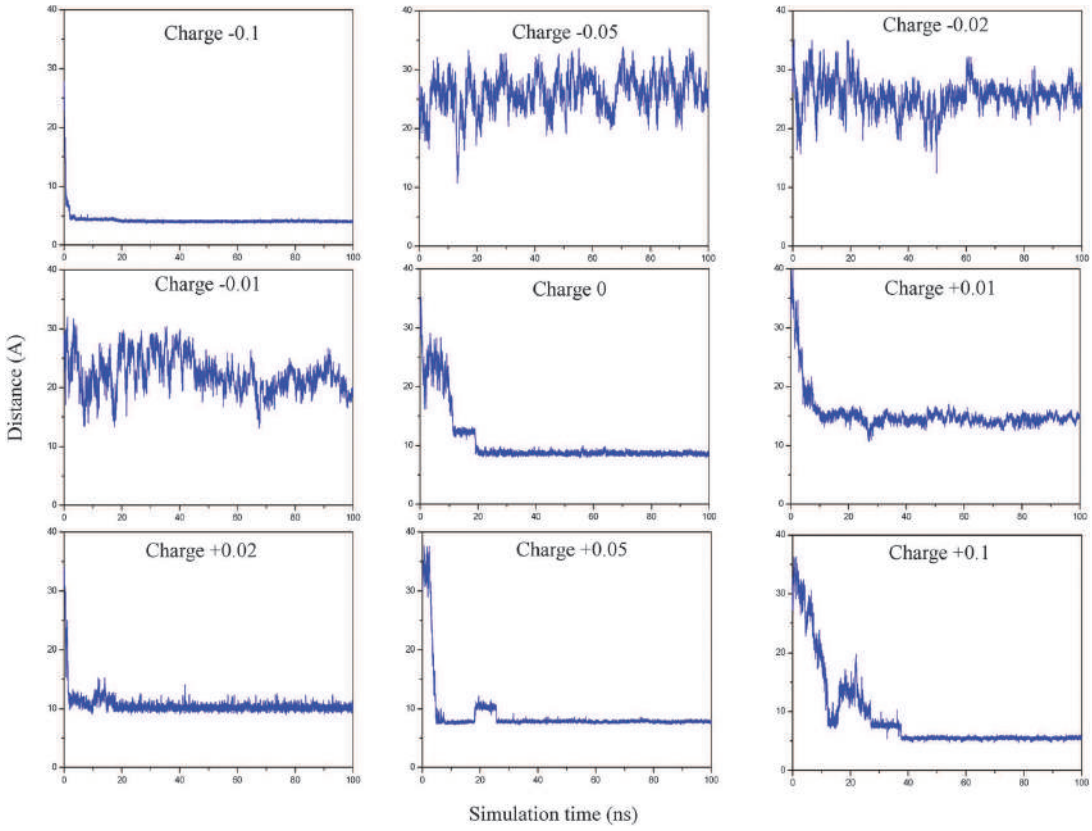

Fig. 6 The distance of the central phosphorus atom in Å of ss-DNA to the graphene layer during the MD simulation. The charge of the graphene atoms is indicated in each plot.

of the negatively charged sugar-phosphate backbone in the middle part of the ss-DNA with the counterions localised close to the surface, which became important after approx. 17 ns of the simulation.

The system containing graphene with the unit charge of −0.1e shows that the most important interaction between graphene and the DNA is mediated by the strong attraction between the phosphates and the oppositely charged, almost immobile layer of sodium cations, which are situated upon the graphene, similarly as in the case of ds-DNA. Since the ss-DNA is more flexible than ds-DNA, more phosphates are involved in the direct interaction with sodium cations than in the case of ds-DNA (the average distance of the central phosphorus atom from the surface is by 0.8 Å smaller). The bases point away from the surface, whereas ds-DNA retains its helical structure.

Positively charged graphene. Whereas for the ds-DNA the interaction motif with the graphene layer with charges of +0.01e remains similar to the one observed in the system with uncharged graphene, the ss-DNA benefits from the mutual cooperative effect of the electrostatic and dispersion interactions. This leads, approximately after 10 ns of the simulation, to a configuration where the whole ss-DNA is localised close to the surface and interacts *via* phosphates (by electrostatic forces) and as well as with majority of its bases (by dispersion forces) with the surface.

When the charge of the carbons in graphene is changed to +0.02e, the electrostatic attraction between the phosphates and the surface causes a parallel orientation of the DNA already in the early stage of the simulation. In addition, an electrostatic interaction of the guanine with the surface mediated *via* the O6 oxygen atom of the base is observed. Occasionally, one or a few bases still interact with the surface by dispersion forces.

For the system containing graphene with a charge of +0.05e on the carbon atoms, the electrostatic forces attracting the phosphates to the surface are crucial. However, like for the ds-DNA with the same charged graphene slab, it takes about 10 ns before the parallel orientation of the DNA with the surface is reached (probably owing to the presence of a non-negligible amount of chloride anions next to the surface). Generally the relaxation time of 10–25 ns is typical for reaching the equilibrated state for most of our simulations.

As for the ds-DNA at the surface with a charge of +0.1e, the ss-DNA remains extended and perpendicularly orientated

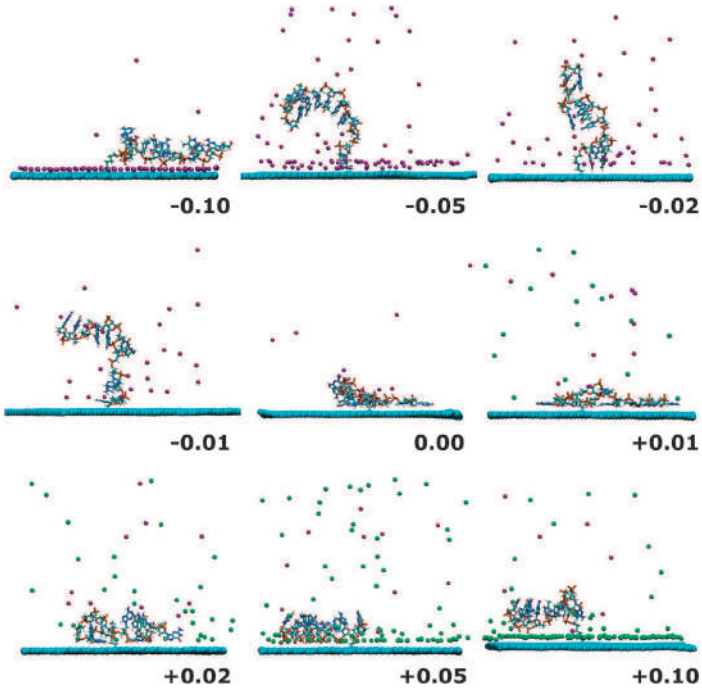

Fig. 7 The typical conformations of ss-DNA after the equilibrium is reached.

to the graphene surface covered by an almost immobile layer of counterions (Cl^-) at the beginning of the simulation. This rather strong repulsion between the chloride anions and phosphates leads to the extension of the linker as well as the DNA, resulting in an increase of the distance of the central phosphorus atom from the surface from an initial value of 27 Å to 38 Å within a few ns of the simulation. Later, the DNA gets closer to the surface and some of the phosphate groups are able to penetrate the chloride layer starting to interact directly with the positively charged layer. This conformational motif is similar to the motif observed by Wong *et al.*[53] Although their system had a higher charge density (0.711 C m^{-2}) and more ions compared to our system, they similarly noticed oligonucleotide with its last few bases forming a curved segment and closely interacting with the surface through its phosphate groups.

A graphical representation of the above-mentioned competition between base stacking and the electrostatic attraction of the phosphate group is depicted in Fig. 8. The increasing number of adsorbed phosphate groups with the increasing positive surface charge up to +0.05e can be seen from Fig. 8 both for ss-DNA and to a smaller extent also for ds-DNA, although the competition between base stacking and the phosphate groups' adsorption onto the surface is not as strong in the latter case.

C. Effect of the DNA sequence

Since in our study we used only one DNA sequence, the question arises: can the presented observations be applied generally on DNA, or are they specific for a given sequence? The effect of the DNA sequence can be expected to be more pronounced for neutral or low-charged surfaces. A higher ratio of purine bases can lead in the case of very flexible ss-DNA to a slightly stronger interaction with the graphene surface than for ss-DNA containing the pyrimidine-rich sequences. Sequence-specific interactions of the terminal bases are of limited practical importance, since the majority of the DNA probes used in experiments have identical bases at their ends (namely G/C, introduced to improve stability). The sequence specificity of the DNA–surface interactions likely diminishes for highly charged surfaces, where electrostatic interactions between the phosphates and the surface/ions play a dominant role.

D. Interaction of ions with the surface

So far, we have discussed the role of the ions surrounding the DNA and also interacting with the surface only qualitatively based on simulation snapshots (Fig. 4 and 7). Here, we quantify the adsorption of ions and the role of the presence of DNA in the distribution of ions.

The axial density profiles of ions interacting with the surface are given in Fig. 9. As expected, the distribution is rather independent of the presence of ds-DNA or ss-DNA because of the dominating effect of the direct surface–ion interactions. This is also confirmed by selected simulations (for charges −0.05e, 0e and +0.05e) of the graphene surface interacting with aqueous solutions of ions without DNA. Only for a neutral surface or a small magnitude (±0.01e) of the surface charges are the curves qualitatively different owing to the

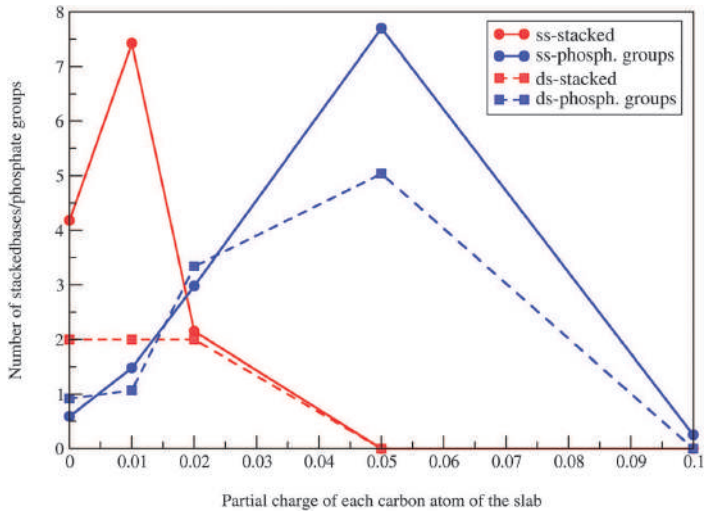

Fig. 8 Changes in the averaged number of stacked bases and adsorbed phosphate groups with increasing positive surface charge. Bases were considered as stacked when N1 and N3 atoms in their heteroatomic rings were within 4.5 Å from the surface. Similarly, a distance criterion for phosphate groups was set to 5.5 Å for the phosphorus atom. Equilibrated parts of simulations were considered in analysis. Since the negatively charged surface repels DNA, the dependence is depicted only for the positively charged and uncharged slab.

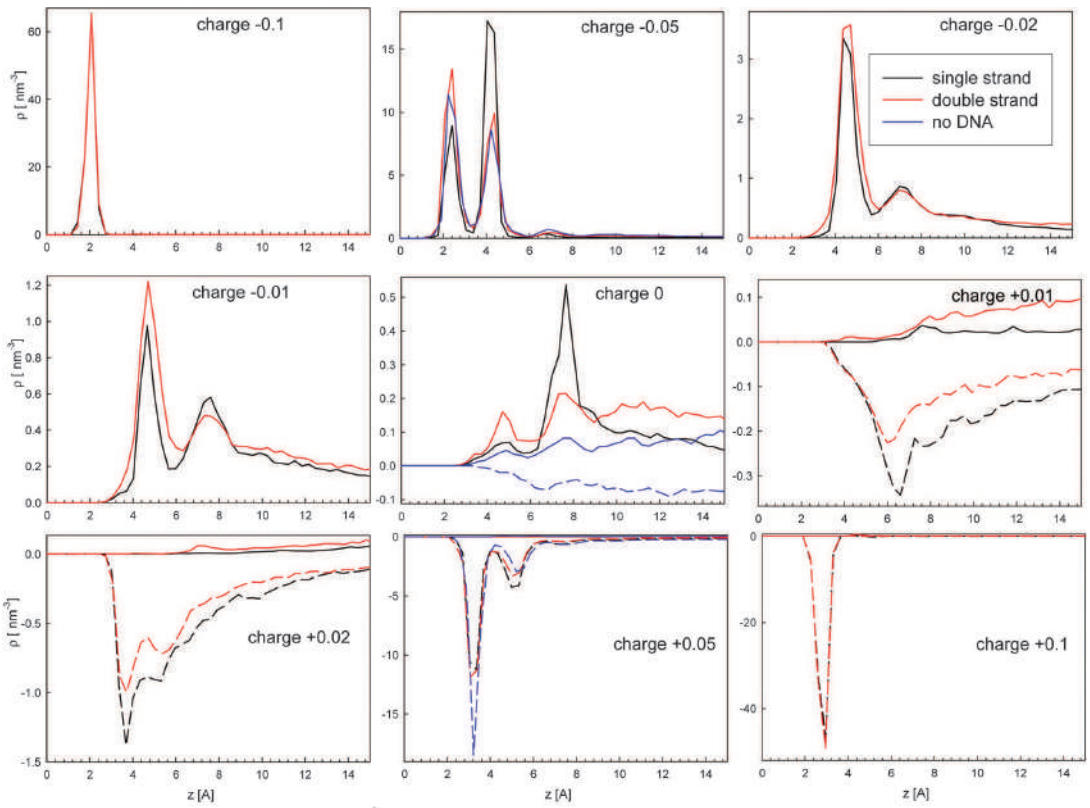

Fig. 9 Density profiles of Na^+ (solid lines, positive values) and Cl^- (dashed lines, negative values) as a function of distance from the graphene surface in the presence of ss-DNA, ds-DNA, and without DNA. Note the different vertical scales of the graphs.

different number of dissolved ions, including those compensating for the charge of the DNA, *cf.* Table 1.

For the most negative surface (charges −0.1e), we observed a single adsorption peak of Na^+ around 2 Å, which corresponds to inner-sphere adsorption of the ion. In this case, the ion is partially desolvated and directly interacts with the negatively charged carbon atoms. Charges of −0.05e cause the coexistence of both inner-sphere and outer-sphere adsorbed cations, with the latter fully solvated and around 4.3 Å. The position of the inner-sphere adsorbed ions shifts to slightly larger distances—2.4 Å from the surface. For smaller magnitudes of the carbon charges, the solvation dominates over electrostatics and no inner-sphere adsorption is observed.

A very similar situation is observed for anions at positively charged surfaces. At the largest carbon charges, +0.1e, all of the Cl^- adsorb as an inner-sphere complex at a height of around 2.8 Å from the graphene surface. The position of this peak is shifted to the longer distances compared to that of Na^+ at a negative surface because of the larger size of the Cl^- ions. For a surface with +0.05e charges, the inner-sphere adsorption shifts to 3.3 Å, but it still dominates and occurs even for a surface with charges of +0.02e, although followed by a range of adsorption distances with the increasing solvation of the Cl^-.

The formation of strong and well-defined adsorption peaks of either ions in the extremely charged systems explains why the observed behaviour of DNA in these cases does not follow the trend seen for smaller charges. As stated above, in these cases the DNA feels the layer of adsorbed counterions and the DNA conformation and its orientation to the layer depend on its ability to penetrate the layer of counterions and establish direct contact with the surface.

We should mention that for an even slightly higher surface charge density than studied here, Wong *et al.*[53] observed two adsorption peaks for Cl^- separated by ~2.2 Å, but that has been attributed to sandwiching of the surface ammonium coating of their β-cristobalite surface. In our case of a nearly perfectly flat surface, the formation of single or multiple adsorption layers of ions must be exclusively assigned to interplay between the surface and solvation interactions.

Finally, the role of the ions and the surface charge in the hybridisation processes should be discussed. The environment at the solid–liquid interface is very different from the bulk solution. As a result, the thermodynamics and kinetics of the solid-phase hybridisation differ substantially from those in the bulk. One of the key factors is the presence of cations. Špringer *et al.*[54] studied the effect of the monovalent and divalent cations on solid-phase DNA hybridisation. The authors found that the duplex stability is substantially lower than the one reported for the bulk (but still in the range of tens of kJ mol^{-1} for an oligomer). In the absence of magnesium, higher sodium concentrations stabilize the duplex. The hybridisation free energy depends linearly on the logarithm of the sodium concentration, as observed also in the bulk.[55] However, the slope is much lower in the solid phase than in the bulk. Thus, the sodium concentration influences the duplex stability much less in solid phase hybridisation than in the bulk. Our effective sodium concentration, based on the number of ions (Table 1) and the volume of the simulation box, varies between 60 mM and 1 M. This corresponds to the difference in the hybridisation free energy[56] of just only 1 kJ mol^{-1}.

The surface hybridisation kinetics is also very different from that in the bulk. Gao *et al.*[56] found that the hybridisation rate constants at the surface drop by a factor of 20–40 compared to the bulk. The authors also observed that the hybridisation rate increases with increasing salt concentration (a several fold increase with the NaCl concentration changing from 100 mM to 1 M). Peterson *et al.*[57] studied the rate of DNA adsorption onto the surface and found roughly a 5-fold increase in the adsorption rate upon changing the NaCl concentration from 50 mM to 1 M. Note, however, that the time scales of DNA hybridisation are orders of magnitude longer than our simulation times. Indeed, based on the rate constants at 0.5 M NaCl reported by Gao *et al.*,[56] the characteristic time of the hybridisation reaction in our systems would be about 1 ms.

IV. Conclusions

As far as the local conformation is concerned, our results suggest that the ds-DNA retains its B-DNA features regardless of the presence of the graphite layer and its charge, except for terminal base pairs and steps. In contrast, the ss-DNA exhibits an ordered stacked helical structure if left free in solution, but it shows localised structural collapse when a graphene layer is present, even if it is not charged.

Under physiological conditions, a DNA molecule is negatively charged and polar, owing to the negatively charged phosphate groups in its backbone. Thus a strong influence on its orientation to the surface was expected when the charge of the layer was varied. Our simulation of both ss-DNA and ds-DNA anchored on the differently charged graphene layer fully confirmed that the orientation of the DNA is extremely sensitive to the charge density of the layer.

A. Uncharged layer

Interactions between the ds-DNA and graphene are mediated, besides by the tether, by the dispersion forces between the closest base pair. The DNA molecule is orientated more or less perpendicularly to the surface. On the other hand, interactions between the surface and the ss-DNA confirm both the experimental and theoretical results,[28,37,58] namely that more bases than merely the first one are adsorbed to the surface because of the higher flexibility of the ss-DNA.

B. Positively charged layer

When a low charge density is applied on the graphene layer, the dispersion forces in conjunction with the weak electrostatic attraction are responsible for the interaction between the DNA and the layer. At medium positive surface charge densities, 0.12–0.3 C m^{-2} (corresponding to partial charges +0.02 and +0.05e at each carbon atom of the surface), the electrostatic attraction of the phosphate group and the layer becomes undoubtedly dominant both for the ss- and ds-DNA.

For a highly positive charged surface, the situation is complicated by the presence of a high amount of chloride counterions, creating along with the graphene a bilayer, which is negatively charged at the side facing the DNA. Thus, the DNA is repelled from the surface and remains in the perpendicular

orientation to the surface at the first stage of the simulation. However, the DNA is later capable of disrupting the layer of counterions and begins to interact directly with the graphene by the phosphate groups.

C. Negatively charged layer

For the layers with low and medium negative charge densities, -0.06 to -0.3 C m^{-2} (corresponding to partial charges -0.01, -0.02 and -0.05e at each carbon atom of the surface), a rather repulsive interaction was observed for the ds-DNA, whereas the ss-DNA prefers to interact with the charged graphene by its polar groups of the bases with a positive partial charge.

For the systems with the highest applied negative charge density on the graphene, an oppositely charged layer of counterions was again formed. A strong attraction of the phosphates with the sodium cations was observed immediately after the beginning of the simulations both for the ss- and ds-DNA.

D. Ions

For surface charge densities in the range -0.12 to 0.12 C m^{-2}, the ions adsorb predominantly as outer-sphere complexes with a limited effect on the DNA–surface interactions. However, for the largest magnitudes of surface charges (-0.1, $+0.05$ and $+0.1$e per carbon atom, *i.e.* -0.6, $+0.3$, $+0.6$ C m^{-2}), the formation of a counterion inner-sphere layer becomes a key factor in reversing the trends and effective charge of the surface. Being a smaller ion compared to Cl^-, Na^+ solvation is stronger, which leads to a mixed adsorption of Na^+ at a surface charge density of -0.3 C m^{-2} in two distinct inner-sphere and outer-sphere geometries.

E. Hybridisation

The molecular dynamics simulations performed do not show due to different time scales the process of DNA hybridisation directly. However, important indirect indices have been observed showing how the proximity of the graphene surface may influence the formation or melting of the DNA duplex. The practical applications of hybridisation with surface-bound probes depend not only on the stability of the duplex formed but also on other parameters such as hybridisation kinetics, sensitivity and selectivity, which, in this case, become also functions of the parameters characterising the surface and its interactions with the DNA.

We have demonstrated that hybridisation with surface-bound probes could benefit from both electrostatic and stacking interactions between the DNA and the graphene layer. As expected, the B-form structure of the double helix itself is not affected by the vicinity of the moderately charged surface, in agreement with the experimental results.[28,59] One exception to this rule was observed, namely the dangling end created on the target strand by the above-mentioned attractive interaction of the first nucleobase of the probe with the graphene surface. Both duplex formation and melting are cooperative mechanisms and (de)stabilisation of a single base-pair may induce a global DNA conformation change. Therefore, this finding should not be underestimated.

The application of an attractive electric field could in principle solve a serious problem of microarray technology—the slow hybridisation rates.[58] On the other hand, the multiple stacking interactions between the ss-DNA bases and graphene that were observed on a positive surface up to a charge density of $\sim$0.1 C m^{-2} represent a serious problem for hybridisation. Depending on the surface charge, the accessibility of the probes is reduced and the double-helix formation is slowed down if not stopped. This result clearly shows why the increase in the surface layer concentration of the target, created by the attractive electric field, which should accelerate the hybridisation kinetics, is not directly reflected by the overall hybridisation rate owing to the steric hindrance when the probes are collapsed on the surface of the chip. It is well known that hybridisation depends on many parameters such as temperature, probe and target lengths, on the composition of the buffer, on zwitterions and on the surface chemistry in the presence of electric fields. Our results elucidating the influence of the surface were obtained with a short oligonucleotide model. Similar surface-effects (steric hindrance, electrostatic and stacking interactions with graphene) can be expected with mutually non-interacting long oligonucleotides (> 30 nucleotides). The behaviour of mutually interacting probes in the so-called brush region of surface concentrations may differ from our results and should be treated separately.

The model system considered in our work is interesting for practical applications not only for its potential to accelerate hybridisation. The graphene properties are similar to graphite, a widely used material. Graphite, being composed of non-covalently bonded sheets of graphene, in principle leads to a bit more longer-ranged vdW interactions (coarse-graining of interaction with a single plane leads to 10-4 Steele potential, while that with half-space bulk material to 9-3 potential),[59] however considering the strong and long-range effect of electrostatics, the effect of the difference between graphene and graphite on observed trends is not expected—as long as the surface charge density is the same.

Graphene is able to quench the fluorescence of DNA attached fluorescent labels effectively.[60] The above-mentioned behaviour can be used for the preparation of new graphene-based microarrays with dye attached to the probe instead to the target DNA, where the hybridisation is detected by fluorescence intensity changes caused by the changing distance of the fluorescent label from the quenching surface.

Acknowledgements

This work was supported by Grants 204/09/J010 and 203/08/0094 (Czech Science Foundation), LC512 (Ministry of Education, Youth and Sports, Czech Republic) and No. IAA400550808 (Grant Agency of the Academy of Sciences of the Czech Republic) and was a part of the research project No. Z40550506 of the Institute of Organic Chemistry and Biochemistry, Academy of Sciences of the Czech Republic. F.L. gratefully acknowledges funding from the J.E. Purkyně Fellowship provided by the Academy of Sciences of the Czech Republic. The access to the MetaCentrum computing facilities provided under the programme "Projects of Large Infrastructure for Research, Development, and Innovations" LM2010005 funded by the Ministry of Education, Youth, and Sports of the Czech Republic is appreciated.

References

1 A. Sassolas, B. D. Leca-Bouvier and L. J. Blum, *Chem. Rev*., 2008, **108**, 109–139.
2 A. P. Abel, M. G. Weller, G. L. Duveneck, M. Ehrat and H. M. Widmer, *Anal. Chem*., 1996, **68**, 2905–2912.
3 M. F. Ali, R. Kirby, A. P. Goodey, M. D. Rodriguez, A. D. Ellington, D. P. Neikirk and J. T. McDevitt, *Anal. Chem*., 2003, **75**, 4732–4739.
4 J. A. Ferguson, T. C. Boles, C. P. Adams and D. R. Walt, *Nat. Biotechnol*., 1996, **14**, 1681–1684.
5 J. Li, W. Tan, K. Wang, D. Xiao, X. Yang, X. He and Z. Tang, *Anal. Sci*., 2001, **17**, 1149–1153.
6 J.-C. Avarre, P. de Lajudie and G. Bena, *J. Microbiol. Methods*, 2007, **69**, 242–248.
7 S. Ingebrandt, Y. Han, F. Nakamura, A. Poghossian, M. J. Schöning and A. Offenhäusser, *Biosens. Bioelectron*., 2007, **22**, 2834–2840.
8 A. Vainrub and B. M. Pettitt, *Biopolymers*, 2004, **73**, 614–620.
9 D. Bystřická, O. Lenz, I. Mráz, P. Dědič and M. Šíp, *Acta Virol. (Engl. Ed.)*, 2003, **47**, 41–44.
10 D. Bystřická, O. Lenz, I. Mráz, L. Piherová, S. Kmoch and M. Šíp, *J. Virol. Methods*, 2005, **128**, 176–182.
11 M. Šíp, D. Bystřická, S. Kmoch, L. Nosková, H. Hartmannová and P. Dědič, *J. Virol. Methods*, 2010, **165**, 64–70.
12 W. Li and X. Ying, *Appl. Bioinf*., 2006, **5**, 181–186.
13 R. Wernersson and H. B. Nielsen, *Nucleic Acids Res*., 2005, **33**, W611–W615.
14 R. J. Heaton, A. W. Peterson and R. M. Georgiadis, *Proc. Natl. Acad. Sci. U. S. A*., 2001, **98**, 3701–3704.
15 A. W. Peterson, R. J. Heaton and R. M. Georgiadis, *Nucleic Acids Res*., 2001, **29**, 5163–5168.
16 A. Vainrub and B. M. Pettitt, *Phys. Rev. E: Stat. Phys., Plasmas, Fluids, Relat. Interdiscip. Top*., 2002, **66**, 041905.
17 A. Vainrub and B. M. Pettitt, *Biopolymers*, 2003, **68**, 265–270.
18 B. J. Hong, S. J. Oh, T. O. Youn, S. H. Kwon and J. W. Park, *Langmuir*, 2005, **21**, 4257–4261.
19 N. Zammatteo, L. Jeanmart, S. Hamels, S. Courtois, P. Louette, L. Hevesi and J. Remacle, *Anal. Biochem*., 2000, **280**, 143–150.
20 S. Taylor, S. Smith, B. Windle and A. Guiseppi-Elie, *Nucleic Acids Res*., 2003, **31**, e87.
21 F. Fixe, M. Dufva, P. Telleman and C. B. V. Christensen, *Nucleic Acids Res*., 2004, **32**, e9.
22 N. Kimura, *Biochem. Biophys. Res. Commun*., 2006, **347**, 477–484.
23 D. Liu, R. K. Perdue, L. Sun and R. M. Crooks, *Langmuir*, 2004, **20**, 5905–5910.
24 M. S. Shchepinov, S. C. Case-Green and E. M. Southern, *Nucleic Acids Res*., 1997, **25**, 1155–1161.
25 A. Barhoumi, D. Zhang and N. J. Halas, *J. Am. Chem. Soc*., 2008, **130**, 14040–14041.
26 S. J. Hurst, A. K. R. Lytton-Jean and C. A. Mirkin, *Anal. Chem*., 2006, **78**, 8313–8318.
27 Y. Shao, J. Wang, H. Wu, J. Liu, I. A. Aksay and Y. Lin, *Electroanalysis*, 2010, **22**, 1027–1036.
28 Z. Tang, H. Wu, J. R. Cort, G. W. Buchko, Y. Zhang, Y. Shao, I. A. Aksay, J. Liu and Y. Lin, *Small*, 2010, **6**, 1205–1209.
29 S. Sorgenfrei, C.-Y. Chiu, R. L. Gonzalez, Y.-J. Yu, P. Kim, C. Nuckolls and K. L. Shepard, *Nat. Nanotechnol*., 2011, **6**, 126–132.
30 M. Pumera, *Mater. Today (Oxford, UK)*, 2011, **14**, 308–315.
31 G. Lu, P. Maragakis and E. Kaxiras, *Nano Lett*., 2005, **5**, 897–900.
32 R. R. Johnson, A. Kohlmeyer, A. T. C. Johnson and M. L. Klein, *Nano Lett*., 2009, **9**, 537–541.
33 X. Zhao, *J. Phys. Chem. C*, 2011, **115**, 6181–6189.
34 M. Zheng, A. Jagota, E. D. Semke, B. A. Diner, R. S. Mclean, S. R. Lustig, R. E. Richardson and N. G. Tassi, *Nat. Mater*., 2003, **2**, 338–342.
35 A. N. Enyashin, S. Gemming and G. Seifert, *Nanotechnology*, 2007, **18**, 245702.
36 M. Levitus, *J. Phys. Chem. Lett*., 2010, **1**, 1346–1350.
37 X. Shi, Y. Kong, Y. Zhao and H. Gao, *Acta Mech. Sin*., 2005, **21**, 249–256.
38 A. Minoia, Buildcstruct–Chembytes.
39 D. A. Case, T. E. Cheatham, T. Darden, H. Gohlke, R. Luo, K. M. Merz, A. Onufriev, C. Simmerling, B. Wang and R. J. Woods, *J. Comput. Chem*., 2005, **26**, 1668–1688.
40 A. Elaissari, P. Cros, C. Pichot, V. Laurent and B. Mandrand, *Colloids Surf., A*, 1994, **83**, 25–31.
41 S. Kuga, J.-H. Yang, H. Takahashi, K. Hirama, T. Iwasaki and H. Kawarada, *J. Am. Chem. Soc*., 2008, **130**, 13251–13263.
42 A. Vainrub and B. M. Pettitt, *J. Am. Chem. Soc*., 2003, **125**, 7798–7799.
43 A. Pérez, I. Marchán, D. Svozil, J. Šponer, T. E. Cheatham, C. A. Laughton and M. Orozco, *Biophys. J*., 2007, **92**, 3817–3829.
44 D. J. Price and C. L. Brooks, *J. Chem. Phys*., 2004, **121**, 10096–10103.
45 I. S. Joung and T. E. Cheatham, III, *J. Phys. Chem. B*, 2008, **112**, 9020–9041.
46 X. Zhao and J. K. Johnson, *J. Am. Chem. Soc*., 2007, **129**, 10438–10445.
47 G. Hummer, J. C. Rasaiah and J. P. Noworyta, *Nature*, 2001, **414**, 188–190.
48 W. D. Cornell, P. Cieplak, C. I. Bayly and P. A. Kollmann, *J. Am. Chem. Soc*., 1993, **115**, 9620–9631.
49 X. Lu and W. K. Olson, *Nucleic Acids Res*., 2003, **31**, 5108–5121.
50 B. Hess, C. Kutzner, D. van der Spoel and E. Lindahl, *J. Chem. Theor. Comput*., 2008, **4**, 435–447.
51 A. Vainrub and B. M. Pettitt, *Chem. Phys. Lett*., 2000, **323**, 160–166.
52 R. R. Johnson, A. T. C. Johnson and M. L. Klein, *Nano Lett*., 2008, **8**, 69–75.
53 K.-Y. Wong, A. Vainrub, T. Powdrill, M. Hogan and B. M. Pettitt, *Mol. Simul*., 2004, **30**, 121–129.
54 T. Špringer, H. Šípová, H. Vaisocherová, J. Štěpánek and J. Homola, *Nucleic Acids Res*., 2010, **38**, 7343–7351.
55 J. SantaLucia, *Proc. Natl. Acad. Sci. U. S. A*., 1998, **95**, 1460–1465.
56 Y. Gao, L. K. Wolf and R. M. Georgiadis, *Nucleic Acids Res*., 2006, **34**, 3370–3377.
57 A. W. Peterson, R. J. Heaton and R. M. Georgiadis, *Nucleic Acids Res*., 2001, **29**, 5163–5168.
58 S. He, B. Song, D. Li, C. Zhu, W. Qi, Y. Wen, L. Wang, S. Song, H. Fang and C. Fan, *Adv. Funct. Mater*., 2010, **20**, 453–459.
59 W. A. Steele, *J. Phys. Chem*., 1978, **82**, 817–821.
60 C. F. Edman, D. E. Raymond, D. J. Wu, E. Tu, R. G. Sosnowski, W. F. Butler, M. Nerenberg and M. J. Heller, *Nucleic Acids Res*., 1997, **25**, 4907–4914.

[OK3]

Dorčák V., Kabeláč M., **Kroutil O.**, Bednářová K. and Vacek J.

Electrocatalytic Monitoring of Peptidic Proton-Wires

Manuscript accepted in Analyst, (2016)

[IF(2014) = 4.107]

Participation of Ondřej Kroutil:

OK participated in the paper writing.

Electrocatalytic Monitoring of Peptidic Proton-Wires. Dorčák V., Kabeláč M., Kroutil O., Bednářová K. and Vacek J. Analyst, 2016

DOI: 10.1039/C6AN00869K. Reproduced from [OK3] with permission from the Royal Society of Chemistry.

Analyst

COMMUNICATION

View Article Online
View Journal

Electrocatalytic monitoring of peptidic proton-wires†

Cite this: DOI: 10.1039/c6an00869k

Received 14th April 2016,
Accepted 14th June 2016

DOI: 10.1039/c6an00869k

www.rsc.org/analyst

V. Dorčák,[a] M. Kabeláč,[b] O. Kroutil,[c] K. Bednářová[a] and J. Vacek*[d]

The transfer of protons or proton donor/acceptor abilities is an important phenomenon in many biomolecular systems. One example is the recently proposed peptidic proton-wires (H-wires), but the ability of these His-containing peptides to transfer protons has only been studied at the theoretical level so far. Here, for the first time the proton transfer ability of peptidic H-wires is examined experimentally in an adsorbed state using an approach based on a label-free electrocatalytic reaction. The experimental findings are complemented by theoretical calculations at the *ab initio* level in a vacuum and in an implicit solvent. Experimental and theoretical results indicated $Ala_3(His–Ala_2)_6$ to be a high proton-affinity peptidic H-wire model. The methodology presented here could be used for the further investigation of the proton-exchange chemistry of other biologically or technologically important macromolecules.

The exchange or transfer of protons is important for many biochemical processes including the respiratory chain, photosynthesis and enzyme catalysis. In proteins, proton transfer and proton binding affinities determine the charge and structure of their molecules, and thus have a large impact on their functioning and interactions with other molecules.[1]

A highly important phenomenon is the regulation of the function of some proteins by proton translocation, *e.g.* using the so-called proton-wires (H-wires) formed by water molecules captured in the channels localized within protein structures.[2–4] They can be found in green fluorescent proteins,[5] microbial rhodopsins,[6] gramicidin,[7] carbonic anhydrase,[5,8] or ribosomal complexes.[9] The mechanism of proton transport in such channels is based on proton diffusion through the hydrogen bond network of water molecules (the Grotthuss mechanism) followed by proton exchange with amino acid (aa) residues; very often His.[5]

In addition to the water H-wires in proteins, helical peptidic H-wires have also been proposed recently.[10] The ability of these 21-mer His-rich peptides to accept a proton and transfer it *via* the His residues distributed along the peptide backbone was proposed only at a theoretical level. To the best of our knowledge, such proton binding and translocation events were investigated using only the tools of computational chemistry.[10] In general, there is a lack of experimental approaches for the study of proton transfer or proton intramolecular movement in peptidic structures.

Here we focused on peptidic H-wires composed of His (H) and Ala (A) residues alone as follows: $A_3[HA_2]_6$ (HA2), $A_2[HA_3]_4HA_2$ (HA3), and $A_2[HA_4]_3HA_3$ (HA4).[10] Their proton transfer abilities were examined experimentally for the first time *via* an approach based on the electrochemical investigation of their activity in the catalytic hydrogen evolution reaction (CHER) at a Hg-electrode. An essential part of the electrode process is a catalytic cycle (reactions (1) & (2), Scheme 1A) in which the transfer of protons from the acid constituent of a solution (BH, H^+ donor) onto the electrode

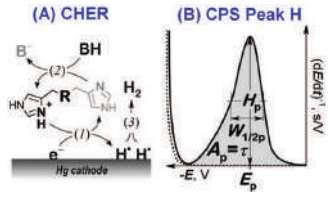

Scheme 1 (A) The catalytic hydrogen evolution reaction (CHER) of a His-containing catalyst. Catalyst deprotonation (1) reprotonation/regeneration (2), and formation of molecular/gaseous hydrogen (3) are highlighted. BH: the acid component of the supporting electrolyte. (B) CPS peak H due to the CHER resulting from derivation of the measured *E*–*t* curve (raw data) to facilitate its evaluation.

[a]*Institute of Biophysics of the CAS, v.v.i., Kralovopolska 135, 612 65 Brno, Czech Republic*
[b]*Department of Chemistry, Faculty of Science, University of South Bohemia, Branisovska 31, 370 05 Ceske Budejovice, Czech Republic*
[c]*Institute of Physics and Biophysics, Faculty of Science, University of South Bohemia, Branisovska 1760, 370 05 Ceske Budejovice, Czech Republic*
[d]*Department of Medical Chemistry and Biochemistry, Faculty of Medicine and Dentistry, Palacky University, Hnevotinska 3, 775 15 Olomouc, Czech Republic. E-mail: jan.vacek@upol.cz; Fax: +420 585632302; Tel: +420 585632303*

†Electronic supplementary information (ESI) available: Section 1, details of electrochemical experiments, section 2, *in silico* methods, section 3, CD spectroscopy analyses. See DOI: 10.1039/c6an00869k

surface (H^+ acceptor) is mediated by the His-containing catalyst adsorbed onto the electrode surface. The surface-bound hydrogen atoms then combine into more stable molecules of gaseous hydrogen, H_2 (reaction (3), Scheme 1A). The consumption of electrons, accompanying the transfer of protons, is reflected in the so-called peak H (Scheme 1B) at highly negative potentials as a typical analytical output when constant-current chronopotentiometric stripping (CPS) is used.[11]

Usually, both an increase in the CPS peak H area A_p (corresponding to the transition time τ) and a shift in its potential E_p towards less negative values suggest a more effective mediation of the proton transfer. In CHER, only aa residues with functional groups bearing exchangeable protons can be involved, *i.e.* only imidazolium groups of His residues in peptidic H-wires can participate in the transfer of protons reflected by the CPS peak H.[12–14] We applied the above-described methodology to study the proton transfer ability of H-wires HA2, HA3 and HA4.

At first, the H-wires were analyzed on the basis of the CPS peak H at a hanging mercury drop electrode (HMDE) in three different media. Initially, the peptides were accumulated on the electrode surface at an applied (accumulation) potential (E_A) of +0.1 V from unstirred solutions at a concentration of 1 μM. After 60 s of accumulation time (t_A), the electrode with adsorbed H-wire molecules was polarized by a cathodic (stripping) current (I_{str}) of −5 μA to reach highly negative potentials of around −2.0 V, where peak H was recorded. Other details of the electrochemical measurements are provided in section 1 of the ESI.†

Well-developed and much higher peaks were obtained under buffered conditions, while more than 1000-fold smaller peaks were produced in unbuffered solution (Fig. 1). Buffered medium, providing an excess of slightly acidic H^+ donors, is thus necessary for immediate reprotonation/regeneration of the catalyst in its adsorbed state from the bulk to close/form the catalytic cycle in CHER[13] (Scheme 1A).

In the buffered media, the biggest peak H at the least negative potential (E_p of −1.8 V) was produced by peptide HA2. The peptides HA3 and HA4 gave smaller responses at significantly more negative potentials (Fig. 1B and C). This finding indicates that HA2 is an effective proton transporter, which is in agreement with the previously reported computational results.[10] However, in contrast to our results, the theoretical investigation showed HA3 to be a more effective proton transporter than HA4. To interpret the theoretical *vs.* experimental differences in HA3 and HA4 proton transfer efficacy, it should be taken into account that proton transfer for H-wires in the form of an adsorbed layer at the Hg-surface is detected by CPS. In this way, protons can be transported *via* various mechanisms, including intermolecular and cooperative transfer effects, in comparison to the idealistic theoretical setup based on proton intramolecular translocation as reported in the literature.[10]

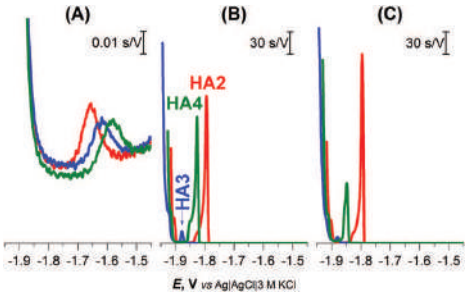

Fig. 1 CPS peaks H of 1 μM HA2, HA3, and HA4 at HMDE in (A) 0.1 M NaCl, pH 5.5, (B) 0.1 M Na-phosphate buffer, pH 7 and (C) McIlvaine buffer of pH 7, an I_{str} of −5 μA.

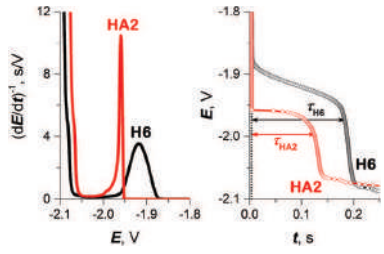

Fig. 2 CPS peaks H (left) and their corresponding E–t curves (right) of 10 μM HA2 and H6 at HMDE in 50 mM Na-phosphate buffer of pH 7, an I_{str} of −50 μA.

As a result, in subsequent experimental work we focused primarily on investigating HA2 together with the H6 peptide, which served as a positive control. H6 was chosen as the control because it contains six His residues, like HA2. The CPS peaks H of both peptides, including the original E–t curves, are shown in Fig. 2.

To obtain more reliable data for comparing the proton transfer in HA2 and H6, we measured their CPS responses under conditions suggesting full electrode coverage, *i.e.* at 10 μM or higher concentration (Fig. S1 in ESI†). Thus, the surface concentration of the catalyst was kept constant in the subsequent experiments, while the effect of pH on the CPS responses of HA2 and H6 was investigated. With decreasing pH-value, both the extent of peptide protonation and the proton donor concentration in the solution increased. As a result, an increase in the peak H area (A_p) and height (H_p) of both peptides was observed with decreasing pH from 7.5 to 6.3, and between pH 6.3 and 5.6 it changed only a little (Fig. 3). The pH-value of this break (6.3) is very close to the pK_a value of the His imidazolium group, *i.e.* ~6.1.[15]

It was recently shown using several model proteins that I_{str} is a driving parameter affecting their interfacial behavior and structural integrity during a CPS scan. Thus, we increased cathodic I_{str} intensity to avoid (i) reorientation of the catalyst molecules during the electrode process,[16] and (ii) disruption of the catalyst structural features upon exposure to highly negative electrode potentials.[17]

We can conclude that at $-I_{str}$ higher than 95 μA, both of the above effects were eliminated (Fig. 4 and S2 in ESI†). Between 35 and 95 μA, an S-shaped transition can be observed with HA2.

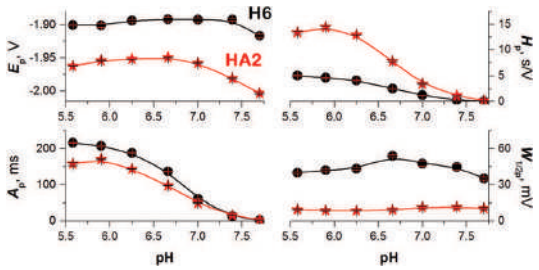

Fig. 3 Dependences of 10 μM HA2 (asterisk) and H6 (circle) peak H potential (E_p), area (A_p), height (H_p), and half-width ($W_{1/2p}$) on the pH-value of 50 mM Na-phosphate buffer at an I_{str} of −50 μA. Data are represented as means ± SD of four measurements. Error bars smaller than the plotted symbols are not visible.

This transition most likely reflects interfacial structural changes, *i.e.* distortion in HA2's structure, which is in agreement with previously reported studies,[16–19] especially the study where bovine serum albumin was investigated under practically the same experimental conditions.[17] At $-I_{str}$ lower than 35 μA, the prolonged exposure of HA2 molecules in the adsorbed layer to negative potentials could lead to complete structure destabilization, *i.e.* unfolding. The unfolding is due to electrostatic and hydrophobic interactions with the highly negatively charged electrode surface. This most likely results in the disruption of hydrogen bonds, the predominant stabilizing element of HA2's structure. The unfolded structures give higher electrochemical responses (expressed as $I_{str}\tau^{1/2}$ in Fig. 4) than the folded ones, because of the higher accessibility of the electrocatalytically active sites of HA2 to the electrode surface. In this way unfolded HA2 is involved in CHER more easily than the compact folded HA2 configuration. Similar examples and interpretations of electric field-induced destabilization of biomacromolecular structures (polypeptides and nucleic acids) can be found in the ref. 11 and 20.

The typical S-shaped transition was not observed with H6, since it has the structure of a random coil (see below Fig. 5B and 6). The typical CPS responses of HA2 and H6 acquired at an I_{str} of −150 μA are shown in the inset of Fig. 4.

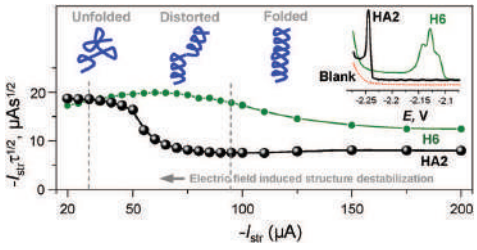

Fig. 4 Dependence of the $I_{str}\tau^{1/2}$ values of HA2 and H6 on an I_{str} at a 50 mM concentration of Na-phosphate buffer solution of pH 6. Inset: peak H of HA2 and H6 at an I_{str} of −150 μA. For other details, see Fig. S2 in the ESI.† The depictions of peptide structures here are only schematic and not to scale.

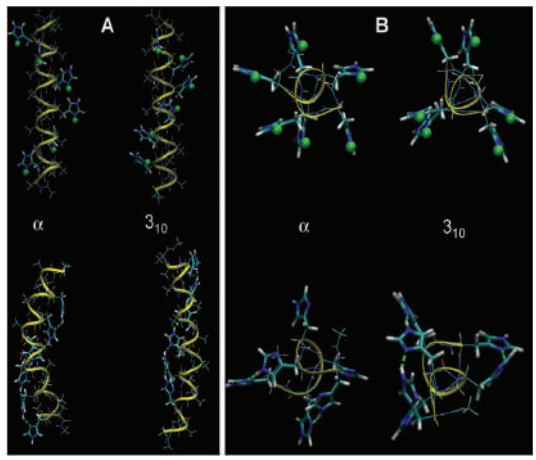

Fig. 5 Optimized α- and 3_{10}-structures of HA2 (A) and H6 random coil (B) in a fully protonated (top) and unprotonated (below) state using water as a solvent. Protons bound to His residues are highlighted as green spheres. The structures calculated in a vacuum are shown in Fig. S3 in the ESI.†

On the basis of our experimental data, the proton transfer mechanism of HA2 is different from that of H6. It is evident that both peptides have high proton transfer ability. HA3 and HA4 did not give a CPS response under the experimental conditions used (Fig. 4, inset). This result confirmed that HA2 is a more effective proton transporter than HA3 and HA4, not only under the initial experimental conditions (Fig. 1B and C) but also under the optimized conditions excluding the inevitable effects attributed to the specific interfacial behavior and structural distortion of adsorbed peptidic H-wires at the negatively charged electrode surface.

An important aspect in the further interpretation of both the experimental and theoretical data presented here is the knowledge of the structure of both peptides. Accordingly, we performed a calculation of the helical structures with all His residues protonated in a vacuum and in an implicit water environment. The 3_{10}-helix and α-helix configurations were taken into account, as reported previously.[10] With unprotonated polypeptides, the α-helical structure is more stable than the 3_{10}-one (by 19 kJ mol^{-1} in a vacuum and 49 kJ mol^{-1} in water). This is probably connected to the strong ability of Ala

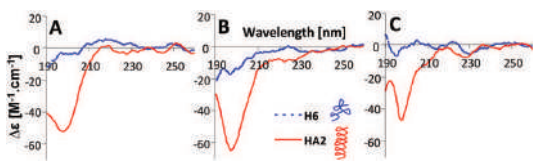

Fig. 6 CD spectra of 10 μM HA2 and H6 in 50 mM Na-phosphate buffer at (A) pH 6, (B) pH 7 and (C) pH 8. The depictions of peptide structures are only schematic and not to scale.

Table 1 Proton affinity calculated as difference between averaged energy of all optimized protonated systems and optimized neutral systems in kJ mol^{-1}. The deformation energy is included

	Proton affinity
Vacuum	
H6-3_{10}	937.0
H6-α	940.9
HA2-3_{10}	1112.5
HA2-α	1099.7
Water	
H6-3_{10}	1682.7
H6-α	1694.1
HA2-3_{10}	1718.6
HA2-α	1714.3

residues to form the α-helix. Optimized conformations of HA2 and H6 at fully protonated or unprotonated states in an aqueous environment are shown in Fig. 5. The calculated structures indicate that the state of protonation has a smaller impact on the structure for the HA2 peptide than for the H6 random coil peptide.

The proton affinity was calculated by computing the energy difference between the optimized unprotonated molecule and the fully protonated molecule (Table 1). The protonation energies are comparable for the different conformations. However, the HA2 peptide has a slightly higher proton affinity than H6 in water (by 30 kJ mol^{-1}), in a vacuum the difference is substantial (170 kJ mol^{-1}). Details of the calculated structures for HA2 and H6 can be found in section 2 in the ESI.†

In the next part of the experimental work, the structures of HA2 and H6 were investigated by circular dichroism (CD) spectroscopy under the same experimental conditions as for CPS measurement; for details see section 3 in the ESI.† HA2 exhibited a strong negative band near 200 nm, revealing that ordered structures are present (Fig. 6).[21] The CD spectrum of H6 exhibited only a low molar ellipticity in the examined pH-range, indicating a random coil organization with no dominating organized structure. It is evident that HA2 has a compact structure compared to the H6, with no periodicity in its structure.

In conclusion, further application of the electrocatalytic assay presented in this communication could provide new knowledge in the field of protonation equilibria and proton transfer in peptides. The experimental data are supported by *ab initio* calculations and CD spectroscopy of peptidic H-wires at different pH levels. Both our experimental data and calculated proton affinities indicate that HA2 is an effective molecule that can be used as a model for both experimental and theoretical investigations in the future. The proposed methodology is not only able to recognize protonated *vs.* unprotonated states (static parameter) but also to assess the proton transfer ability (dynamic parameter) in peptidic H-wires *via* CPS peak H characteristics, as specified in Scheme 1B. In terms of the mechanistic elucidation focused on the proton transfer process, the goal of further experimental work will be the self-assembled organization of peptidic H-wires onto the electrode surface,[22,23] which could enable us to also investigate a mechanism of proton movement in more detail.

This work was supported by the Czech Science Foundation (14-08032S, 13-08651S and P205/12/0466), by the MEYS of the Czech Republic/COST Action BM1203 (project no. LD14033) and by the CAS (RVO 68081707). The access to computing and storage facilities owned by parties and projects contributing to the National Grid Infrastructure MetaCentrum, provided under the programme "Projects of Large Infrastructure for Research, Development, and Innovations" (LM2010005) is highly appreciated.

Notes and references

1 V. R. I. Kaila, M. Wikstrom and G. Hummer, *Proc. Natl. Acad. Sci. U. S. A.*, 2014, **111**, 6988–6993.
2 E. Meyer, *Protein Sci.*, 1992, **1**, 1543–1562.
3 A. Migliore, N. F. Polizzi, M. J. Therien and D. N. Beratan, *Chem. Rev.*, 2014, **114**, 3381–3465.
4 G. M. Ullmann and E. Bombarda, *Biol. Chem.*, 2013, **394**, 611–619.
5 A. Shinobu and N. Agmon, *J. Phys. Chem. A*, 2009, **113**, 7253–7266.
6 K. Gerwert, E. Freier and S. Wolf, *Biochim. Biophys. Acta, Bioenerg.*, 2014, **1837**, 606–613.
7 R. Pomes and B. Roux, *Biophys. J.*, 1996, **71**, 19–39.
8 Q. Cui and M. Karplus, *J. Phys. Chem. B*, 2003, **107**, 1071–1078.
9 Y. S. Polikanov, T. A. Steitz and C. A. Innis, *Nat. Struct. Mol. Biol.*, 2014, **21**, 787–793.
10 G. E. Lopez, I. Colon-Diaz, A. Cruz, S. Ghosh, S. B. Nicholls, U. Viswanathan, J. A. Hardy and S. M. Auerbach, *J. Phys. Chem. A*, 2012, **116**, 1283–1288.
11 E. Palecek, J. Tkac, M. Bartosik, T. Bertok, V. Ostatna and J. Palecek, *Chem. Rev.*, 2015, **115**, 2045–2108.
12 V. Dorcak, V. Ostatna and E. Palecek, *Electrochem. Commun.*, 2013, **31**, 80–83.
13 V. Dorcak, V. Vargova, V. Ostatna and E. Palecek, *Electroanalysis*, 2015, **27**, 910–916.
14 V. Vargova, M. Zivanovic, V. Dorcak, E. Palecek and V. Ostatna, *Electroanalysis*, 2013, **25**, 2130–2135.
15 *CRC Handbook of Chemistry and Physics*, CRC Press, Boca Raton, Florida, 66th edn, 1985.
16 V. Dorcak, M. Bartosik, V. Ostatna, E. Palecek and M. Heyrovsky, *Electroanalysis*, 2009, **21**, 662–665.
17 H. Cernocka, V. Ostatna and E. Palecek, *Electrochim. Acta*, 2015, **174**, 356–360.
18 V. Ostatna, H. Cernocka and E. Palecek, *J. Am. Chem. Soc.*, 2010, **132**, 9408–9413.
19 E. Palecek, V. Ostatna, H. Cernocka, A. C. Joerger and A. R. Fersht, *J. Am. Chem. Soc.*, 2011, **133**, 7190–7196.
20 E. Palecek and M. Bartosik, *Chem. Rev.*, 2012, **112**, 3427–3481.
21 N. J. Greenfield, *Nat. Protoc.*, 2006, **1**, 2876–2890.
22 J. J. Gooding and N. Darwish, *Chem. Rec.*, 2012, **12**, 92–105.
23 B. J. Pepe-Mooney and R. Fairman, *Curr. Opin. Struct. Biol.*, 2009, **19**, 483–494.

[OK4]

Kroutil O., Minofar B. and Kabeláč M.

Structure and Dynamics of Solvated Hydrogenoxalate and Oxalate Anions: a Theoretical Study

Manuscript

Participation of Ondřej Kroutil:

OK prepared all models, performed all ab initio molecular dynamics simulations and did several analyses. He participated in the paper writing.

Structure and Dynamics of Solvated Hydrogenoxalate and Oxalate Anions: a Theoretical Study

Ondřej Kroutil, [1,2] Babak Minofar[1,3] and Martin Kabeláč[*,1]

[1] Faculty of Science, University of South Bohemia, Branišovská 31, 370 05, České Budějovice, Czech Republic

[2] Faculty of Health and Social Studies, University of South Bohemia, J. Boreckého 27, 370 11, České Budějovice, Czech Republic

[3] Center for Nanobiology and Structural Biology, Institute of Microbiology, Academy of Sciences of the Czech Republic, Zámek 136, 373 33, Nové Hrady, Czech Republic

* e-mail: mkabelac@prf.jcu.cz

Abstract:

Hydrogenoxalate (charge -1) and oxalate (charge -2) anions and their solvated forms were studied by various computational techniques. Ab initio quantum chemical calculations in gas phase, in implicit solvent and microsolvated (up to 32 water molecules) environment were performed in order to explore a potential energy surface of both anions. The solvation envelope of water molecules around them and the role of water on the conformation of the anions was revealed by means of Born–Oppenheimer molecular dynamics simulations and optimization procedures. The structure of the anions was found to be dependent on the number of water molecules in the solvation shell. A subtle interplay between intramolecular and intermolecular hydrogen bonding dictates the final conformation and thus an explicit solvent model is necessary for a proper description of this phenomena.

Keywords

oxalic acid anions, solvation, ab initio molecular dynamics, potential energy surface

1 Introduction

Understanding the structure and dynamic behavior of organic compounds covering the effect of surrounding (i.e. solvent and ions) is important for environmental chemistry, catalysis and biological chemistry [1]. It is well known that a solvation process can influence not only the physicochemical properties of the given compound, but also the attributes of the solvent such as surface tension and other colligative properties in the solutions. From this point of view organic acids and in particular dicarboxylic acids belong to an interesting group of compounds where mixing of hydrophobic properties of the backbone and hydrophilic properties of the carboxyl group(s) can influence solvation and solvent properties significantly.

Dicarboxylic acids can exist in two forms - either as unionized acids or as their salts. They appear in nature as a product of photooxidation of volatile organic compounds [2], they can be found in ambient atmosphere, in rainwater and aerosols. An important role of them as cloud condensation nuclei in the atmosphere and their influence on the physicochemical properties of tropospheric organic aerosols has been investigated [3]. They can stick to clay minerals such as kaolinite, montmorillonite [4] and, reversely, they can easily release from them to natural waters and soil. They decrease the surface tension of aqueous solutions and show surface propensity to the air/water interface in aqueous solutions [5–8].

The smallest of the dicarboxylic acids, oxalic acid ($H_2C_2O_4$), attracts the largest attention. It occurs in nature as a calcium oxalate mineral (whewellite, weddellite). It has been spotted in traces in atmosphere as a product of the combustion of fossil fuels, biomass burning, and exhaust of cars, representing 37–69% of the total dicarboxylic acids in atmosphere [9]. It also shows a wide biological activity in plants and animals. Tran *et al.* studied the production of oxalic acid by treatment of *Arabidopsis thaliana* plant with ozone. They revealed that oxalic acid induces activation of anion channels triggering the depolarization of the cell [10]. Its function in a human body has been investigated by Weljie *et al.* [11]. The authors revealed that the oxalic acid and diacylglycerol metabolites in blood are quantitatively depleted under sleep-restricted conditions and restored after recovery of sleep. Its high solubility (143 g/L; due to its polarity and a formation of intra and intermolecular hydrogen bonds) and moderate dissociation constants allows to produce oxalate ion which can interact with calcium ion and thus it plays an important role in the formation of calcium-containing uroliths in human body [12].

The neutral oxalic acid has been a subject of many experimental and theoretical studies. Mohajeri *et al*. [13] employing the second-order Møller–Plesset (MP2) level of theory investigated conformational flexibility of this compound. The role of intramolecular hydrogen bonds in gas-phase acidity and stability was also revealed in this paper. Jedlovszky *et al.* using classical molecular dynamics (MD) computer simulations investigated the phase diagram of binary mixture of oxalic acid and water in different concentrations [14]. Buonaugurio *et al*. measured and calculated (by means of photoelectron spectroscopy and ab initio calculations) the adiabatic electron affinity and electron vertical detachment energy and revealed the effect of intra-molecular hydrogen bonds in this process [15]. Weber *et al.* studied theoretically the interaction of oxalic acid with water molecules in gas phase by employing density functional theory and MP2 method, calculating the geometries, relative energies and free energy changes of the clusters of oxalic acid with up to six water molecules. They showed that the clusters of microsolvated oxalic acid produce stable neutral systems in the early stage of the cluster formation where solvation of potential hydrated proton is insufficient and hydrogen bond network of water is poorly developed [16].

As well as neutral oxalic acid, bare oxalate dianion ($C_2O_4^{-2}$) and its salts were studied extensively. Free oxalate anion possess orthogonal (staggered) structure, whereas in the presence of water and ions the structures is somewhat twisted or even planar [17].

Wang *et al*. investigated the solvation of different dicarboxylate dianions in water clusters and aqueous slabs by photoelectron spectroscopy and molecular dynamics simulations. They revealed that the oxalate ion is solvated in the bulk, whereas the dicarboxylate dianion with hydrophobic groups possess the propensity to the aqueous solution/air interface [18, 19]. This finding agree with results of other MD simulations [20–22]. Several works focused on ion pairing with oxalate anion has been also published [23–26].

Compared to oxalic acid and oxalate dianion, hydrogen oxalate anion ($HC_2O_4^{-1}$) studies are presented sparsely. They are mainly focused on description of an intramolecular proton transfer [27–30]. To the best of our knowledge only a work of Mohajeri *et al*. [13] is dedicated to the microsolvation (up to 6 molecules of water) of this anion.

In this article we focus on both forms of oxalic acid anion, i.e. hydrogenoxalate anion and oxalate dianion. The reason to omit neutral oxalic acid is related to its strength (pKa_1 =1.24) and thus very low concentration of its non-dissociated form in near-neutral pH.

2 Computational Methods

Ab initio optimization procedures

Structure of the oxalate dianion (fully deprotonated, i.e. with net charge 2-) , abbreviated as *ox-2* in the text and hydrogenoxalate anion, (net charge -1, abbreviated as *ox-1*) were studied at various level of theory, including bare and hydrated ions using implicit water model as well as explicit water.

a) *Calculations in vacuum and implicit solvent*

The rotational barrier of *ox-2* O-C-C-O torsion angle and two-dimensional energy profile of *ox-1* O-C-C-O vs. H-O-C-C torsion angles at the relaxed potential energy surface were studied at the B3LYP/cc-pVTZ level of theory in vacuum and using PCM model of implicit water [31]. The missing dispersion term at the DFT level was added in the empirical way using Grimme's D3 correction [32].

The benchmark energy data were obtained for the B3LYP relaxed geometries at the CCSD(T) level employing the same basis set. Since it is believed that the basis set containing the diffusion functions can be important for the anionts, we recalculated the rotation barrier for the oxalate dianion in the same manner at CCSD(T) level employing also the daug-cc-pVTZ basis set. Only the energy differences between stationary points were reinvestigated employing this diffusion basis set for the hydrogenoxalate anion due to time demandingness of the calculations.

The time-consuming ab initio molecular dynamics simulations require the usage of the simpler form of the functional and medium-sized basis set (in order to speed-up the calculations), thus the torsion profiles were also recalculated using BLYP functional with D3 corrections and def2-SVP basis set in the same way as the benchmark cc-pVTZ data.

b) *Ab initio optimization of microsolvated clusters*

The initial geometries of clusters of oxalic acid anions, (i.e. *ox-1, ox-2*) containing 4, 8, 16 and 32 water molecules were obtained from four randomly chosen snapshots from respective ab initio MD simulations. For each structure the O-C-C-O torsion angle was set to 0, 45 and 90 degrees, producing thus three new geometries, which were after fully optimized. Harmonic

vibrational frequencies were calculated in order to characterize each of the stationary points. All these calculations were performed using the program Gaussian09 program package [33].

c) Ab initio molecular dynamics (AIMD) in periodic box

Periodic boundary conditions AIMD simulations based on Born-Oppenheimer approximation were carried on using a hybrid Gaussian plane-wave method (GPW) implemented in CP2K [34] software. Charge density cut-off of 400 Ry with NN50 smoothing was used in all simulations. This cut-off value represents finer grid than had been used in similar studies (250 Ry) [35, 36], thus the error in calculated energy should be low. Higher cut-off values would give practically the same results but with drastically increased computer power cost.

BLYP functional [37] with the empirical dispersion term [32] for the main group elements was used in conjunction with double-ξ molecularly optimized basis functions augmented by polarization function (DZVP) [38] and appropriate pseudopotential of Goedecker, Teter and Hutter (GTH) [39]. All hydrogens were replaced by deuterium to reduce quantum effects of the hydrogen nuclei and to increase the time step.

Each simulation box was composed of (hydrogen)oxalate anion and 50 heavy water (D_2O) molecules. Box dimensions were adjusted to match density of 1.01 $g.cm^{-3}$, resulting in cubic box of length of ~11.8 Å. The net charge of the system (-2 for oxalate dianion and -1 for hydrogenoxalate anion, respectively) was compensated by the neutralizing background charge.

For each ionic form of oxalic acid two simulations based on different initial conformations were carried out. For the hydrogenoxalate anion we selected two existing minima at the potential energy surface (PES) [13], *ox-1-closed* (planar structure, hydrogen atom pointing to the second carboxyl group) and *ox-1-open* (O-C-C-O value equal to 90 degrees, hydrogen pointing out of the molecule) with respective number of waters taken into account. See Figure 1 for above mentioned conformations.

We initiated our simulation from staggered geometry corresponding to the minimum at the PES and from the planar conformation (transition state at the PES) for *ox-2* system. Since the AIMD simulations provided identical results in range of RMSDs for both initial structures, the results will be discussed just once.

An equilibration phase consisted of two steps. Firstly, 500 ps classical MD simulation in NVT ensemble had been performed with frozen (hydrogen)oxalate ion. *Gaff* force field [40] with

partial charges derived by standard RESP procedure had been used both for anions and SPC/E model of water. A 200 fs AIMD pre-equilibrium simulation followed, with the same constrains preserved as in the previous step.

All subsequent production runs were carried out within NVT ensemble with a Nosé-Hoover thermostat (relaxation time 500 fs) and time step of 1 fs. A temperature was set to 300 K. Each trajectory was 30 ps long and the structures were saved each step. The first 5 ps of the trajectory was considered as an equilibration phase and it was not included in the analysis except for an investigation of the time evolution of dihedral angles. The trajectories were inspected using Gromacs analysis tools [41] and the VMD program [42] was used for their visualization.

d) *Ab initio molecular dynamics of microsolvated systems*

AIMD simulations of microsolvated system containing 4, 8, 16 and 32 water molecules were performed with the same settings and initial structures as it was mentioned in section c). The only difference was an absence of periodicity and usage of Martyna-Tuckerman Poisson's equations solver [43].

3 Results and discussion

a) Ab initio calculations in gas phase and implicit solvent

The O-C-C-O torsion profile of *ox-2* is depicted in Figure 2. The global minimum corresponds to the structure with carboxylate groups oriented perpendicularly to each other (staggered conformation). All our employed methods predict the energy barrier of the rotation in the gas phase in range between 3.8-4.9 kcal/mol, what is in a good agreement with findings from previously published data based on ab initio methods) [44–46] (2 - 6 kcal/mol) and with results from umbrella sampling classical MD simulations [24] (3.6 kcal/mol).

The CCSD(T) energy dependence based on B3LYP/cc-pVTZ geometries is almost identical with the B3LYP one, the rotational barriers differs only by 0.1 kcal. No significant improvement of the results was observed when a large diffusive daug-cc-pVTZ basis set was used, the barrier height was found only by 0.38 kcal/mol higher in comparison with the results when the cc-pVTZ basis set was employed.

The computationally inexpensive BLYP functional and def2-SVP basis set provides a satisfactory consistency with benchmark CCSD(T) data, since the barrier height is underestimated only by 0.8 kcal/mol. Together with the ability of this functional to describe correctly the behavior of bulk water [47, 48] it justifies the choice of this functional and this basis set as an economical tool for our ab initio molecular dynamics simulations.

When the system was placed into the implicit solvent, the barrier was lowered in all methods systematically by about 1.5 kcal/mol, resulting to its value of 2.8 kcal/mol for the CCSD(T)level.

There are two minima at the potential energy surface of *ox-1* anion. The global minimum corresponds to the planar structure (see Figure 1, *ox-1-closed*) with a weak intramolecular OH...O hydrogen bond [28, 29]. The local minimum *ox-1-open* (See Figure 1, *ox-1-open*) is far less stable (by 10 kcal/mol) and it contains perpendicularly oriented carboxylic groups and the hydroxyl group rotated by 180 degrees.

The 2D-relaxed scan of the energy dependence of O-C-C-O *vs.* H-O-O-C torsion angles for the *ox-1* was performed using the same technique as in the case of *ox-2*. The results are depicted in Figure 3. The rotation around the C-C bond is hindered due to the presence of hydrogen bond and the energy barrier is higher by 6 kcal/mol (i.e. it reaches the value of 10.2 kcal/mol) in comparison with the *ox-2*. No such hindrance occurs for the local minimum, where the barrier remains similar as in the case of *ox-2*.

The rotation of OH group is blocked completely, since the barrier reaches the value of 21.4 kcal/mol. Results of all methods are in good agreement, even the BLYP functional predicts the barriers only slightly higher; by 1.6, resp. 2.5 kcal/mol than the other methods. The gain of the employment of usage of daug-cc-pVTZ basis set for this system is again weak since the discrepancy in comparison with data obtained by cc-pVTZ basis set did not exceed 0.5 kcal/mol for all stationary points at the potential energy surface.

The implicit solvent again systematically diminishes the barriers, between 3.1 - 3.9 kcal/mol without other important changes at the PES.

b) AIMD and optimizations in explicit solvent

All bond lengths and valence angles of *ox-2 and ox-1* obtained both from optimization and from the ab initio dynamics are in good agreement with the literature data available [13, 29, 30, 46, 49,

50] and do not differ more than 0.06 Å, resp. 15 degrees from each other, see Table S1 in the Supplementary information part. The biggest discrepancies were found in the *ox-1-closed* structure due to change of its geometry (see below).

The crucial geometrical parameter of oxalic acid is its O-C-C-O dihedral angle which deserves a detailed analysis, separately for both ionic forms.

Ox-2 system. The AIMD simulations of *ox-2* in periodic box consisting of 50 molecules of water as well as AIMD of microsolvated systems show a clear preference of the nearly staggered form of *ox-2*, nevertheless whether the AIMD run started from planar or staggered structure. When a planar form was used, the O-C-C-O dihedral changed gradually approximately during 3 ps to values close to 90 degrees in all simulations, no matter how many water molecules was used to solvate the system and retained close to this value for the rest of the simulations, see Figure 4 for further details. The effect of the increasing number of solvent molecules on lowering of the energy barrier is evident, since an occasional full rotation around C-C bond in the periodical system was observed (approx. every 12 ps). The average value of the dihedral angle is deviated from the ideal value of 90 degrees and it reaches values 77.5 ± 8.4, 77.1 ± 9.0, 66.7 ± 10.1, 76.0 ± 10.6, 75.5 ± 10.6 and 70.9 ± 17.9 for gas phase, microsolvation with 4, 8, 16 and 32 water molecules and periodic systems, respectively. Such a conformation allows to create the most favorable network of H-bonds in the system. This finding was confirmed by the optimization procedure and by the literature data available. Rosas-García *et al.* [50] found O-C-C-O dihedral angle equal to 78° for the microsolvated system with 14 water molecules, Gao's *et al.* [49] computed values were in range from 81 to 88° on B3LYP/6-31+G** level when 12 water molecules were included. The histogram profile of the torsion angle for the simulation in the periodic box is depicted in Figure 5, showing that the thermal movement allows a broader fluctuation of the dihedral angle and thus the higher flexibility of the system.

The results obtained from the optimization procedure (see Table 1) have rather qualitative character since the conformational search at the PES of microsolvated complexes was not performed due to extreme complexity and flatness of the potential energy surface and since the structures selected for the optimization were based on the random choice. Nevertheless, we can conclude that water diminishes the energy difference between the staggered and planar conformations, in agreement with the findings from AIMD and the calculations in implicit solvent. The values of the dihedral angle in the optimized structures agree well with its average

value obtained from the AIMD. The role of the entropy is rather weak since the differences between relative electronic energies and Gibbs free energies are very similar and they do not differ more than 1 kcal/mol. When the number of water molecules is doubled, the solvent-solute interaction energy is raised by approx. 50 kcal/mol. The values of interaction energy for the anion surrounded by 4 or 8 water molecules are in agreement with available literature data [50].

Ox-1 system. Whereas the initio optimizations in the gas phase and implicit solvent predict the planar geometry as the most stable one, from the AIMD in explicit solvent it is evident that the preferred geometry of *ox-1-closed* system is dependent on the number of water molecules. During the first two ps of the AIMD simulation in the periodic box the intramolecular H-bond in this structure was disrupted, the planar conformation changed to staggered one and the O-C-C-O torsion angle begun fluctuating around the value of 70° (Figure 6) for approx. 20 ps. In the next 3 ps the structure gradually changed back close to its initial planar conformation in which it more or less remains for the rest of the simulation. This indicates that the energy difference between planar and staggered geometry is significantly lower in explicit solvent than in gas phase, as it is predicted by the calculations in the implicit solvent. The histogram profile of the torsion angle for the simulation in the periodic box is depicted in Figure 5.

Similarly as for *ox-2* we conducted also AIMD in the gas phase and in the microsolvated environment (Figure 6) for *ox-1-closed* structure. The system maintains its initial planar structure in the gas phase and in the system with up to 8 water molecules for whole time of the simulation. A sudden oscillation of the O-C-C-O dihedral in time of ~19.5 ps of gas phase trajectory is associated with the intramolecular proton transfer where the molecule started swinging for 3 ps and after than the dihedral angle returned back to its common value. No proton transfer was observed in microsolvated systems on time scale used in AIMD.

The complete first hydration shell (14 water molecules [50]) of *ox-1* seems to be sufficient to change the preferred conformation from planar to staggered one. The O-C-C-O dihedral oscillates between average value of 70.7° and 60.5° for systems containing 16 and 32 water molecules, similarly as it was observed in the simulation in the periodic environment. Generally, the change from planar to staggered form is caused by formation of strong hydrogen bond between hydrogen of *ox-1* and oxygen of incoming water molecule, showing a preference of the

intermolecular over the intramolecular H-bond. A short time existing bifurcated hydrogen bond on hydrogen atom of *ox-1* is an intermediate of this process.

Ab initio optimizations (see Table 2) also confirm a decrease of difference between planar and staggered structure when number of water molecules is increased, however planar conformations remains global minima regardless of size of the of solvation envelope. The interaction energies between solvent and solute are ca. 55% of those of water - *ox-2* systems due to smaller charge of the anion and thus weaker Coulombic forces between the anion and water.

We also performed an AIMD in periodic water box for the *ox-1-open* structure, which is a local minimum at the PES in the gas phase. The dependence of the O-C-C-O torsion angle more resembles the profile of *ox-2,* with even higher variability in its values (Figure 5). The anion in *open* conformation seems to be better hydrated than in the *closed* form (the hydration energies are systematically by 5 kcal/mol more negative) and in vacuum disfavored *open* conformation in the presence of 32 water molecules became a global minimum at the PES. Similar discrepancy between stability of the closed and open structure in implicit solvent and explicit water was found for pyruvic acid [51]. However, the transition between *open* and *closed* conformation has never been observed in AIMD (Figure S1) signaling that the H-O-O-C barrier remains still too high to be overcame at the room temperature even in the presence of the solvent.

Solvation shell properties. Firstly, to prove reliability of used combination of the DFT functional and basis set we plotted the radial distribution function (RDF) between all water oxygens in the system (Figure 7a). One can notice a good agreement between experimental neutron diffraction data and our simulations both for *ox-1* and *ox-2* systems. A calculated running coordination number (RCN) around water molecules (Figure S2) is 4.80, which falls into range of values computed for the neat water in previous studies (4.17 for BLYP and 4.91 for BLYP-D2) [47].

All oxygens (Ox) are equal in *ox-2* molecule due to the system symmetry and thus the Ox-Ow RDF can be plotted for all Ox atoms (Figure 7b) at once. The RDF possess its first maximum at 2.75 Å. Very similar values were also found for acetate [35] and sulfate anion [36]. Further we observed a minimum in the distance of ~3.2 Å and the flat second maximum situated at ~ 4.8 Å in the RDF. Comparing the Ox-Ow and Ow-Ow RDFs we can see almost same localization of the first maximum, however the height and width of Ox-Ow peak is smaller due to absent

hydrogens in *ox-2,* resulting in inability of *ox-2* behaving as a proton donor. The running coordination number for the first peak corresponds to the value of ~2.5 (Figure S2) which is almost one half of the value in RCN in Ow-Ow.

The first peak in Ox-Hw RDF (Figure 7b) positioned at 1.75 Å belongs to the water hydrogen directly interacting with oxalate oxygens, whereas the second peak at 3.5 Å belongs to the second hydrogen of corresponding water molecule. The spatial distribution of water molecules around *ox-2* is depicted in Figure 8. One can notice almost symmetrically distributed lobes of higher water density, two around each Ox oxygen.

The O-Ow RDF of *ox-1* anion must be plotted separately for each of the oxygen atoms (for the atom names see Figure 1) of *ox-1.* O1-Ow RDF of *ox-1-closed* structure shows the first sharp peak at 2.6 Å (Figure 7c). It belongs to the water oxygen which is in the contact with the hydrogen H1 of the anion. This region is encircled and labeled as "1st O1-Ow" in the spatial distribution function (SDF) in Figure 8b. RCN of this peak is ~0.52 (Figure S2). The second well recognizable peak situated between 2.9 and 4.2 Å corresponds to tightly bonded water molecules around O1. Sharp-peaked RDF profile is inflicted by pointing of the H1 atom into the interior of the structure, letting carboxyl oxygens O1 and O2 to be more exposed to the solvent.

The O1-Ow RDF profile of *ox-1-open* structure is less developed except of the first peak. The hydrogen atom of *ox-1* is oriented out of the molecule thus the H-bond pattern is different from one in the *ox-1-closed* anion.

The first peak in O2-Ow RDF (Figure 7d) has its maximum at 2.9 Å and it is less pronounced for both conformations of *ox-1* in comparison with the remaining O-Ow RDFs. RCN ~1.9 of O2 oxygen is lower in comparison to O3/O4 oxygens (RCN ~2.5). This can be caused by a smaller polarity of a neutral COOH group in comparison with the charged COO^- group, lowering thus the attractive forces between the ion and the surrounding water molecules. The first peak is more blurred compared to RDF of *ox-1-closed*, probably due to flexible solvation shell. The *ox-1-closed* RDF contains the second sharp peak around 4.6 Å belonging to the water molecules interacting with O1, whereas this peak is missing in RDF of *ox-1-open* structure.

The RDF of oxygens O3 and O4 (Figure 7e) that belong to the charged carboxylate group of both conformers of *ox-1* is very similar to RDF of Ox-Ow of *ox-2* structure and the same finding is also valid for the comparison between O3+O4-Hw and Ox-Hw profiles.

O1-Hw RDF slightly differs between both *ox-1* conformers (Figure 7c). Whereas *ox-1-closed* RDF monotonously rises up to the first maximum at 3.1 Å, there is a small peak at 1.5 Å in the *ox-1-open* RDF. This peak corresponds to the water hydrogen bonded to the O1 of the *ox-1*. This region is encircled in corresponding SDF and named as "1st O1-Hw" (Figure 8c). The shape of the O2-Hw RDFs (Figure 7d) is similar for both *ox-1* structures with the first peak at 1.8 Å, which corresponds to hydrogen-bonded water molecules. This peak is lower in *ox-1-open* due to the steric hindrance of the hydroxyl group for incoming water molecules.

In order to retrieve an information about the number of water molecules accommodated in the first solvation shell, we also plotted the RDFs between centers-of-masses of the anions and water oxygens (Figure S3). All curves possess one distinct minimum around 5 Å. The corresponding RCN is equal to ~15 water molecules located in the first solvation shell, both for *ox-1* and *ox-2*. This finding is in accordance with work of Rosas-García et al. [50] who found 14 water molecules in the first solvation shell of ox-2 and in fairly good agreement with Gao et al. [49], who reported RCN = 12 for *ox-2*.

4. Conclusions

1. Our ab initio calculations have confirmed that the most stable conformation of *ox-2* both in gas phase and in the implicit solvent is the staggered D_{2d} form. Implicit water model systematically lowers all rotational barriers by 1.5- 3 kcal/mol.

2. AIMD calculations as well as the optimizations of solvated *ox-2* show that the rotational barrier around C-C bond can be relatively easily overestimated in the explicit solvent. The preferred conformation remains the staggered one, however with partial deviation (~20°) from the ideal value.

3. There are two minima on *ox-1* potential energy surface: The global minimum corresponds to the planar structure. The hydrogen of COOH group is involved in intramolecular hydrogen bond with neighboring COO^- group in this conformation. The structure of the local minimum was found in staggered geometry with hydrogen of COOH group pointing out of the oxalic acid. This conformation is far less stable in the gas phase and in the implicit solvent (by 10, resp. 7 kcal/mol) than the global minimum.

4. The AIMD of microsolvated *ox-1-closed* structure shows that the system with up to eight water molecules remains in the planar conformation, whereas in the presence of more water molecules and in the bulk the staggered conformation becomes more preferred. The rotation around C-C bond is almost free at the room temperature in the bulk. The distribution of O-C-C-O torsion angles during AIMD for the *ox-1-open* structure more resembles the profile of the *ox-2* system. The local minimum seems to be slightly better hydrated than the global one which helps to overcome its instability in the gas phase. These two conformers are more or less isoenergetical in the bulk. However, the barrier of rotation of hydroxyl group remains still too high to be overcame even in the solvent and the transition between the global and local minimum was never observed in our AIMD runs.

5. The solvation pattern around negatively charged carboxylate group is very similar both for *ox-1* and *ox-2* with approximately 2.5 water molecules around each oxygen. The COOH group solvation shell structure is dependent on the orientation of its hydrogen, as it can be deduced from the RDF profile. Number of water molecules in the first solvation shell (~15) was found to be the same for both *ox-1* and *ox-2* and in the agreement with previously reported data.

6. Finally, the implicit solvent is inadequate for the proper description of such charged systems with strong H-bond network around and a sufficient amount of water molecules or periodic boundary conditions should be applied for the studies of such compounds.

Acknowledgement

Authors were supported by the Czech Science Foundation Project 13-08651S. Computational resources were provided by the MetaCentrum under the program LM2010005 and the CERIT-SC under the program Centre CERIT Scientific Cloud, part of the Operational Program Research and Development for Innovations, Reg. CZ.1.05/3.2.00/08.0144.

References

1. Nandi N, Bhattacharyya K, Bagchi B (2000) Dielectric Relaxation and Solvation Dynamics of Water in Complex Chemical and Biological Systems. Chem Rev 100:2013–2046. doi: 10.1021/cr980127v

2. Ervens B, Feingold G, Frost GJ, Kreidenweis SM (2004) A modeling study of aqueous production of dicarboxylic acids: 1. Chemical pathways and speciated organic mass production. J Geophys Res Atmospheres 109:D15205. doi: 10.1029/2003JD004387

3. Kawamura K, Umemoto N, Mochida M, et al (2003) Water-soluble dicarboxylic acids in the tropospheric aerosols collected over east Asia and western North Pacific by ACE-Asia C-130 aircraft. J. Geophys. Res. Atmospheres 1984–2012 108:

4. Kong M, Huang L, Li L, et al (2014) Effects of oxalic and citric acids on three clay minerals after incubation. Appl Clay Sci 99:207–214. doi: 10.1016/j.clay.2014.06.035

5. Chebbi A, Carlier P (1996) Carboxylic acids in the troposphere, occurrence, sources, and sinks: A review. Atmos Environ 30:4233–4249. doi: 10.1016/1352-2310(96)00102-1

6. Mahiuddin S, Minofar B, Borah JM, et al (2008) Propensities of oxalic, citric, succinic, and maleic acids for the aqueous solution/vapour interface: Surface tension measurements and molecular dynamics simulations. Chem Phys Lett 462:217–221. doi: 10.1016/j.cplett.2008.07.085

7. Riipinen I, Koponen IK, Frank GP, et al (2007) Adipic and Malonic Acid Aqueous Solutions: Surface Tensions and Saturation Vapor Pressures. J Phys Chem A 111:12995–13002. doi: 10.1021/jp073731v

8. Topping DO, McFiggans GB, Kiss G, et al (2007) Surface tensions of multi-component mixed inorganic/organic aqueous systems of atmospheric significance: measurements, model predictions and importance for cloud activation predictions. Atmos Chem Phys 7:2371–2398. doi: 10.5194/acp-7-2371-2007

9. Kawamura K, Ikushima K (1993) Seasonal changes in the distribution of dicarboxylic acids in the urban atmosphere. Environ Sci Technol 27:2227–2235. doi: 10.1021/es00047a033

10. Tran D, Kadono T, Molas ML, et al (2013) A role for oxalic acid generation in ozone-induced signallization in Arabidopis cells. Plant Cell Environ 36:569–578. doi: 10.1111/j.1365-3040.2012.02596.x

11. Weljie AM, Meerlo P, Goel N, et al (2015) Oxalic acid and diacylglycerol 36:3 are cross-species markers of sleep debt. Proc Natl Acad Sci 112:2569–2574. doi: 10.1073/pnas.1417432112

12. Sharma S, Nath R, Thind SK (1993) Recent advances in measurement of oxalate in biological materials. Scanning Microsc 7:431–441.

13. Mohajeri A, Shakerin N (2004) The gas-phase acidity and intramolecular hydrogen bonding in oxalic acid. J Mol Struct THEOCHEM 711:167–172. doi: 10.1016/j.theochem.2004.10.002

14. Darvas M, Picaud S, Jedlovszky P (2011) Water adsorption around oxalic acid aggregates: a molecular dynamics simulation of water nucleation on organic aerosols. Phys Chem Chem Phys 13:19830–19839. doi: 10.1039/C1CP21901D

15. Buonaugurio A, Graham J, Buytendyk A, et al (2014) Communication: Remarkable electrophilicity of the oxalic acid monomer: an anion photoelectron spectroscopy and theoretical study. J Chem Phys 140:221103. doi: 10.1063/1.4882655

16. Weber KH, Morales FJ, Tao F-M (2012) Theoretical Study on the Structure and Stabilities of Molecular Clusters of Oxalic Acid with Water. J Phys Chem A 116:11601–11617. doi: 10.1021/jp308499f

17. Dean PAW (2012) The Oxalate Dianion, C2O42–: Planar or Nonplanar? J Chem Educ 89:417–418. doi: 10.1021/ed200202r

18. Minofar B, Vrbka L, Mucha M, et al (2005) Interior and Interfacial Aqueous Solvation of Benzene Dicarboxylate Dianions and Their Methylated Analogues: A Combined Molecular

Dynamics and Photoelectron Spectroscopy Study. J Phys Chem A 109:5042–5049. doi: 10.1021/jp050836u

19. Minofar B, Mucha M, Jungwirth P, et al (2004) Bulk versus Interfacial Aqueous Solvation of Dicarboxylate Dianions. J Am Chem Soc 126:11691–11698. doi: 10.1021/ja047493i

20. Liu Y, Minofar B, Desyaterik Y, et al (2011) Internal structure, hygroscopic and reactive properties of mixed sodium methanesulfonate-sodium chloride particles. Phys Chem Chem Phys 13:11846–11857. doi: 10.1039/C1CP20444K

21. Harper K, Minofar B, Sierra-Hernandez MR, et al (2009) Surface Residence and Uptake of Methyl Chloride and Methyl Alcohol at the Air/Water Interface Studied by Vibrational Sum Frequency Spectroscopy and Molecular Dynamics†. J Phys Chem A 113:2015–2024. doi: 10.1021/jp808630v

22. Chen X, Minofar B, Jungwirth P, Allen HC (2010) Interfacial Molecular Organization at Aqueous Solution Surfaces of Atmospherically Relevant Dimethyl Sulfoxide and Methanesulfonic Acid Using Sum Frequency Spectroscopy and Molecular Dynamics Simulation. J Phys Chem B 114:15546–15553. doi: 10.1021/jp1078339

23. Hind AR, Bhargava SK, Bronswijk WV, et al (1998) On the Aqueous Vibrational Spectra of Alkali Metal Oxalates. Appl Spectrosc 52:683–691. doi: 10.1366/0003702981944355

24. Kuroda DG, Hochstrasser RM (2011) Two-dimensional infrared spectral signature and hydration of the oxalate dianion. J Chem Phys 135:204502. doi: 10.1063/1.3658461

25. Kuroda DG, Hochstrasser RM (2012) Dynamic structures of aqueous oxalate and the effects of counterions seen by 2D IR. Phys Chem Chem Phys 14:6219–6224. doi: 10.1039/C2CP23892F

26. Buchner R, Samani F, May PM, et al (2003) Hydration and Ion Pairing in Aqueous Sodium Oxalate Solutions. ChemPhysChem 4:373–378. doi: 10.1002/cphc.200390064

27. Bosch E, Moreno M, Lluch JM, Bertrán J (1990) Bidimensional tunneling dynamics of malonaldehyde and hydrogenoxalate anion. A comparative study. J Chem Phys 93:5685–5692. doi: 10.1063/1.459562

28. Bosch E, Moreno M, Lluch JM (1992) The role of coupling in intramolecular proton transfer reactions. The hydrogen oxalate anion as an example. Can J Chem 70:100–106. doi: 10.1139/v92-017

29. Truong TN, McCammon JA (1991) Direct dynamics study of intramolecular proton transfer in hydrogenoxalate anion. J Am Chem Soc 113:7504–7508. doi: 10.1021/ja00020a009

30. Fernández-Ramos A, Rodríguez-Otero J, Ríos MA (1998) High Level and Dual Level Direct Dynamics in the Intramolecular Proton Transfer of Hydrogenoxalate Anion. Influence of Tunneling and Isotopic Effect. J Phys Chem A 102:2954–2961. doi: 10.1021/jp980269t

31. Scalmani G, Frisch MJ (2010) Continuous surface charge polarizable continuum models of solvation. I. General formalism. J Chem Phys 132:114110. doi: 10.1063/1.3359469

32. Grimme S, Antony J, Ehrlich S, Krieg H (2010) A consistent and accurate ab initio parametrization of density functional dispersion correction (DFT-D) for the 94 elements H-Pu. J Chem Phys 132:154104. doi: 10.1063/1.3382344

33. Frisch MJ, Trucks GW, Schlegel HB, et al (2009) Gaussian 09. Gaussian, Inc., Wallingford, CT, USA

34. Hutter J, Iannuzzi M, Schiffmann F, VandeVondele J (2013) cp2k: atomistic simulations of condensed matter systems. Wiley Interdiscip Rev Comput Mol Sci n/a-n/a. doi: 10.1002/wcms.1159

35. Kahlen J, Salimi L, Sulpizi M, et al (2014) Interaction of Charged Amino-Acid Side Chains with Ions: An Optimization Strategy for Classical Force Fields. J Phys Chem B 118:3960–3972. doi: 10.1021/jp412490c

36. Pegado L, Marsalek O, Jungwirth P, Wernersson E (2012) Solvation and ion-pairing properties of the aqueous sulfate anion: explicit versus effective electronic polarization. Phys Chem Chem Phys 14:10248–10257. doi: 10.1039/C2CP40711F

37. Lee C, Yang W, Parr RG (1988) Development of the Colle-Salvetti correlation-energy formula into a functional of the electron density. Phys Rev B 37:785–789. doi: 10.1103/PhysRevB.37.785

38. VandeVondele J, Hutter J (2007) Gaussian basis sets for accurate calculations on molecular systems in gas and condensed phases. J Chem Phys 127:114105. doi: 10.1063/1.2770708

39. Goedecker S, Teter M, Hutter J (1996) Separable dual-space Gaussian pseudopotentials. Phys Rev B 54:1703–1710. doi: 10.1103/PhysRevB.54.1703

40. Wang J, Wolf RM, Caldwell JW, et al (2004) Development and testing of a general amber force field. J Comput Chem 25:1157–1174. doi: 10.1002/jcc.20035

41. Hess B, Kutzner C, van der Spoel D, Lindahl E (2008) GROMACS 4: Algorithms for Highly Efficient, Load-Balanced, and Scalable Molecular Simulation. J Chem Theory Comput 4:435–447. doi: 10.1021/ct700301q

42. Humphrey W, Dalke A, Schulten K (1996) VMD: visual molecular dynamics. J Mol Graph 14:33–38, 27–28.

43. Martyna GJ, Tuckerman ME (1999) A reciprocal space based method for treating long range interactions in ab initio and force-field-based calculations in clusters. J Chem Phys 110:2810–2821. doi: 10.1063/1.477923

44. Dewar MJS, Zheng Y-J (1990) Structure of the oxalate ion. J Mol Struct THEOCHEM 209:157–162. doi: 10.1016/0166-1280(90)85053-P

45. Clark T, Von Ragué Schleyer P (1981) Conformational preferences of 34 valence electron A2X4 molecules: An ab initio Study of B2F4, B2Cl4, N2O4, and C2O 42−. J Comput Chem 2:20–29. doi: 10.1002/jcc.540020106

46. Herbert JM, Ortiz JV (2000) Ab Initio Investigation of Electron Detachment in Dicarboxylate Dianions. J Phys Chem A 104:11786–11795. doi: 10.1021/jp002657c

47. Lin I-C, Seitsonen AP, Tavernelli I, Rothlisberger U (2012) Structure and Dynamics of Liquid Water from ab Initio Molecular Dynamics—Comparison of BLYP, PBE, and revPBE Density Functionals with and without van der Waals Corrections. J Chem Theory Comput 8:3902–3910. doi: 10.1021/ct3001848

48. Jonchiere R, Seitsonen AP, Ferlat G, et al (2011) Van der Waals effects in ab initio water at ambient and supercritical conditions. J Chem Phys 135:154503. doi: doi:10.1063/1.3651474

49. Gao B, Liu Z (2005) First Principles Study on the Solvation and Structure of C2O42-(H2O)n, n = 6−12. J Phys Chem A 109:9104–9111. doi: 10.1021/jp052968t

50. Rosas-García VM, del Carmen Sáenz-Tavera I, Rodríguez-Herrera VJ, Garza-Campos BR (2013) Microsolvation and hydration enthalpies of $CaC_2O_4(H_2O)$ n (n=0-16) and $C_2O_4^{2-}(H_2O)$ n (n=0-14): an ab initio study. J Mol Model 19:1459–1471. doi: 10.1007/s00894-012-1707-6

51. Nagy PI, Sarver JG (2014) Theoretical conformational analysis for chain systems with two conjugated double bonds in the gas phase and in solution. Comput Theor Chem 1033:43–51. doi: 10.1016/j.comptc.2014.01.025

52. Soper AK (2000) The radial distribution functions of water and ice from 220 to 673 K and at pressures up to 400 MPa. Chem Phys 258:121–137. doi: 10.1016/S0301-0104(00)00179-8

Tables

Table 1. The energetic and geometrical properties of the most stable structures (staggered and planar rotamer) of microsolvated (from 4 to 32) *ox-2* system found by the optimization at BLYP/def2-SVP theory.

O-C-C-O (deg.) [a]	ΔE (kcal/mol) [b]	ΔG (kcal/mol) [c]	E_{solv} (kcal/mol) [d]
4 WAT			
61.08	0.00	0.00	-103.32
10.01	4.94	4.11	-104.58
8 WAT			
61.24	0.00	0.00	-147.17
30.12	3.77	3.49	-150.39
16 WAT			
68.86	0.00	0.00	-209.92
2.68	2.09	1.36	-203.61
32 WAT			
57.04	0.00	0.00	-259.41
24.88	1.48	1.05	-253.42

[a] Value of the torsion O-C-C-O angle, [b] relative energies with respect to the most stable structure found, [c] relative Gibbs free energies with respect to the most stable structure found, [d] solvation energy calculated as the counterpoise-corrected interaction energy of the anion and the water molecules

Table 2. The energetic and geometrical properties of the most stable structures of microsolvated (from 4 to 32) of *ox-1-closed* and *ox-1-open* systems found by the optimization at BLYP/def2-SVP theory.

O-C-C-O [a] (deg.)	ΔE [b] (kcal/mol)	ΔG [c] (kcal/mol)	E_{solv} [d] (kcal/mol)	O-C-C-O [a] (deg.)	ΔE [b] (kcal/mol)	ΔG [c] (kcal/mol)	E_{solv} [d] (kcal/mol)
	ox-1-closed				***ox-1-open***		
4 WAT							
50.40	11.91	11.61	-50.19	54.75	10.20	9.27	-57.27
1.14	0.00	0.00	-44.54	28.00	6.99	6.15	-53.62
8 WAT							
79.19	7.78	6.97	-72.00	67.30	8.61	6.37	-79.37
16.62	0.00	0.00	-70.54	19.89	5.74	4.34	-82.69
16 WAT							
53.11	4.13	4.01	-104.95	65.03	6.88	4.70	-112.85
23.59	0.00	0.00	-100.67	20.34	2.83	2.61	-107.84
32 WAT							
72.53	1.18	0.93	-122.60	60.54	0.05	-1.11	-127.65
38.01	0.00	0.00	-121.98	8.93	-2.03	-1.37	-128.69

[a] Value of the torsion O-C-C-O angle, [b] relative energies with respect to the most stable structure of *ox-1-closed* system found, [c] relative Gibbs free energies with respect to the most stable *ox-1-closed* system structure found, [d] solvation energy calculated as the counterpoise/corrected interaction energy of the anion and the water molecules

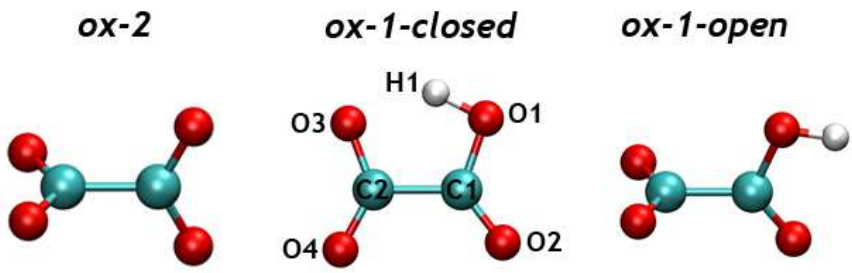

Figure 1. Structures of oxalate (*ox-2*) and hydrogenoxalate (*ox-1*) anion. Atom labeling used further in the text is also depicted for *ox-1*.

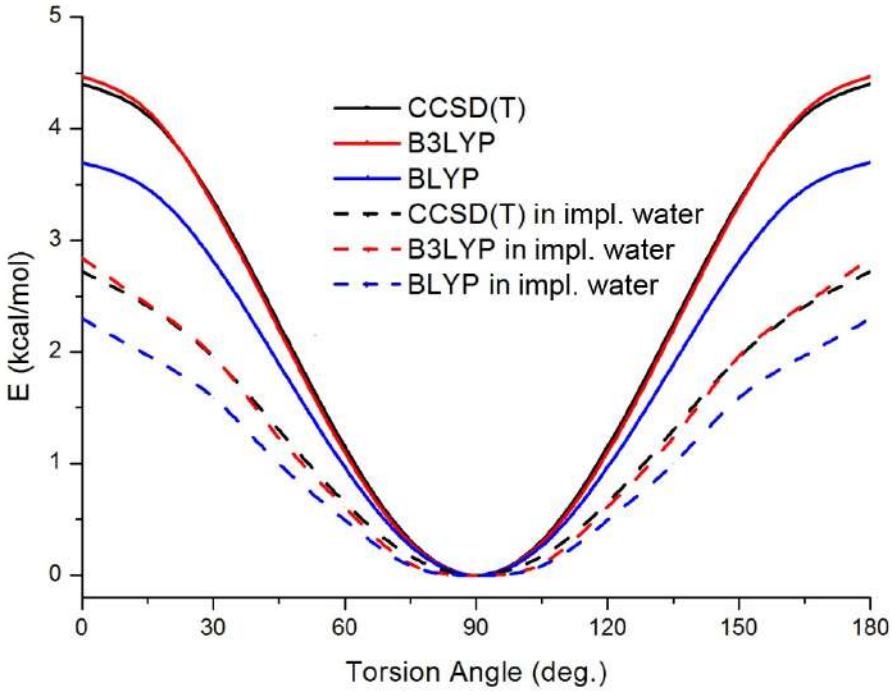

Figure 2. A O-C-C-O torsion profile (in kcal/mol) in oxalate dianion employing various methods. Full lines correspond to data in gas phase, dashed lines to data in implicit water.

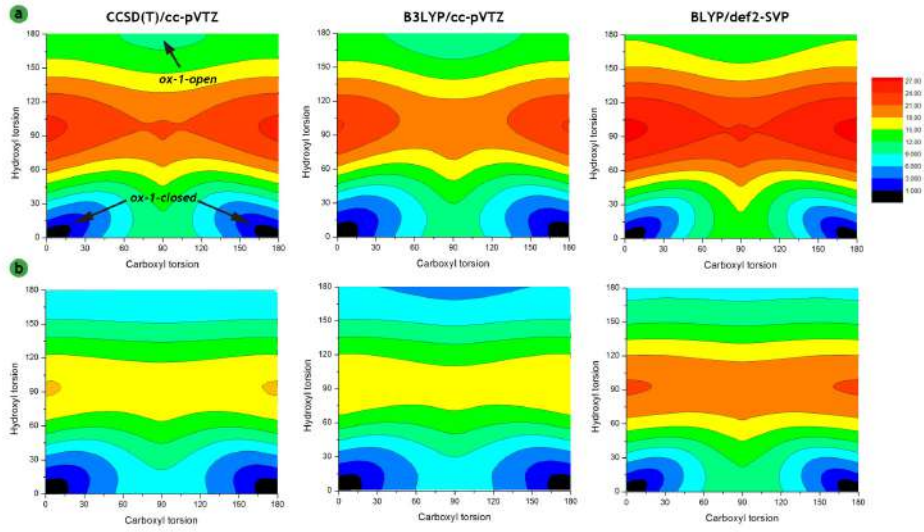

Figure 3. The stability of hydrogenoxalate anion in dependence on the value of O-C-C-O (carboxyl) and H-O-O-C torsion angle (hydroxyl). a) The data obtained in gas phase, b) the data for implicit solvent. Torsion angles are in degrees, energies are in kcal/mol.

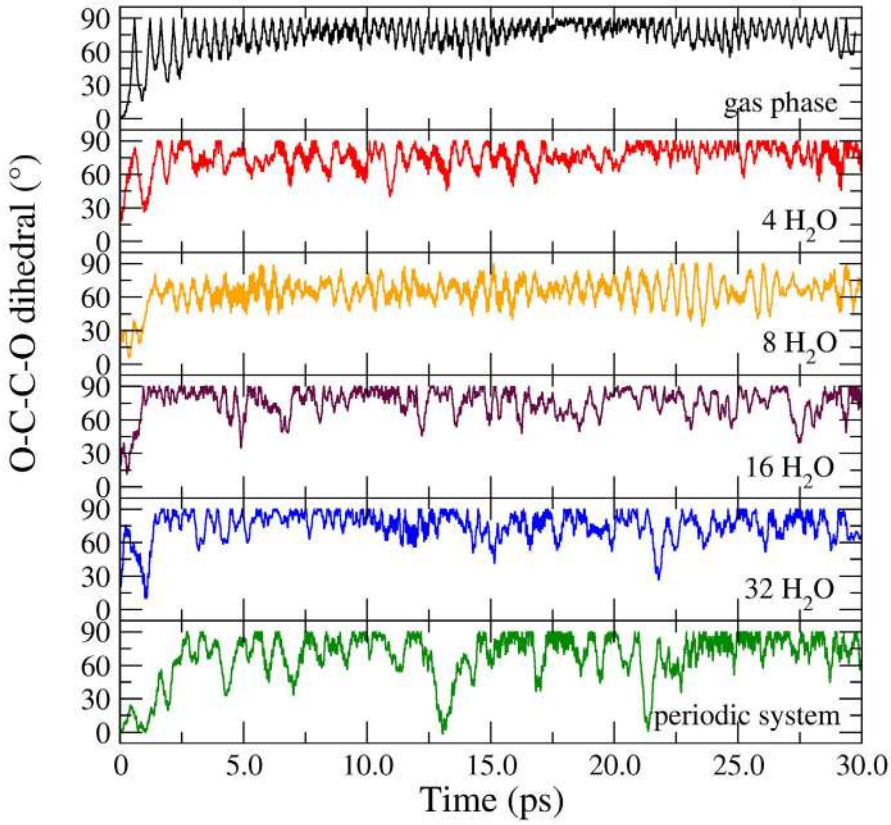

Figure 4. The time evolution of the O-C-C-O dihedral in *ox-2* structure in dependence on number of water molecules presented. From top to bottom: gas phase, microsolvation (ms) with respective water molecules, and the simulation in periodic box containing 50 water molecules. The simulations depicted here started from the planar arrangement and does not differ from those started from staggered conformation.

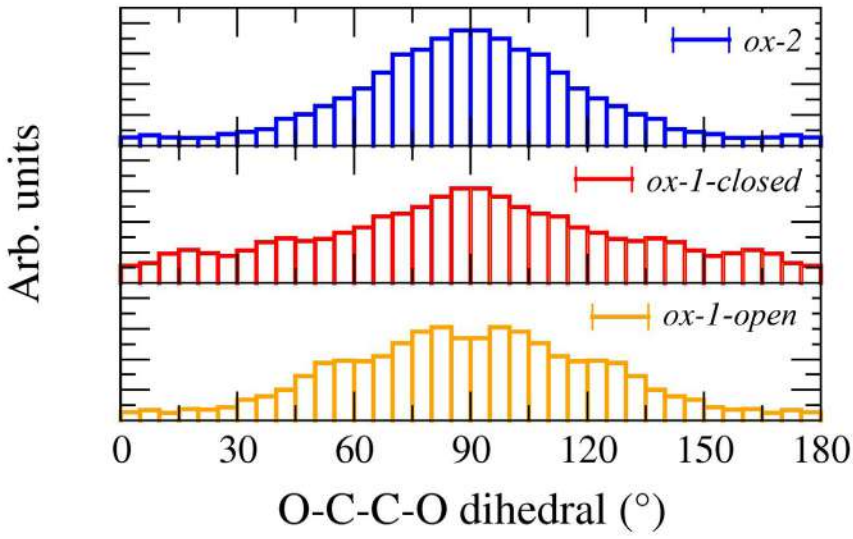

Figure 5. Distribution of O-C-C-O dihedral for AIMD simulations in periodic box. The first 5 ps of the simulation were not included. Data were symmetrized around C2 axis of symmetry.

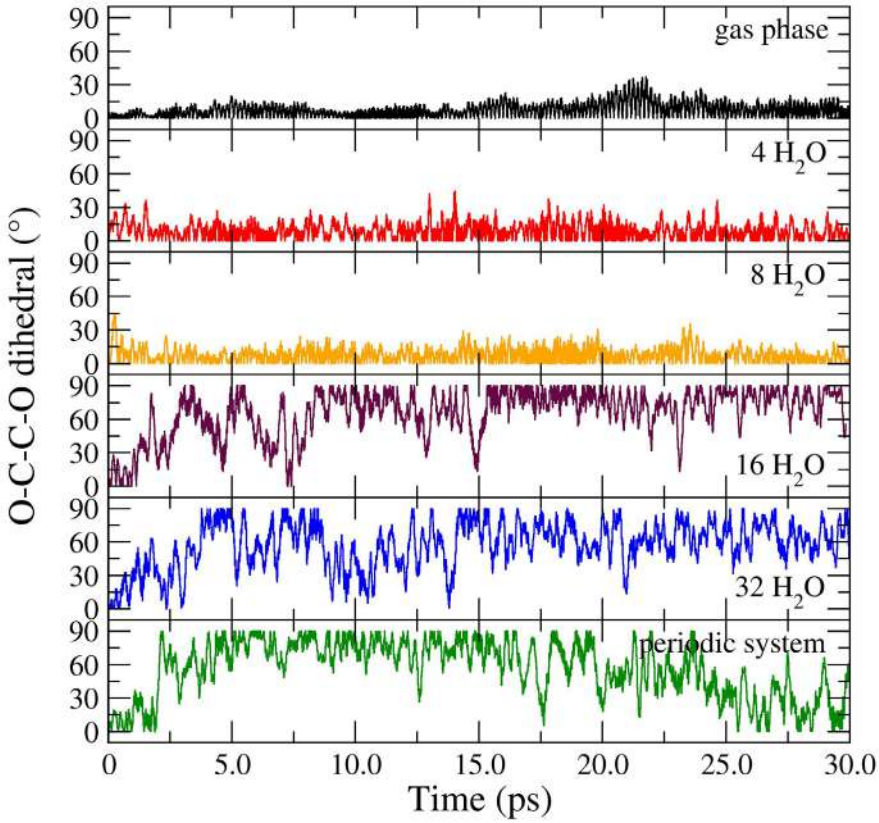

Figure 6. Time evolution of the O-C-C-O dihedral in *ox-1-closed* structure in dependence on number of water molecules presented. From top to bottom: gas phase, microsolvation with respective water molecules, and the simulation in periodic box containing 50 water molecules. The simulations depicted here started from the planar arrangement and does not differ from those started from staggered conformation.

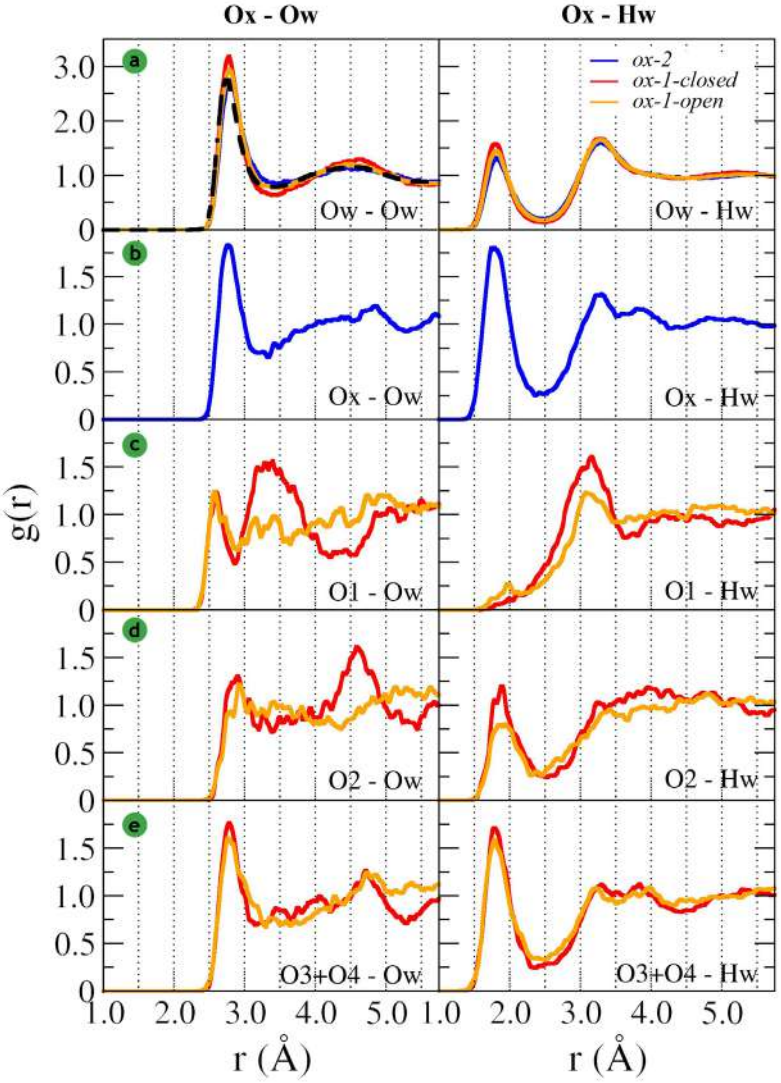

Figure 7. Radial distribution functions between water oxygen (left column), respectively water hydrogen (right column) and (a) water oxygen, (b) oxalate oxygen (c-e) hydrogenoxalate oxygens. For the labeling of the atoms see Figure 1. Black dashed line in (a) originated from experimental data [52].

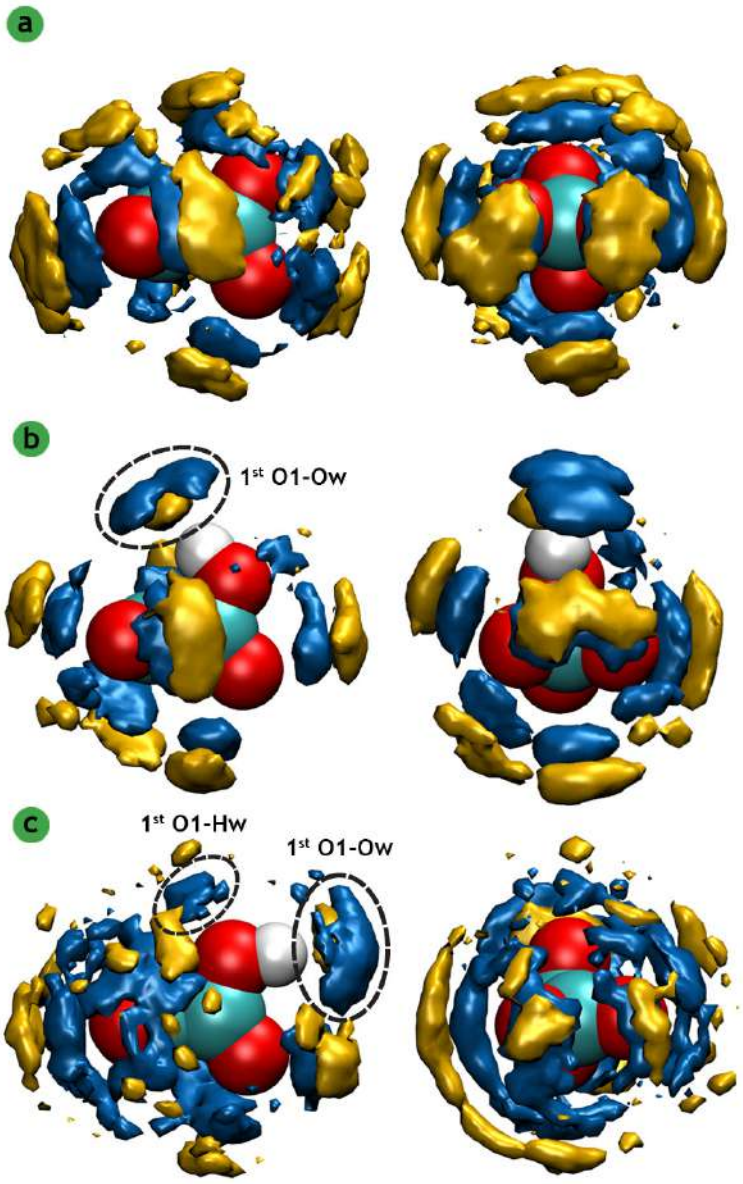

Figure 8. A spatial distribution function of water oxygen (yellow) and water hydrogen (blue) around: a) *ox-2* (b) *ox-1-closed* and (c) *ox-1-open* structure. The profiles were generated by averaging all snapshots of the simulation.

Structure and Dynamics of Solvated Hydrogenoxalate and Oxalate Anions: a Theoretical Study

Ondřej Kroutil, [1,2] Babak Minofar[1,3] and Martin Kabeláč[*1]

Table S1. Geometric parameters of oxalic acid anions. Average MD values were taken from the last 25 ps of the trajectory. For *ox-1*, geometric parameters that includes O1, O2, O3 and/or O4 are reported separately (for the assignment see Figure 1). Bond lengths are in Ångströms and angles in degrees

	AIMD/BLYP/DZVP			BLYP/def2SVP		
	ox-2	***ox-1-closed***	***ox-1-open***	***ox-2***[a]	***ox-1-closed***[a]	***ox-1-open***[a]
C-C	1.56 ± 0.05	1.54 ± 0.04	1.55 ± 0.04	1.60/1.57	1.61/1.60	1.57/1.56
C-O	1.28 ± 0.03	1.34 ± 0.03 (O1)	1.34 ± 0.04 (O1)	1.28/1.28	1.36/1.35 (O1)	1.39/1.37 (O1)
		1.24 ± 0.02 (O2)	1.24 ± 0.03 (O2)		1.22/1.22 (O2)	1.23/1.23 (O2)
		1.27 ± 0.03 (O3)	1.27 ± 0.03 (O3)		1.29/1.28 (O3)	1.26/1.26 (O3)
		1.28 ± 0.03 (O4)	1.27 ± 0.03 (O4)		1.24/1.25 (O4)	1.26/1.26 (O4)
O-H	-	1.04 ± 0.04	1.05 ± 0.06		1.05/1.03	0.99/0.99
O-C-O	125.5 ± 3.3	121.0 ± 2.9 (O1/2)	124.9 ± 3.3 (O1/2)	125.6/126.0	124.2/123.9 (O1/2)	119.0/121.4 (O1/2)
		127.3 ± 3.1 (O3/4)	127.0 ± 3.0 (O3/4)		130.4/130.1 (O3/4)	132.3/130.6 (O3/4)
C-C-O	117.0 ± 3.8	117.2 ± 3.3 (O1)	112.9 ± 3.6 (O1)	117.2/117.0	107.7/108.9 (O1)	112.9/112.4 (O1)
		121.5 ± 3.6 (O2)	121.9 ± 3.7 (O2)		128.1/127.2 (O2)	128.1/126.1 (O2)
		116.2 ± 3.7 (O3)	116.1 ± 3.4 (O3)		109.5/110.8 (O3)	113.7/114.7 (O3)
		116.2 ± 3.7 (O4)	116.5 ± 3.4 (O3)		120.1/119.2 (O4)	114.0/114.7 (O4)
C-O-H	-	112.8 ± 4.9	111.9 ± 5.4	-	95.8/98.0	112.9/106.3
O-C-C-O	70.9 ± 17.9	58.7 ± 29.9	60.9 ± 21.9	90.0/90.0	0.0/0.0	90.5/91.3

[a] gas-phase/PCM implicit model

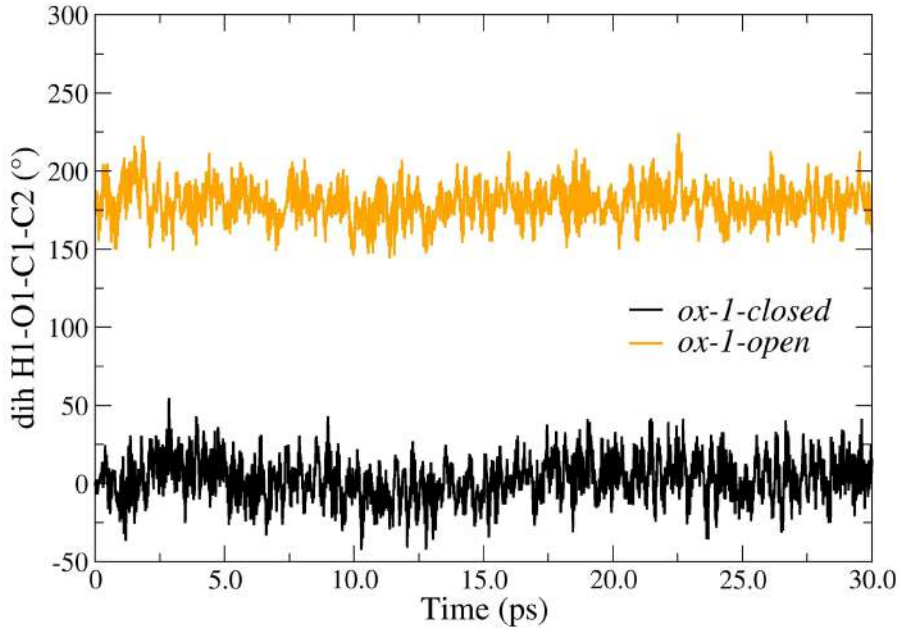

Figure S1. Time evolution of the H1-O1-C1-C2 dihedral in hydrogenoxalate anions with different starting geometry.

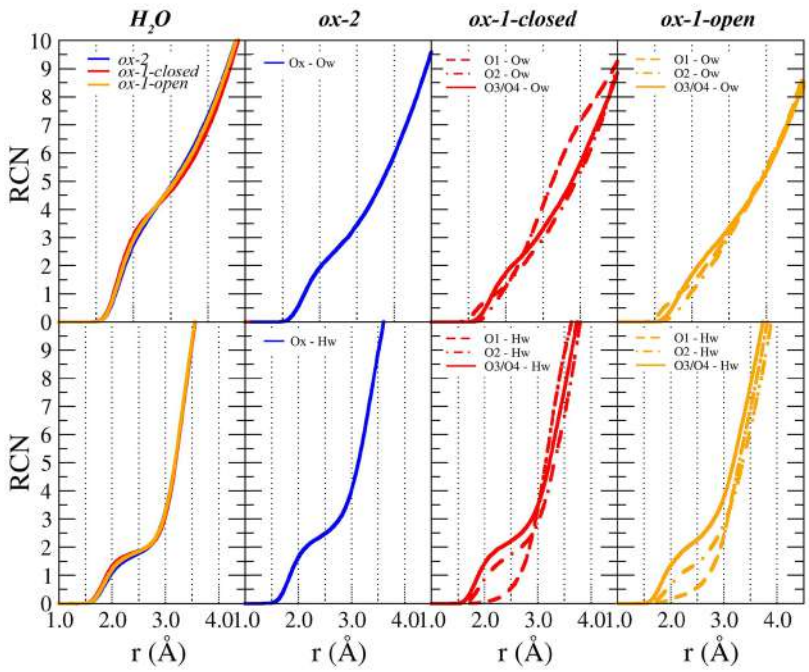

Figure S2. Running coordination numbers corresponding to RDFs in the Figure 7 in the main text. Top: Ow-Ow coordination number (1st column) and Ox - Ow coordination numbers for *ox-2* (2nd column), *ox-1-closed* (3rd column) and *ox-1-open* (4th column). Down: Ow-Hw and Ox-Hw coordination numbers.

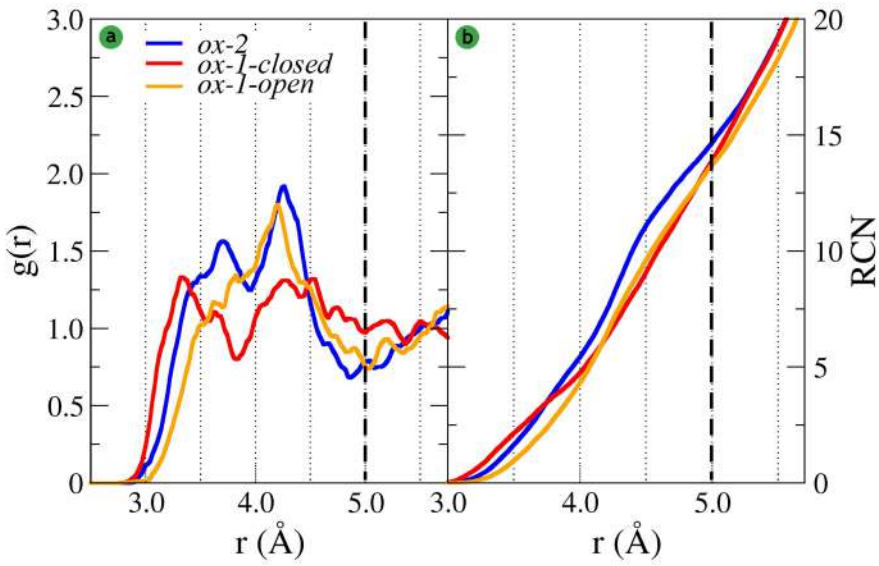

Figure S3. (a) Radial distribution functions between center-of-mass of the (hydroxy)oxalate anion and water oxygen (Ow). (b) Corresponding running coordination numbers. Black vertical dashed lines indicate the end of the first solvent shell.

okroutil@gmail.com

Molecular modeling of biomolecules – surface interactions
Ph.D. Thesis Series, 2016, No. 6

Printed in the Czech Republic by Typodesign
Edition of 20 copies

University of South Bohemia in České Budějovice
Faculty of Science
Branišovská 1760
CZ-37005 České Budějovice, Czech Republic
Phone: +420 387 776 201
www.prf.jcu.cz, e-mail: sekret-fpr@prf.jcu.cz